博士論文

Study on Electric-Field-Induced 2D Superconductivity

（電界誘起2次元超伝導の研究）

斎藤　優

Abstract

Recent advances in materials fabrication enabled the manufacturing of ordered 2D electron systems, such as heterogeneous interfaces, atomic layers grown by molecular beam epitaxy, mechanically exfoliated thin flakes and field-effect devices. These 2D electron systems are highly crystalline and some of them, despite their single-layer thickness, exhibit a sheet resistance more than one order of magnitude lower than that of conventional amorphous or granular thin films. In particular, owing to the recent development of electric-double-layer transistors, it is now enabled to realize electric-field-induced 2D crystalline superconductivity at various electrochemical interfaces.

In this thesis, first of all, I describe two-dimensional transport properties of electric-field-induced superconductivity, and then investigate two anomalous quantum states, i.e., quantum metallic state and the quantum Griffiths phase. In the quantum metallic state, the flattening resistance behavior appears at low temperatures, suggestive of the energy dissipation process originating from quantum creep of vortices due to weak pinning and quantum fluctuation. The quantum metallic state is gradually converted *via* the quantum Griffiths state to the weakly localized metal at high magnetic fields. The scaling behavior, characterized by the divergence of the dynamical critical exponent (Griffiths singularity), indicates that the quantum fluctuation manifests itself as superconducting puddles, in stark contrast to the thermal fluctuation.

In addition, I focus two unprecedented phenomena owing to broken inversion symmetry originating from the crystal structure in ion-gated MoS_2: one is the experimental observation of enhanced in-plane upper critical field up to 52 T due to in-plane mirror symmetry

breaking and Zeeman-type spin-orbit coupling (spin-valley locking), and the other is the nonreciprocal transport including unidirectional longitudinal magnetoresistance and magnetochiral Hall effect in vortex flow and fluctuation regime. These series of unprecedented phenomena suggest that ion-gated 2D crystalline superconductors evidently offer tremendous opportunities to unveil the intrinsic exotic nature of superconductors.

Acknowledgments

First and foremost, let me thank my advisor, Prof. Yoshihiro Iwasa, for guiding my research for six years. He set for me a high standard in graduate research and was always available to discuss physics and revise manuscripts despite a grueling schedule. It is my great pleasure to finish PhD program under his supervision and have developed the new research field of 2D crystalline superconductors.

I owe also a great debt of gratitude to Prof. Tsutomu Nojima for discussions on everything of 2D superconductors, Prof. Jianting Ye for telling me high-quality nanofabrication techniques and Prof. Yuichi Kasahara for discussions on general topics of superconductivity.

I express my gratitude to Prof. Kazushi Kanoda, Prof. Tsuyoshi Tamegai and Prof. Takasada Shibauchi for valuable discussions, comments and suggestions on this thesis.

I would like to thank all members in Iwasa group for their encouragement and support. In particular, I deeply appreciate Dr. Masaro Yoshida for various experimental supports, especially at the very initial stage, and helpful discussions in a wide range from detailed experimental techniques to physics. I also thank current and former group members for experimental supports and discussions; Dr. Yijin Zhang, Dr. Masaki Nakano, Dr. Toshiya Ideue, Dr. Wu Shi, Dr. Ryuji Suzuki, Dr. Sunao Shimizu, Dr. Takafumi Hatano, Dr. Yoichi Nii, Dr. Satria Zulkarnaen Bisri, Dr. Hiroki Shioya, Mr. Takahiko Iizuka, Ms. Ayaka Mori, Mr. Masaru Onga, Mr. Yuji Nakagawa, Mr. Shota Koshikawa, Mr. Hideki Matsuoka, Mr. Yuki Takeuchi, Mr. Takahiro Kurosu, Mr. Takashi Gokuden, Ms. Naoko Inoue, Mr. Keita Hamamoto, Mr. Jun Miyazaki, Mr. Takato Hada, Mr. Yue Wang, Mr. Feng Qin, Mr. Yuki Itahashi, Mr. Yuta

Kashiwabara, Mr. Daiki Shin, Mr. Hiroaki Taiko, Mr. Takatoshi Akamatsu, Mr. Yuki Majima, Mr. Naoki Shiba, Ms. Sasha Yamada, Mr. Josha Young and Mr. Frans Mattsson. I sincerely thank Mrs. Fumiko Yamaura for many supports as a secretary.

My research has benefited from scientific discussions and collaborations outside Iwasa group. I deeply thank Prof. Youichi Yanase and Dr. Yasuharu Nakamura for theoretical supports on upper critical field data, Dr. Mohammad Saeed Bahramy for the calculation of the band structure, Prof. Naoto Nagaosa, Dr. Motohiko Ezawa, Dr. Shintaro Hoshino and Mr. Ryohei Wakatsuki for theoretical supports for nonreciprocal physics, and Prof. Yoshimitsu Kohama and Prof. Masashi Tokunaga for supports of high magnetic field measurements.

Finally, I would like to thank my family, in particular my parents, for their understanding and supports of my research life.

Contents

List of Figures

List of Tables

1 Introduction

1.1 Overview and outline

Two-dimensional (2D) superconductivity has been developed over the last 80 years, and has kept providing a variety of quantum phenomena. Figure 1.1 shows the history of superconducting films toward the atomic thickness after 1980. In the early days of researches, the major methods of fabricating 2D superconductors were thermal evaporation and sputtering of metallic films, in which most of the basic concepts of 2D superconductors were established [1−5].

After 1980, physics of quantum phase transition (QPT) was intensively discussed and established in thin film superconductors ranging from 0.3 to 10 nm in thickness, particularly with disordered structures mostly in amorphous and granular forms (open symbols in Fig. 1.1) [6−13]. It is also noted that in 1990's pioneering works on the fabrication of monolayer cuprate superconductors have been reported [14, 15]. These researches were the dawn of new stages coming in the 21st century, in which a variety of new fabrication techniques, including layer-by-layer molecular beam epitaxy (MBE) accompanied with surface/interface reconstruction process, mechanical exfoliation and field effect devices, have been introduced to the field

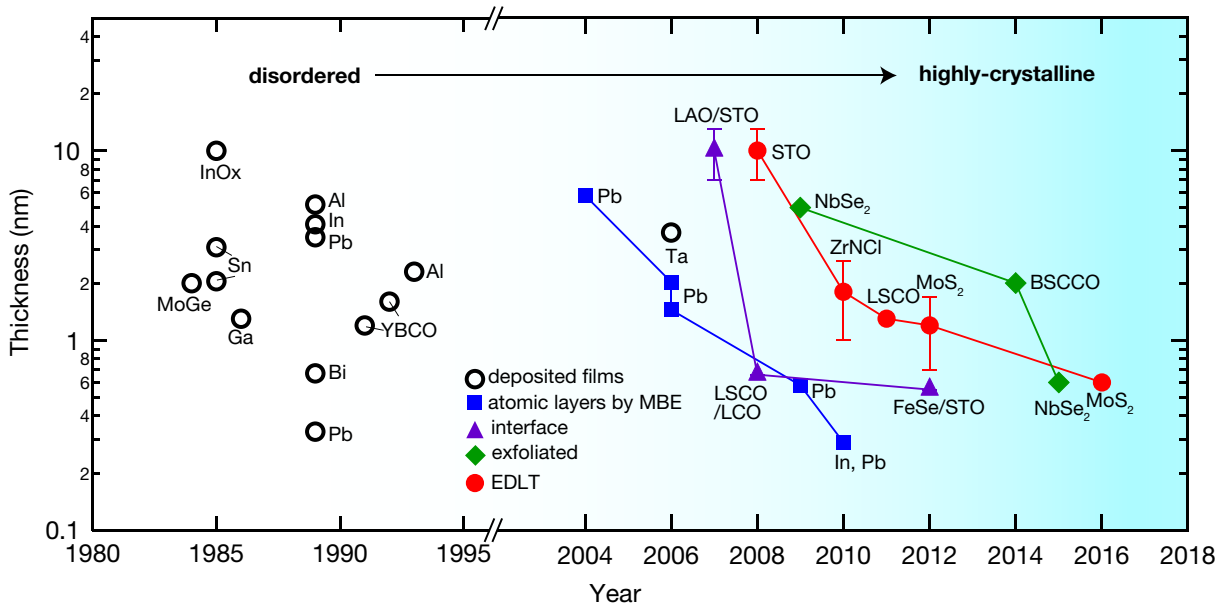

Figure 1.1 | History of 2D superconductors. A plot of their thickness versus year for 2D superconductors after 1980. In the last century, the majority of 2D superconductors were mostly fabricated by deposition of metallic thin films, which are strongly disordered, amorphous or granular (open circles)[6−13]. In the 21st century, atomic layers grown by layer-by-layer MBE (blue squares)[16−20] technique, interfacial superconductors (purple triangles)[21−23], exfoliated atomic layers (green diamonds)[24−27] and EDLT (red circles)[28−31,131] have been fabricated. All of them are highly crystalline, in marked contrast to the conventional ones. Open circles include three kinds of deposited thin films: InO_x, MoGe and Ta are sputtered thin films, Sn, Ga, Al, In, Pb and Bi are MBE-grown thin films, and $YBa_2Cu_3O_y$ (YBCO) is deposited by reactive evaporation.

of 2D superconductors (closed symbols in Fig. 1.1) [16−31]. As a result, the crystallinity was dramatically improved even in the atomic level thickness. With these newly emerging 2D superconductors, researchers are able to access superconductivity in the 2D limit with highly crystalline form. These 2D superconductors are in stark contrast to the highly disordered 2D superconductors fabricated in the last century. In particular, electric-field-induced superconductivity, which is realized by the combination of mechanical exfoliated atomic crystals and field effect produced disorder-minimum 2D superconductors, have a great potential to become a new platform for studying physics as well as for searching novel and high-temperature superconductors. Motivated by such backgrounds, I aim to clarify the intrinsic properties of 2D crystalline superconductors using electric-field-induced superconductivity in this study.

In chapter 1, I first begin with an introduction of the history and general issues of 2D

superconductors, and recent developments of 2D crystalline superconductors fabricated by variety of techniques as I mentioned above. Following this introductory chapter, I explain the experimental methods used in my study in chapter 2. The basic techniques are mechanical exfoliation, standard nanoscale-fabrication technique with electron-beam lithography, electrode evaporation and lift-off process, and ionic liquid gating. I also explain the electrical measurement setup used in this study.

Chapter 3 of the thesis deals with 2D nature and quantum phase transitions in ion-gated MoS_2 and ZrNCl single crystalline flakes generated by mechanical exfoliation. Superconductor-insulator transition (SIT) is one of the remarkable phenomena driven by quantum fluctuation in 2D systems. Such a QPT was investigated predominantly on highly disordered thin films with amorphous or granular structures [32, 33] and discussed in terms of its universality class with constant critical parameters and scaling exponents for decades. However, highly crystalline 2D superconductors [21, 22, 26, 27, 30, 34], which became available by the recent technological advances, have suggested a totally different view on the quantum fluctuation [35−38]. In this chapter, I demonstrate the several 2D nature in terms of fluctuation and upper critical field, and provide a unified picture of temperature versus magnetic field phase diagram of highly crystalline 2D superconductors. According to the magneto-transport measurements in 2D superconducting ZrNCl and MoS_2, we found that the quantum metallic state (vortex liquid), appeared as a flattening resistance at low temperatures, commonly observed at low magnetic fields is gradually converted *via* the quantum Griffiths state to the weakly localized metal at high magnetic fields. The scaling behavior, characterized by the divergence of the dynamical critical exponent (Griffiths singularity), indicates that the quantum fluctuation manifests itself as superconducting puddles, in marked contrast to the thermal fluctuation. We propose that the phase diagram exhibiting an evolution from quantum metallic to the quantum Griffiths state is generic nature in highly crystalline 2D superconductors with weak pinning potentials.

Chapter 4 describes 2D superconducting state with nearly unmeasurable robustness

against in-plane magnetic fields (termed Ising superconductivity) realized in gated $2H$-MoS_2. In this chapter, I deal with gate-induced 2D superconductivity in MoS_2, which possesses intrinsic Zeeman-type SOI that is, in contrast to the Rashba-type SOI, manifested by an out-of-plane spin polarization. Using pulsed magnetic field measurements, we found a surprisingly high in-plane upper critical field showing 52 T at 1.5 K, indicating that the Pauli limit in this system is 4 times larger than the conventional Pauli limit in centrosymmetric systems. Based on realistic tight-binding calculations and numerical calculations of upper critical field, we revealed that this anomalous enhancement originates from an inter-valley Cooper pairing protected by spin-valley locking due to broken mirror symmetry in monolayer and Zeeman-type spin splitting.

Chapter 5 includes nonreciprocal transport in 2D superconducting MoS_2. We found that second harmonic resistance in longitudinal and transverse direction appears only in the configuration of excitation current parallel to the zigzag and armchair edge, i.e., unidirectional magnetoresistance and magnetochiral Hall effect, respectively, while no discernible signal in the other direction has not been observed, which is consistent with the trigonal crystal symmetry. Furthermore, we studied the temperature and current dependence of nonlinear superconducting transport and clarified the unique behaviors, which propose that, in addition to the effect of superconducting fluctuation, the vortices are rectified by the intrinsic asymmetric potentials originating from structural threefold symmetry.

In the final chapter of this thesis, I summarize the conclusion in this study and describe a future perspective.

1.2 History and general issues of 2D superconductors

In 1938, Shal'nikovs first reported superconductivity in Pb and Sn thin films [1], which was the ground-breaking work of thin film superconductors. Following this pioneering work, Buckel, Hilsh [2] and many researchers investigated different kinds of thin films made of soft metals and alloys [3−5]. In the early stage of thin film researches, a quench condensation method was

used where the elements of metals were deposited on surface of a substrate at low temperatures in a high vacuum chamber immersed in liquid-Helium. Those thin films were in amorphous or granular forms with the random arrangement of elements or the random orientation of their crystallites, and were therefore useful to investigate geometrical properties neglecting crystal orientation effects. For example, the angular dependence of upper critical field in thin film superconductors shows a cusp-like peak structure at the magnetic field direction parallel to the film plane [39]. This feature was well explained by the phenomenological Ginzburg-Landau (GL) theory. Tinkham pointed out in 1963 [40] that the cusp-like peak is one of the distinct characteristics of geometrical effect in 2D superconductors. According to the above scheme, 2D superconductors are defined as superconductors with their thickness thinner than the in-plane GL coherence length.

In addition, 2D superconductors shows many other interesting properties such as localization [41], transition temperature oscillation by quantum size effects [16, 42, 43], excess conductivity originating from fluctuation [44−46], Berezinskii-Kosterlitz-Thouless (BKT) transition [47−49] and QPT at zero temperature [32, 33]. In particular, the BKT transition, which is observed in the jump of the power-law exponent at zero current limit in current-voltage characteristic and the disappearance of ohmic resistance obeying the Halperin-Nelson scaling law, is treated as the evidence of 2D superconducting transition through the binding of vortex-antivortex pairs, as shown in a previous work (Figs. 1.2a and b) [50].

One of the most important issues in 2D superconductors is the QPT [32, 33], which has been intensively discussed to date. The SIT in metallic thin films was believed to occur only at zero temperature limit as a function of external tuning parameters, such as disorder (or film thickness), out-of-plane magnetic fields and carrier density (or electric fields), which determine the ground state of the system. The SIT in disordered systems can be divided in two-groups: one is originating from the amplitude fluctuation of the order parameter, and the other includes the phase fluctuation. Fisher and others [32, 51−53] suggested a“dirty-boson”

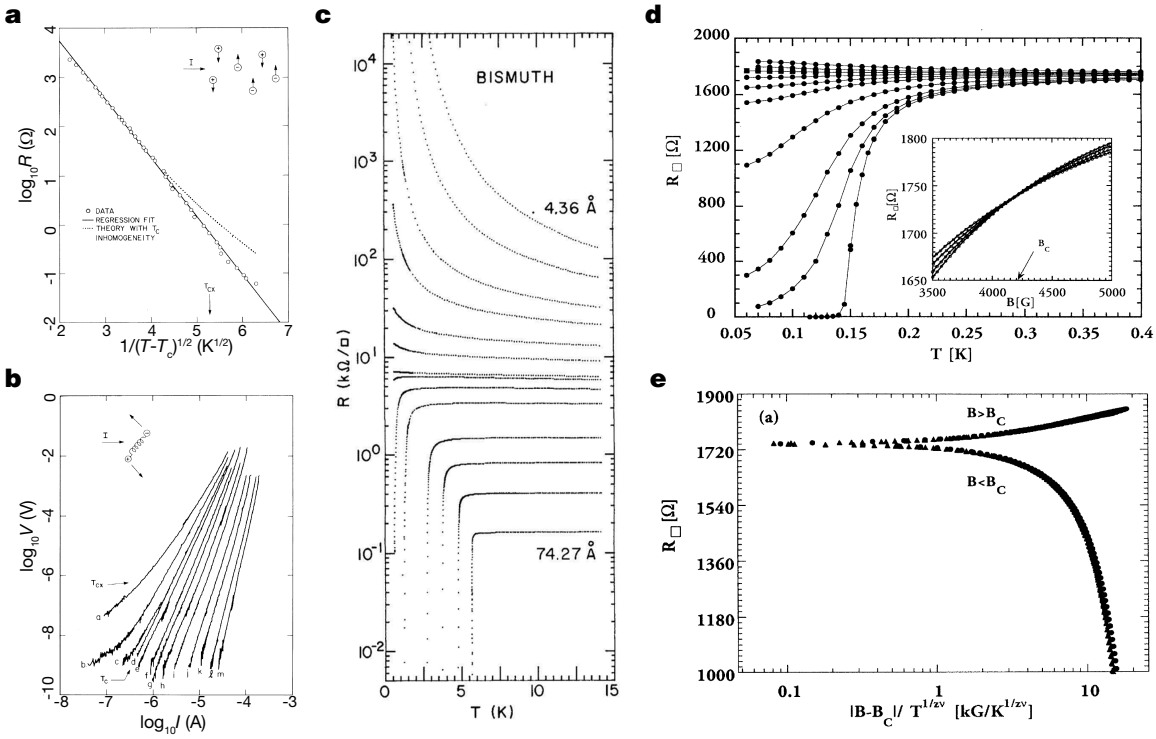

Figure 1.2 | 2D superconductivity in deposited metallic thin films. **a**, Logarithm of the resistance versus $(1 - T/T_{\mathrm{c}})^{-1/2}$ in amorphous $\mathrm{InO_x}$ [50]. Here, T_{c} is treated as the BKT transition temperature. These data represent the vortex-flow resistance of thermally excited vortices and antivortices. Inset: A schematic image of vortex flow process. **b**, Voltage-current characteristics in amorphous InO_x thin films between 1.460 K and 1.939 K. Inset: A schematic image of nonlinear pair-breaking process due to unbinding of a vortex-antivortex pair. **c**, Evolution of SIT in amorphous Bi films with the decrease in film thickness corresponding to the increase in degree of disorder [10]. **d**, Sheet resistance versus temperature under magnetic fields in amorphous MoGe. Inset: Magnetoresistance around the critical magnetic field B_{c} = 4.19 kG [54]. **e**, Finte size scaling of sheet resistance as a function of $|B - B_{\mathrm{c}}|/T^{1/z\nu}$.

model, considering that the SIT is caused by the quantum fluctuation of the phase and long-range Coulomb repulsions (interacting Cooper-pairs). They predicted that it is characterized by a universal sheet resistance (called as quantum resistance) $R_{\mathrm{Q}} = h/(2e)^2$ at the transition point with h the Plank constant and e the elementary charge, which is independent of materials or systems, and the scaling behavior of temperature dependence of sheet resistance $R_{\mathrm{sheet}}(T)$ against $|x - x_{\mathrm{c}}|/T^{1/z\nu}$, where x and x_{c} are a tuning parameter and its critical value, and ν and z the static and dynamic critical exponents, respectively. In the case of magnetic field induced SIT, this model can be understood from self-duality of Cooer pairs and vortices: the super-

conducting phase is a condensate of by Cooper pairs with the localized vortices (vortex glass), while the insulating phase is a condensate of the vortices with localized Cooper pairs (Bose glass). Experimentally, some metallic films such as amorphous-Bi (Fig. 1.2c) shows a critical R_{sheet} almost equal to R_{Q} for disorder induced SIT [10]. The scaling collapse of $R_{\mathrm{sheet}}(T)$ was also observed in the magnetic field induced SIT in films such as amorphous MoGe as shown in Figs. 1.2d and e [54]. However, it has been later pointed out that some others show different behavior [12], for example, an intervening quantum metallic state (possible metallic ground state) with a smaller sheet resistance than R_{Q} between superconducting and insulating state [9, 13, 54−56]. Although various scenarios were proposed for this intervening metallic state, consensus is not yet achieved. Comprehensive review papers on SIT in conventional disordered 2D superconductors are published [33, 57, 58].

Another issue is the effect of SOI and broken inversion symmetry on the superconducting state. In conventional 2D films in the dirty limit, due to the amorphous structure, it has been unable to access the intrinsic properties originating from crystal structure. Also, in such disordered thin films, the large parallel upper critical field that is exceeding the conventional Pauli limit has been attributed to the strong spin-orbit scattering [59, 60]. In highly crystalline systems with less disorder and long mean free paths, however, we can approach the intrinsic properties reflecting crystal symmetry, the characteristic spin-split band structure or spin polarizations.

1.3 Developments of 2D crystalline superconductors

Owing to the recent technological advances and introduction of new approaches of thin films fabrications, there have been emerging a variety of 2D superconductors in terms of interfacial superconductors [21, 22, 61, 62], layer-by-layer MBE-grown ordered-metal atomic layers [19, 20], exfoliated single layer [25−27], electric-field-induced 2D systems [28, 29, 63]. In addition, CVD-grown atomic layers [64, 65], heavy-fermion based super-lattices [66] and in-

tercalated graphene [67−69] are also new classes of crystalline superconductors at the 2D limit. These newly emerged 2D superconductors are extremely thin in the atomic layer level and highly crystalline in common, which enable us to address the QPT in the minimal-disorder limit as well as to observe the novel superconducting state originating from the intrinsic nature of the materials, possibly leading to a step forward to 2D topological superconductors [70].

1.3.1 Oxides and chalcogenides interfaces

As mentioned above, until recently, the studies for SIT in 2D superconductors have been mainly performed using the deposited amorphous or granular thin films. In 2007, superconductivity was realized in a 2D electron system at $LaAlO_3/SrTiO_3(001)$ polarized interface fabricated by pulsed laser deposition (Figs. 1.3a and b) [21]. This was indeed a major breakthrough in the history of 2D superconductivity, because $LaAlO_3/SrTiO_3$ heterostructure has been known to show high electron mobility as compared with conventional metallic films [71]. After this success, the electrostatic control of superconductor-metal-insulator transition by using a back gating technique was realized (Fig. 1.3c) [72]. From the comprehensive studies, the superconducting phase diagram (the dependence of superconducting transition temperature T_{c} on gate voltage V_{G} or sheet carrier density) was found to be a dome-shape with the critical exponent of 2/3 in the vicinity of quantum critical point (QCP) at the threshold of the superconducting dome, which indicates that the superconducting-metal transition in $LaAlO_3/SrTiO_3$ is described by the (2+1)D XY model in clean systems. Similar critical behavior was found in ion-gated superconducting MoS_2 [30]. In $LaAlO_3/SrTiO_3$ interface, in addition, the pseudo gap state and the Cooper pairs above T_{c} are also observed with the tunnel spectroscopy [73] and single-electron transistor [74], respectively. As a similar system, the Mott-insulator-based $LaAlO_3/SrTiO_3$ interface was found to show superconductivity [35, 75, 76]. One of the important discoveries in the electrostatically gated $LaAlO_3/SrTiO_3$ interface is the existence of multiple quantum criticality under magnetic fields, where the superconducting 2D electron

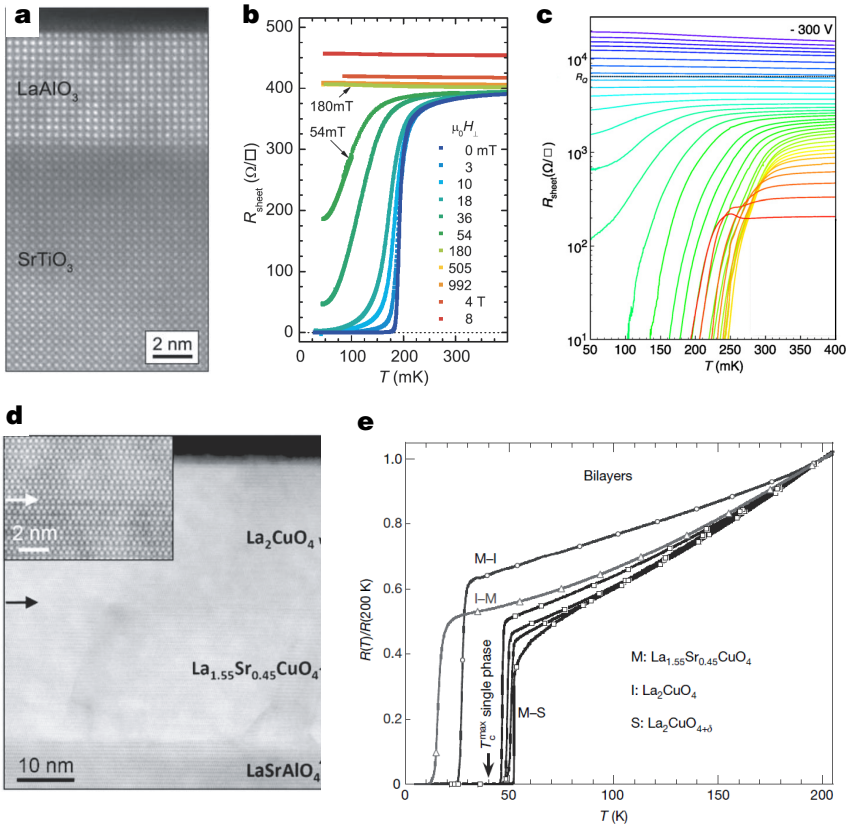

Figure 1.3 | Superconductivity in oxide interfaces. **a**, Image of a 15-unit-cell-thick $LaAlO_3$ grown on $SrTiO_3$ with scanning transmission electron microscopy with high-angle annular dark field [21]. **b**, Sheet resistance as a function of temperature for various magnetic fields. **c**, Superconductor-metal-insulator transition in $LaAlO_3/SrTiO_3$ controlled by electric fields [72]. **d**, A image of the structure of $La_2CuO_4/La_{1.55}Sr_{0.45}CuO_4/LaSrAlO_4$ with annular dark field [22]. Inset: a magnified image of the M−I interface. **e**, $R(T)/R(200\text{ K})$ for various bilayers (M-S, I-M and M-I sequences). S, M and I are $La_2CuO_{4+\delta}$ (superconducting): oxygen-doped by annealing in ozone, $La_{1.55}Sr_{0.45}CuO_4$ (metallic): overdoped, La_2CuO_4 (insulating): vacuum-annealed [22].

system is driven to a weakly localized metal by passing through the double critical behavior, which is described by a clean and dirty (2+1)D XY model at low (high) and high (low) magnetic fields (temperatures), respectively [35]. An overview on interface superconductors is given [61, 62].

Another important work is the observation of superconductivity at the cuprate-based interface between $La_{1.55}Sr_{0.45}CuO_4$ and La_2CuO_4 (Fig. 1.3d) [22, 77]. While the two components are non-superconducting metal (M) and insulator (I) in the single-phase layers, respectively, the bilayers of them exhibit superconductivity with the deposition-sequence dependent

T_c: 15 K in the I-M sequence and 30 K in the M-I sequence as shown in Fig. 1.3e. More importantly, it was found that if the excess oxygen is doped in La_2CuO_4 of the M-I bilayer, T_c exceeds 50 K. This value is higher than the maximum value of single phase $La_{2-x}Sr_xCuO_4$ and $La_2CuO_{4+\delta}$. Electronic reconstruction at the interface, which is similar to the case of $LaAlO_3/SrTiO_3$, is one possible origin of the improved T_c, although oxygen vacancies and interstitials can be additional factors.

The interfacial superconductivity between a topological insulator and an iron chalcogenide (Bi_2Te_3/FeTe) was also reported, the heterostructure of which was fabricated by MBE [78]. The authors performed various analyses of transport data and confirmed that the superconductivity has the 2D nature with a thickness of ∼7 nm, but the origin of superconductivity remains to be understood.

1.3.2 Layer-by-layer grown atomic films by MBE

Since the beginning of 2000's, the quality of metallic thin film superconductors (especially Pb) grown by MBE have continued to be improved to the extent that the intrinsic property in metallic ordered thin films can be investigated [16−18, 79−81]. Oscillatory behavior of T_c depending on number of monolayers was observed with reducing the thickness [16], which was accounted for in terms of the existence of Fabry-Pe'rot interference modes of electron de Broglie waves in thin films [82, 83]. In 2009, superconductivity in Pb bi-layer crystalline films was observed, which corresponds to a single quantum channel [19], and finally realizing highly crystalline superconductivity in single-atomic-layer of ordered Pb (T_c = 1.5 K) and In (T_c = 3.2 K) ultra-thin films (Figs. 1.4a−f) was successful, which was confirmed by observing the superconducting gaps and vortices using scanning tunnel microscopy (STM) [20]. These atomic layers are the thinnest superconductors in existing systems (Fig. 1.1). After this success, superconducting transition in In and Pb ordered-atomic-layers was confirmed by transport measurement [84, 85]. Particularly, the authors found that atomic steps act as strongly

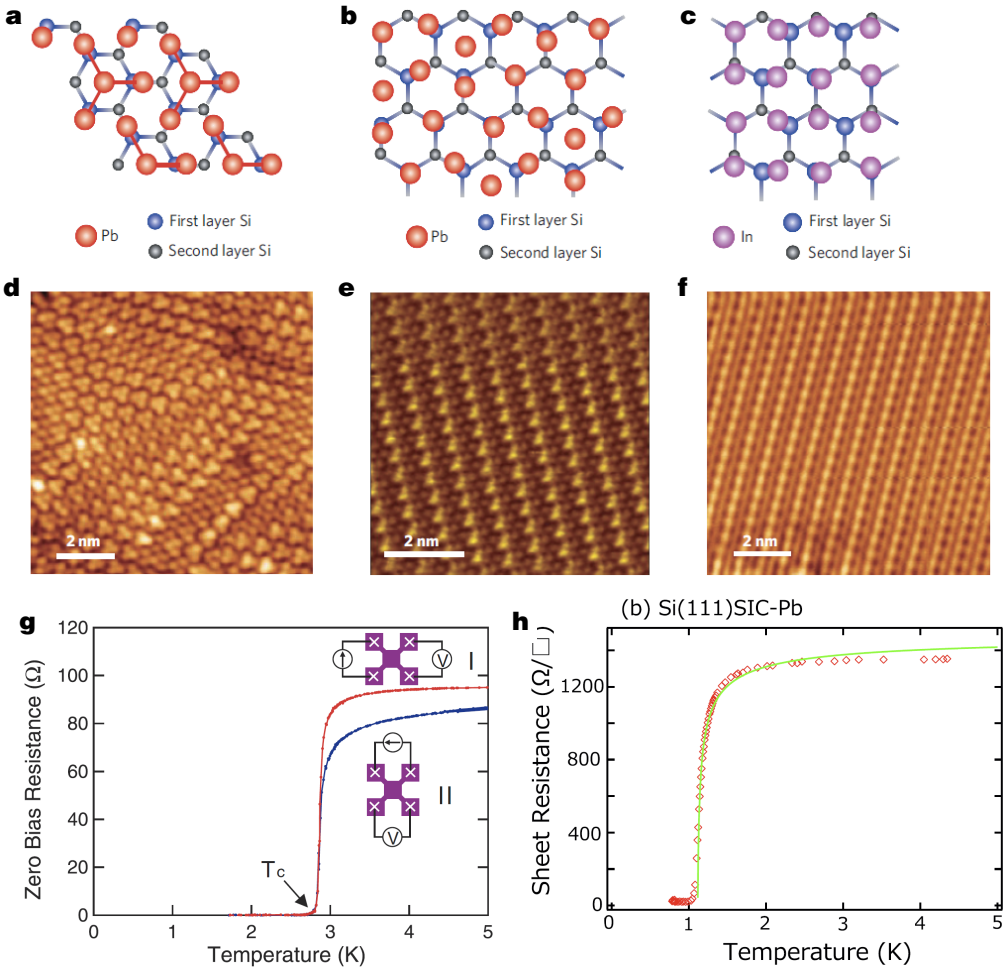

Figure 1.4 | Superconducting atomic layers of Pb and In grown by MBE. a-c, Schematic structure models, **d**−**f**, High-resolution STM based images of the striped incommensurate-Pb (**a**, **d**), $\sqrt{7}\times\sqrt{3}$-Pb (**b**,**e**) and $\sqrt{7}\times\sqrt{3}$-In (**c**, **f**) phases grown on a Si(111) substrate [20]. Sheet resistance as a function of temperature in In (**g**) and Pb (**h**) atomic layers [84, 85]. Insets in Fig. 1.4g: Schematic drawings of the probe configurations I and II.

coupled Josephson junctions [84], where Josephson vortices exist at zero magnetic field [86]. Very recently, fabricating a 2D Tl-Pb atomic layer compound consisting of 1 monolayer Tl and 1/3 layer Pb on Si(111) substrate was successful, and superconducting transition in zero and finite magnetic fields was observed [87].

One of the most intriguing phenomena unique to these kinds of single atomic layer superconductors is the large Rashba spin splitting due to the spin-orbit interaction (SOI) with mirror symmetry breaking along the out-of-plane direction. In Tl-Pb ultra-thin films, the gi-

ant spin splitting ($\sim$ 250 meV) was indeed observed by angle-resolved photoemission spectroscopy (ARPES) measurements [88], which may lead to observe a number of fascinating phenomena. Also, very robust superconductivity against the in-plane magnetic field in a Pb single layer on a cleaved GaAs(110) surface was found [89]. A very large in-plane upper critical field is suggestive of the enhancement of the Pauli paramagnetic limit. In their discussion, the spin-orbit scattering effect in the dirty limit cannot account for the obtained results consistently. The experimental results, on the other hand, are accounted for in terms of an peculiar superconducting state such as a FFLO state or a helical state predicted for 2D metals with a large Rashba SOI [90−92].

Ga crystalline bilayers grown by MBE shows 2D superconductivity [93]. Authors discussed the unique magneto-transport properties observed in this system. Also, MBE-grown $NbSe_2$ one-atomic-layer was fabricated, and showed some signature of the interplay between superconductivity and CDW formation in the 2D limit by ARPES and STM/scanning tunnel spectroscopy (STS) measurements [94].

One of the most amazing studies is high temperature superconductivity in FeSe atomic layers [23]. While T_c for bulk FeSe is 9 K [95], the authors observed high temperature superconductivity in a FeSe single layer grown on $SrTiO_3$ substrate with a superconducting gap of 20 meV at 4.2 K, which corresponds to $T_c \sim 80$ K, in the *in-situ* STM measurements. The onset T_c of 5-unit-cell-thick FeSe with the capping layers is around 40 K in the *ex-situ* resistive measurement, which is still much higher than that of bulk. In this work, the authors mentioned that the bottom first unit cell contributes to the superconductivity. Later, it was reported that T_c exceeded 100 K in FeSe single layer on Nb-doped $SrTiO_3$ substrate by the *in-situ* transport measurements [96]. From ARPES measurements, it is indicated that electronic structure is composed of a crossed single band at the Fermi level: the Fermi surface is made of electron pockets centered at the zone edge [97], and that an annealing process [98] and suppression of spin density wave [99] are necessary for the superconductivity. As the origins for the en-

hancement of T_c, the strain effect and charge transfer have been intensively discussed, and the former was found not to be promising [98−100].

Electrochemical etching induced high temperature superconductivity in FeSe films [101] provided the strong evidence that the electron doping and band bending due to the electric field or the charge transfer from the substrate play a crucial role in the enhancement of superconductivity in FeSe. According to the systematic studies of the effects of substrate ($SrTiO_3$ and MgO), thickness and carrier density, the high T_c phase emerges even when the film is much thicker than the single layer under a strong electric field. It was also found that a few-layer-thick FeSe film on $SrTiO_3$ exhibits superconductivity at about 40 K without gating. By contrast, FeSe on MgO superconductor only under gating possibly because of the absence of charge transfer from the substrate, which is in good agreement with the previous results. A similar conclusion was obtained in the study of Potassium-deposited FeSe multilayer thin films [102].

1.3.3 Mechanical exfoliated atomic layers

Inspired by the discovery of graphene [103, 104] and the subsequently growing researches of 2D materials in various approaches [105−116], researchers found that mechanical exfoliation is another useful method to create 2D superconductors with high crystallinity because in this method single crystalline thin flakes are simply cleaved from bulk single crystals and transferred onto the substrate without crystal growth in vacuum chambers. If the deposition or epitaxial-growth method is called a bottom-up technique, this mechanical exfoliation can be regarded as a top-down method to fabricate 2D superconductors. A single-layer $Bi_2Sr_2CaCu_2O_{8+x}$ (Bi2212) superconductor by cleaving them down to half-unit-cell thickness was successfully fabricated, where graphene was transferred on the top as the protection layer (Figs. 1.5a and b) [25]. Also, recent dvelopments of the transfer technique to use hexagonal boron nitride (*h*-BN) as a substrate or cap-layer [117] allows us to address important issues

in condensed matter physics. Examples include Hofstadter butterfly [118−120] and the fractional fractal quantum Hall effect [121] in graphene heterostructure, as well as the quantum hall effect in black phosphorus [122] and transition metal dichalcogenides (TMDs) [123], all of which also indicate that exfoliated 2D materials is intrinsically less disordered systems. One of the typical exfoliated systems is a 2D $NbSe_2$ crystalline superconductor. Although there was a pioneering work and successfully observed the thickness dependence of T_c in ultra-thin $NbSe_2$ [124], the real thickness was not so reliable because the estimation of the thickness was only from resistivity. A single layer superconducting $NbSe_2$ covered or sandwiched by *h*-BN (Figs. 1.5c and d) [26, 27] was demonstrated. In those studies, $NbSe_2$ was found to be conductive down to a monolayer and the evident signs of superconductivity were observed even in 1−3 layers. These exfoliated 2D superconductors, which are thus higher in crystallinity compared to the MBE-grown thin films or pulsed laser deposited oxide thin films, show a quantum metallic state in the wide range of temperature *T* and magnetic field *B* in the mixed state as discussed below.

1.3.4 Electric-field-induced superconductivity

The field-effect transistor (FET) has been one of the most convenient tools to investigate the pure effect of carrier doping on the various 2D materials without introducing unintentional disorder. In fact, this transistor structure has been utilized for a long time to modulate T_c of conventional superconductor films as well as cuprate superconductor films [125−135]. Among them, remarkable control of T_c and inducing SIT in ultrathin $GdBa_2Cu_3O_{7-x}$ films by using ferroelectric oxide gate was realized [133]. After this success, the electrostatic modulation of SIT in amorphous bismuth thin films was realized [136], and continuous switching from superconducting state to insulating state in $LaAlO_3/SrTiO_3$ was demonstrated [72]. However, the bottleneck of this conventional FET structure with solid gate, which might drag down the research of electric-field-effect control of superconductivity in many materials, is the magni-

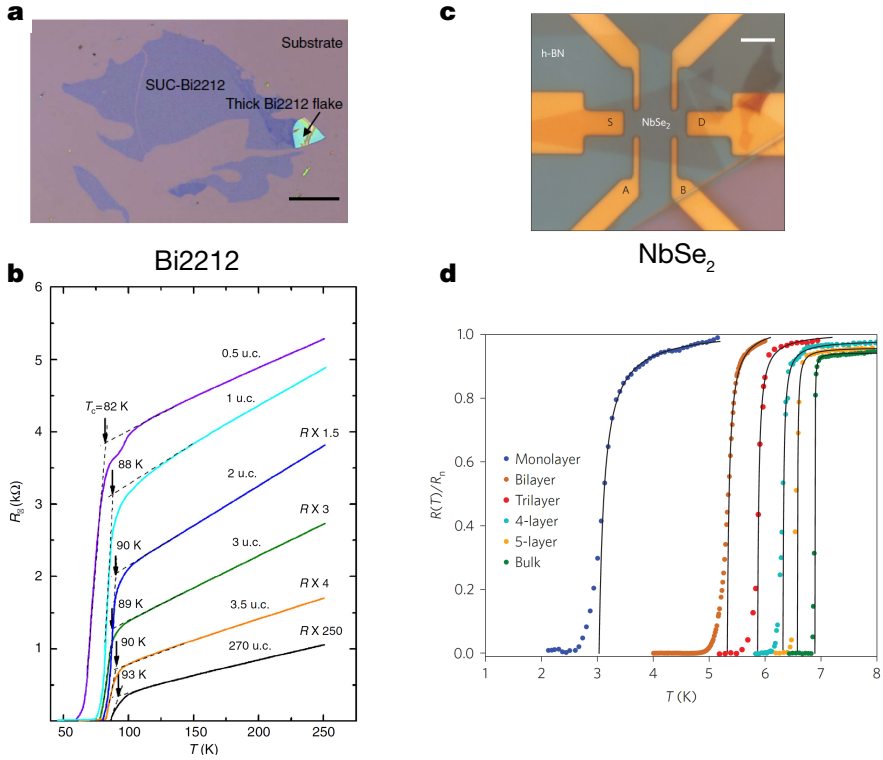

Figure 1.5 | Atomically thin superconductors based on exfoliated 2D crystals. **a**, Optical microscope image of several $Bi_2Sr_2CaCu_2O_{8+x}$ (Bi2212) flakes [25].**b**, Temperature dependent sheet resistance for Bi2212 multilayer flakes with different thicknesses from half-unit-cell thick to 270-unit-cell thick. **c**, Optical micrograph of four terminal $NbSe_2$ devices covered by *h*-BN. **d**, Thickness variation of resistive superconducting transition of $NbSe_2$ thin flakes.

tude of controllable carrier density. The reachable carrier density by the field effect is limited because of the dielectric breakdown, and usually is not enough to induce superconductivity in insulators and to control T_c in a wide range. To solve this bottleneck, a different type of electrostatic doping technique using a liquid gate, which is realized in the EDLT configuration, has been developed [137−139]. The basic concept for carrier doping in EDLT is similar to that in conventional FET structure, where an ionic liquid or electrolyte is employed as a gate medium instead of solid gate dielectric (Figs. 1.6a and b; Figure 1.6a shows a typical optical image of MoS_2 thin flake device). According to this replacement of gate material, the EDLT enables us to apply a large electric field over 10 MV/cm at a liquid/solid electrochemical interface and accumulate the extremely high carrier densities over 10^{14} cm^{-2} [140] by forming an EDL with

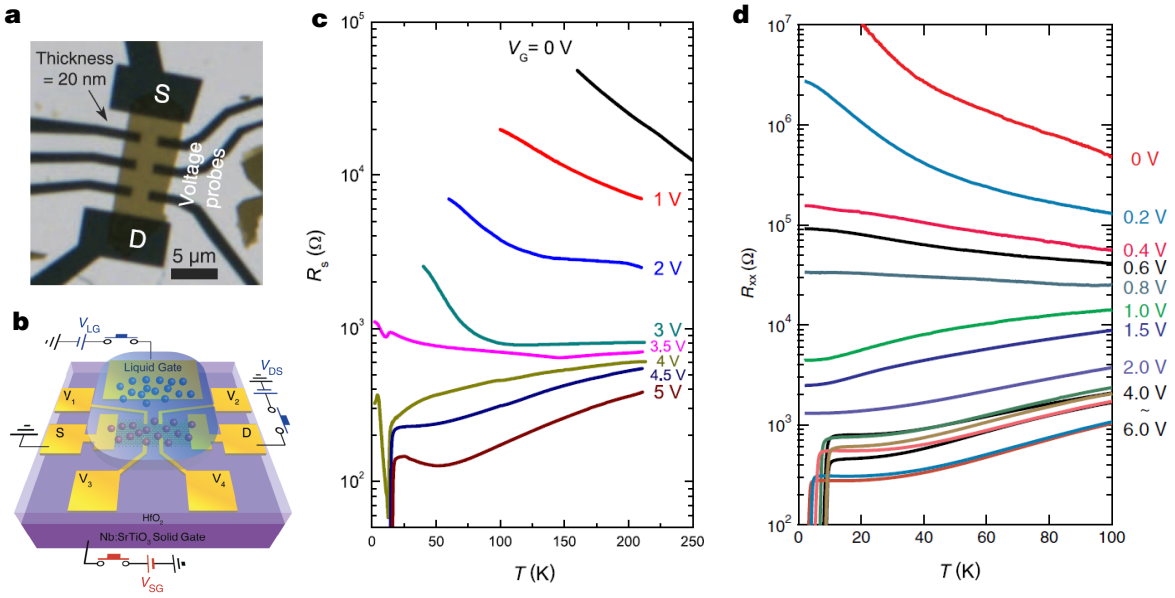

Figure 1.6 | Electric-field-induced superconductivity in 2D crystals. a, An optical image of a MoS_2 thin flake EDLT device before putting an ionic liquid. **b**, A schematic of an EDLT device. **c**, **d**, Insulator-to-superconductor transitions in ion-gated ZrNCl (**c**) [29] and MoS_2 (**d**) [30].

a $\sim$ 1-nm-gap near the surface, which can be regarded as a nanometer-gapped capacitor [141]. While the function of the prototype transistor with electrolyte was examined in very early studies in some materials including organic semiconductor [142] and cuprate superconductors [143], this technique has dramatically been improved in 2000's and became key tool to realize the electric-field-induced superconductivity on the surface of $SrTiO_3$ [28], which is originally a band insulator. After this success, the EDLT has become a promising tool for the search of superconductivity, as exemplified by gate-induced or tuned superconductivity in $KTaO_3$ [144], quasi-2D layered ZrNCl [29], TMDs [30, 31, 145−147] and cuprate thin films [148−151] in addition to $SrTiO_3$ [28, 152, 153]. In particular, ZrNCl and MoS_2 were investigated in detail as for *R*-*T* curve at different gate voltages (Fig. 1.6c and d) [30, 36].

One of the greatest advantages of the EDLT is its easy accessibility to a wide range of materials because we do not have to grow the solid dielectric thin film on the top of channel materials in contrast to the usual FETs. Indeed, methods of EDLT are now applied to the studies for not only superconductivity but also other physical phenomena, such as ferromagnetism,

metal-insulator transitions, tuning of SOI and valleytronics [114, 147, 154−158].

2
Experimental

2.1 Mechanical exfoliation

First of all, we prepare two kinds of Scotch-tape for mechanical exfoliation of single crystals. One is a blue color Scotch-tape (ULTRON SYSTEMS, Inc. Dicing Tape 1007R), which is less sticky and useful for materials with weak van der Waals force such as graphene, TMDs and black phosphorus. The other is a white color tape (3M Inc.), which is stickier and maybe useful for materials with strong van der Waals force such as FeTe and $IrTe_2$. In the next, we put a small bulk single crystal (grown *via* chemical vapor transport method) on a tape. Then, we fold the scotch tape and unfold it slowly to mechanically exfoliate into the thin flakes. After repeating this procedure for several times, attach the scotch tape on the top of the substrate, and carefully remove the tape from the top of the substrate. We can see many flakes using an optical microscope. After this process, we measure the thickness of the obtained flakes by AFM or immediately cover the surface by spin-coating of resist. The bake time of the resist is the following: After spin-coating, 180 °C for 1 min for PMMA, 150 °C for 3 min for ZEP520A.

As a next step, we explore flakes which are suitable for the transport or optical mea-

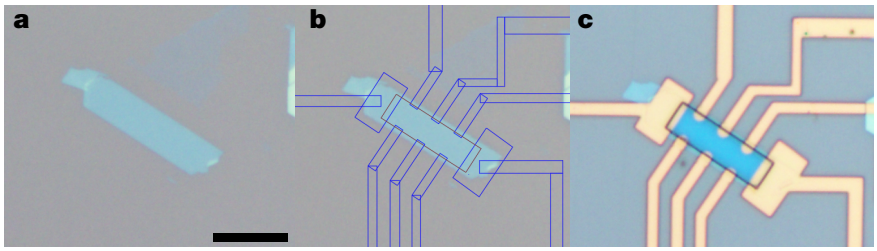

Figure 2.1 | Nanofabrication process. a, The mechanically exfoliated flakes after spin-coating. The scale bar means 5 μm.**b**, Typical design of electrodes by AutoCAD. **c**, After the lift-off process.

surements with an optical microscope. We primarily select flakes which have atomically flat surfaces by the sight of uniformity of reflection or using atomic force microscopy (Fig. 2.1a). If the surface of flake is not flat, the carriers transporting on the surface are scattered and mobility declines. This condition can badly affect the results of the experiments. Then, we estimate the thickness of the flakes by the color of the surface with an optical microscope. The difference of color of the surface is caused by optical interference on the thin flakes, which tells us the approximate value of the thickness. Also, using the dark-field (DF) mode, in which the light shined the edge of the flakes from the side, we can know the approximate value of the thickness. After searching the flakes by the optical microscope, we design a device pattern by AutoCAD (Fig. 2.1b), and perform the process of electron beam lithography. After finishing the process of electron beam lithography, we develop the pattern according with the following parameters: immersing the substrate in the mixed solution of methyl isobutyl ketone (MIBK) and IPA with the ratio of MIBK: IPA = 1: 3 in the case of PMMA, and Xylene for ZEP. The time of development may change depending on the environmental conditions such as humidity and temperature.

2.2 Deposition and lift off process

After the putting the substrate into an evaporator, we first deposit Cr or Ti of $\sim$ 5 nm as an adhesion layer under low enough vacuum condition (less than 10^{-4} Pa). In this time the rate of deposition is 0.02$-$0.03 nm/s. Next, we deposit Au of appropriate thickness (typically,

80−100 nm) with the rate of 0.1−0.2 nm/s. To prevent unintentional electrochemical reaction on gold because of the ionic liquid, we deposit SiO_2 with the thickness of 5−10 nm as a protection layer. We select one device and immerse it into NMP at 50 °C for 1 hour in order to remove redundant PMMA and gold. Only the fabricated electrodes are remained on the substrate. After lift-off process, we wash the substrate by IPA and dry it by nitrogen gun (Fig. 2.1c). Also, we cover the electrode near the flakes by putting SiO_2 or resist (PMMA or ZEP520A) in order to reduce the exposed electrode area to ionic liquid, or define the channel area right above the flake. Finally, we connect gold pads to a chip-carrier using wire-bonder just before measurement.

2.3 Measurement system

The resistance measurements of an EDLT under both zero and finite magnetic fields are made using a standard four-probe geometry in a Quantum Design Physical Property Measurement System (PPMS), combined with two kinds of AC lock-in amplifiers (Stanford Research Systems Model SR830 DSP and Signal Recovery Model 5210). The gate voltage is supplied by a Keithley 2400 source meter. We apply gate voltages to the device at 220 K under high vacuum (less than 10^{-4} Torr), and cool down to low temperatures. We measure the temperature dependent resistance under magnetic fields under a helium atmosphere (5 − 10 Torr) with a cooling speed of 1 K/min. All the measurements in chapter 3 are performed under the condition that the source-drain current, I_{DS}, is less than 1 μA, at which we confirm that the behavior of *R (T, B)* is completely unchanged.

In the cooling process of ion-gated semiconductor thin flakes, we frequently encountered the jump of the electrical resistance between 60 and 120 K, which hinders to measure the intrinsic properties at low temperatures. Although accurate reasons for this phenomenon have not been clear, there might be several possible reasons. One possible reason is the difference in the thermal expansion between gold and ionic liquid are different, which causes unintentional

strain of the contact. Second reason is the high Schottky barrier between semiconductor flakes and gold electrodes. Unlike oxides after the milling process and metallic thin flakes, the part beneath gold electrode is semiconducting or insulating, and thus the Schottky barrier (contact resistance) increases with decreasing temperatures. Another reason is the possible cracking of the ionic solid under cooling process, which causes the unintentional leak of the electric field at the sample surface. In addition to such reasons, the surface inhomogeneity or inhomogeneous charge accumulation, which depends on the samples, may cause unintentional jump of resistance due to, for example, sudden change of channel area.

3

Quantum phase transitions in ion-gated 2D crystalline superconductors

3.1 Introduction

Two-dimensional (2D) superconductors have been well-known platforms for the study of a QPT. In granular or amorphous superconducting thin films, which was the initial and highly disordered 2D superconductors with the atomic layer thickness, a direct SIT was a consequence of the QPT occurring at zero temperature. The SIT has been long discussed based on so called “ dirty-boson model ”, which is applied to the highly and homogeneously disordered systems. In this scenario, the ground state is either superconductor or insulator distinguished by a QCP, which is characterized by the critical sheet resistance and a critical tuning parameter for the degree of disorder, magnetic field or carrier density. Figure 3.1 shows a conventional generic phase diagram of 2D superconductors. While disorder-free superconductors show Abrikosov lattice state (zero resistance state) under magnetic fields from finite temperature to the ground state, the ground state of disordered superconductors is vortex glass phase. Experimentally, quantum phase transitions in disordered 2D superconductors have been intensively studied, the ground state of highly crystalline superconductors has been unexplored

because of the technical bottleneck.

One of the issues to be addressed in 2D superconductors is how zero electrical resistance is achieved or destroyed under magnetic fields in extremely weak disorder or pinning case at 0 K. In 2D superconductors exposed to out-of-plane magnetic fields, vortex pinning, which is necessary to achieve zero electrical resistance under magnetic fields, ideally becomes very weak compared to 3D ones. To address this question, superconductivity in vacuum-deposited metallic thin films has been studied in the previous studies [32, 33] as explained above [54]. The conventional way to approach the 2D limit is to reduce the film thickness, but this concomitantly increases disorder, which acts as the pinning center. In such thin films, a direct SIT is observed in most cases when the system is disordered; however, some metallic thin films with weak pinning show magnetic-field-induced intervening metallic state between superconducting and insulating such as MoGe [54] and Ta [13]. Therefore, investigation of 2D superconductivity in even cleaner systems is highly desirable.

As reviewed in chapter 1, recent technological advances of materials fabrication have led to discoveries of a variety of superconductors at heterogeneous interfaces and in ultrathin films; examples include superconductivity at oxide interfaces [21−23], electric-double-layer interfaces [28−31,131], and mechanically exfoliated [24−27], molecular-beam-epitaxy grown [16−20] atomically thin layers. These systems are providing opportunities for searching superconductivity at higher temperatures and for investigating the intrinsic nature of 2D superconductors, which are distinct from bulk superconductors because of enhanced thermal and quantum fluctuations due to a lower dimension.

In particular, despite five years of the past efforts from many groups by inducing many materials into superconducting states, this field lacks even basic understanding of the physical nature of electric-field-induced superconductors *via* ionic liquid gating. In fact, it has not even been established whether the simple Thomas-Fermi screening model can be applied in the emergent heterogeneous interfaces due to possible electronic and structural reconstructions at

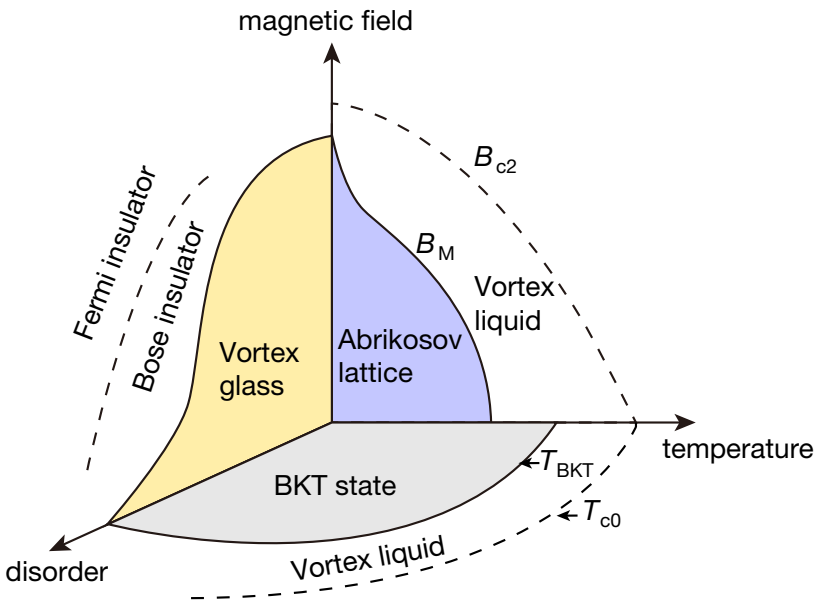

Figure 3.1 | Generic phase diagram of 2D superconductors as a function of temperature, magnetic field and disorder. This phase diagram is based on the previous studies [32, 159]. The crossover curve between the Fermi and Bose insulators does not continue by zero disorder region and does not reflect the possible emergence of a quantum metallic state. The ground state under a magnetic field in disorder-free 2D superconductors is occupied by the Abrikosov lattice. Once disorder is included, the ground state changes to vortex glass. At zero magnetic field, the ground state is the BKT state.

the interfaces or the electrochemical reaction occurs at the interface, and as a result the surface possibly becomes dirty. Thus, the basic understanding of electric-induced-superconductivity is important in terms of clarifying the intrinsic nature of 2D crystalline superconductors as well as properties of ionic-liquid/solid electrochemical interfaces. In this chapter, therefore, I focus ionic-liquid gating to produce highly crystalline 2D superconductors combined with 2D layered crystals, ZrNCl and MoS_2, both of which are layered semiconductors with honeycomb structures (Fig. 3.2) and investigate the intrinsic nature of superconductivity realized in such electrochemical interfaces.

In the following several sections, I provide comprehensive transport studies on ZrNCl-EDLTs to clarify the basic properties of electric-field-induced superconductivity, and also attack important issues related quantum states in 2D crystalline superconductors. First, we confirmed that ZrNCl-EDLTs show 2D superconducting nature based on various analyses. Sec-

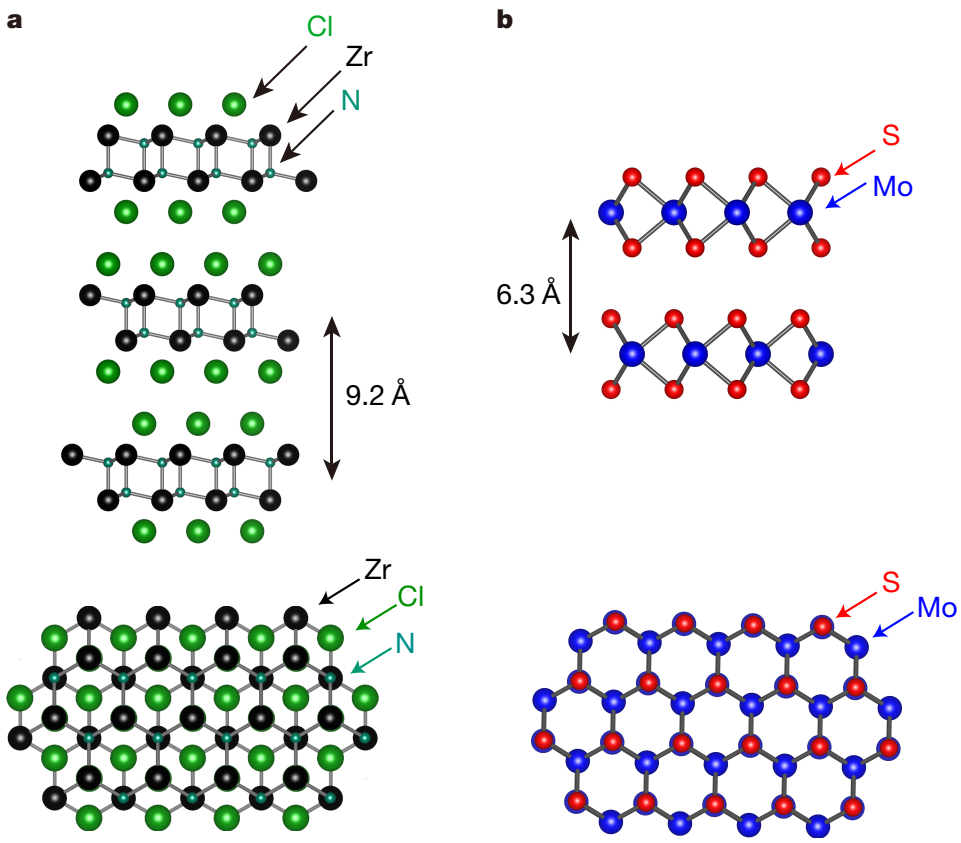

Figure 3.2 | Crystal structure of ZrNCl (a) and 2*H*-MoS_2 (b).

ond, we discovered that the zero-resistance state is immediately destroyed by the application of finite out-of-plane magnetic fields, and consequently, a quantum metallic state is stabilized in a wide range. This is a manifestation of the quantum tunneling of vortices due to the extremely weak pinning and quantum fluctuation at the 2D limit [36].

3.2 Two-dimensionality and superconducting fluctuation

ZrNCl is a band insulator with a layered crystal structure with honeycomb structure [160], in which a unit cell comprises three $(ZrNCl)_2$ layers. ZrNCl becomes a superconductor with a critical temperature, T_c, as high as 15 K by alkali-metal intercalation [161, 162] and field-effect doping [29]. We prepared a ZrNCl-EDLT using a mechanically exfoliated multilayer flake with a thickness of 20 nm without any monolayer steps. Also, we performed the cryogenic measurement at a sufficiently low excitation current. As shown in Fig 3.3a, the tem-

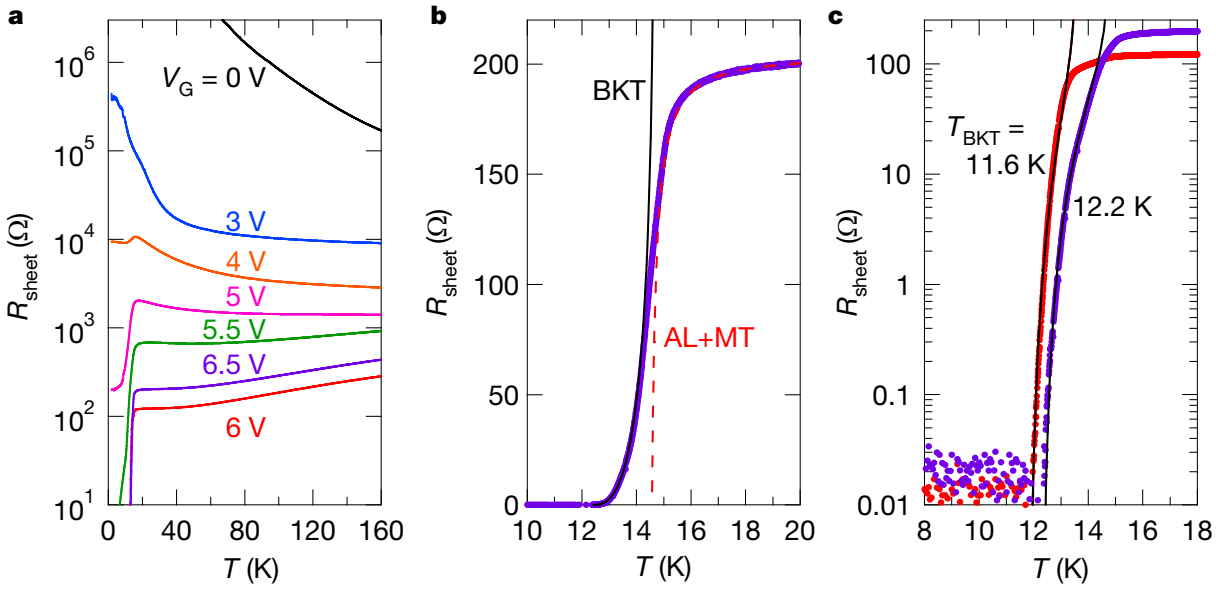

Figure 3.3 | Sheet resistance R_{sheet} as a function of temperature T at different gate voltages V_{G}, and superconducting fluctuations. **a**, R_{sheet} as a function of T at different V_{G}. We applied V_{G} at 220 K, followed by cooling down and scan the temperature dependent resistance. Signature of superconductivity appeared at 4 V. True zero resistance was achieved at 6 and 6.5 V. **b**, The temperature dependence of the resistance and fitting results. Red dotted line shows the AL and MT fitting. **c**, Temperature dependence of the resistance at 6 and 6.5 V and BKT fittings.

perature dependence of the sheet resistance, R_{sheet}, at different V_{G} values, the insulating state is dramatically suppressed with increasing V_{G}, and finally a resistance drop because of a superconducting (SC) transition appears at V_{G} = 4 V. Zero resistance state (below $\sim$ 0.05 Ω), namely BKT state (shown in later) was realized at V_{G} = 6 and 6.5 V. Despite the application of such relatively large gate voltages, any signature of electrochemical process was not observed in the present experiment.

The broadening of resistive transition observed in R_{sheet} as a function of T is interpreted as two-kinds of fluctuation: amplitude and phase fluctuation. The amplitude fluctuation causes paraconductivity above transition, which is a direct contribution that the Cooper pair originated from the fluctuation transports the current. This is called Aslamazov-Larkin (AL) term [44], which depends on the dimension of the system as shown below.

$$\sigma'_{\mathrm{3D-AL}} = \frac{e^2}{32\hbar\xi(0)}\epsilon^{-1/2} \tag{3.1}$$

$$\sigma'_{\mathrm{2D-AL}} = \frac{e^2}{16\hbar d}\epsilon^{-1} \tag{3.2}$$

In these equation, epsilon means

$$\epsilon \equiv \ln\left(\frac{T}{T_{\mathrm{c0}}}\right) \approx \frac{T - T_{\mathrm{c0}}}{T_{\mathrm{c0}}}. \tag{3.3}$$

First, we took only the AL term into account, and performed the nave fitting based on the following equation,

$$\left(\frac{1}{R_{\mathrm{sheet}}} - \frac{1}{R_{\mathrm{N}}}\right)^{-1} = R_0\left(\frac{T - T_{\mathrm{c0}}}{T_{\mathrm{c0}}}\right) \tag{3.4}$$

Here, R_0 and T_{c0} is the fitting parameters. Also, R_{N} is the normal state sheet resistance. We noted that R_0, is smaller by a factor of 3.0 than the value, which is supposed to be $e^2/16h$ in the original AL term. The correction for this excess conductance is possible if we consider the contribution of the Maki-Thompson (MT) term [44], which is similar *T* dependence with AL term close to T_{c0}. Indeed, we checked that this term does not affect the conclusion for two dimensionality of fluctuation conductance as shown below. In the next, the fluctuation analysis taking all the quantum fluctuation into account is described as following.

The analyses of $R(T)$ curves above T_{c} were performed based on the model of superconducting amplitude fluctuation [163], using the expression,

$$R(T) = \left(\frac{1}{R_{\mathrm{N}}(T)} + \Delta G_{\mathrm{SF}}\right)^{-1} \tag{3.5}$$

where G_{SF} is the excess conductance due to superconducting fluctuation (SF). In this work we adopted the formula for $R_{\mathrm{N}}(T)$,

$$\frac{1}{R_{\mathrm{N}}(T)} = \frac{1}{a + bT^2} + \ln\left(\frac{T}{T_0}\right) \tag{3.6}$$

with a ,b, c and T_0 as T-independent fitting parameters. The second term comes from the contributions of the weak localization (WL) and the Coulomb interaction between particles with

nearly the same momenta (ID), which are remarkable in dirty 2D systems [164]. For V_{G} = 6.5 V, we obtained the function form of $R_{\mathrm{N}}(T)$ by fitting the $R(T)$ curve at B = 9 T, where the contribution of SF can be ignored since $B_{\mathrm{c2}}^{\perp}(0) \approx$ 2 T, with $a = 1.92 \times 10^2$ Ω, $b = 8.25 \times 10^{-3}$ Ω/K^2, c = 3.47×10^{-4} Ω^{-1}, and T_0 =52.8 K. We also checked that the first Drude term in eq. 3.6 can reproduce $R(T)$ curve at 0 T above T = 50 K, where the quantum contributions (logarithmic term by WL and ID) are negligible. SFs are commonly comprised of three principal contributions: the AL process [44], the anomalous MT process, which is described as an indirect effect of the Cooper pairs after decaying into pairs of quasiparticles and dominant in clean 2D superconductors [45], and the depression in the electronic density of states (DOS) due to their involvement in fluctuation pairings [165, 166]. Using these contributions, the conductance of SFs are given by [163]

$$\Delta G_{\mathrm{SF}} = \Delta G_{\mathrm{AL}} + \Delta G_{\mathrm{MT}} + \Delta G_{\mathrm{DOS}} \tag{3.7}$$

$$= \frac{e^2}{16\hbar}\left(\frac{T_{\mathrm{c0}}}{T - T_{\mathrm{c0}}}\right) + \frac{e^2}{8\hbar}\frac{T_{\mathrm{c0}}}{T(1-\Delta) - T_{\mathrm{c0}}} \tag{3.8}$$

where T_{c0} is the temperature at which the finite amplitude of the order parameter develops, and δ is the pair-breaking parameter. As shown in Fig. 3.3b, the experimental data are well fitted by eq. 3.5, taking eq. 3.6 and eq. 3.8 into account, when δ = 0.05 T and T_{c0} = 14.65 K. We note that the value of δ = 0.05 is relatively larger when considering the small normal sheet resistance. This might originate from the strong spin orbit interactions generated by the inversion symmetry breaking due to an external electric field. Therefore, we can conclude that a ZrNCl-EDLT is a 2D superconductor in terms of amplitude superconducting fluctuation, which can be explained by AL and MT term.

With further increasing temperature, the system goes into phase fluctuation regime, and finally zero resistance state is achieved with the Berezinskii-Kosterlitz-Thouless (BKT) transition [47, 48, 49]. The BKT transition is a topological phase transition. In the phase fluctuation regime, the same number of vortex and antivortex pairs thermally and spontaneously created and annihilated, and at the BKT transition temperature, those vortices and antivortices

are bound as pairs. At $T < T_{\mathrm{BKT}}$ the zero resistance state is realized, while at $T > T_{\mathrm{BKT}}$ the vortex or the antivortex drift by the Lorentz force, and thus the finite resistance is generated. Also, Lorentz force originating from the current affects the vortices and antivortices to the opposite direction, therefore much enough current-induced Lorentz force causes dislocation-antidislocation pairs to unbind. This effect is reflected in the current-voltage characteristics. At $T < T_{\mathrm{BKT}}$ the linear relationship, $V \propto I$is realized, while at $T > T_{\mathrm{BKT}}$ the non-linear relationship, $V \propto I^a (a = 3)$ is realized. This universal jump of a is a feature of the BKT transition.

The experimental data are consistent with the BKT transition and no deviation from the BKT down to the experimental limit under zero magnetic field. This data indicates that we do not have to consider the finite size effect [167]. We used the Halperin-Nelson equation [168], for the analysis of the BKT transition, which shows square-root-cusp behavior that originates from the energy dissipation owing to Bardeen-Stephen vortex flow above the BKT transition temperature.

$$R_{\mathrm{sheet}} = AR_{\mathrm{N}} \exp\left[-2b\left(\frac{T_{\mathrm{c0}} - T}{T - T_{\mathrm{BKT}}}\right)^{1/2}\right] \tag{3.9}$$

where A and b is the constant of order unity and system-dependent parameters. As you can see, the experimental data are completely consistent with a BKT transition and there is no deviation from the BKT analysis down to the experimental limit (about 0.01 Ω) at zero magnetic field. Therefore, we believe that the finite-size effects can be excluded in our experiments.

We summarize the results of the superconducting fluctuations in Fig. 3.3b. The purple curve shows experimental data, red curve shows the amplitude fluctuation and black dashed curve shows the BKT transition. Near the transition temperature, the experimental data are well fitted by the amplitude fluctuation including AL and MT term. The BKT transition was observed at both 6 and 6.5 V (Fig. 3.3c).

To decide the upper critical field for each angle, we investigated the angular dependence of magnetoresistance. We used the Horizontal Rotator Probe for PPMS (Quantum Design,

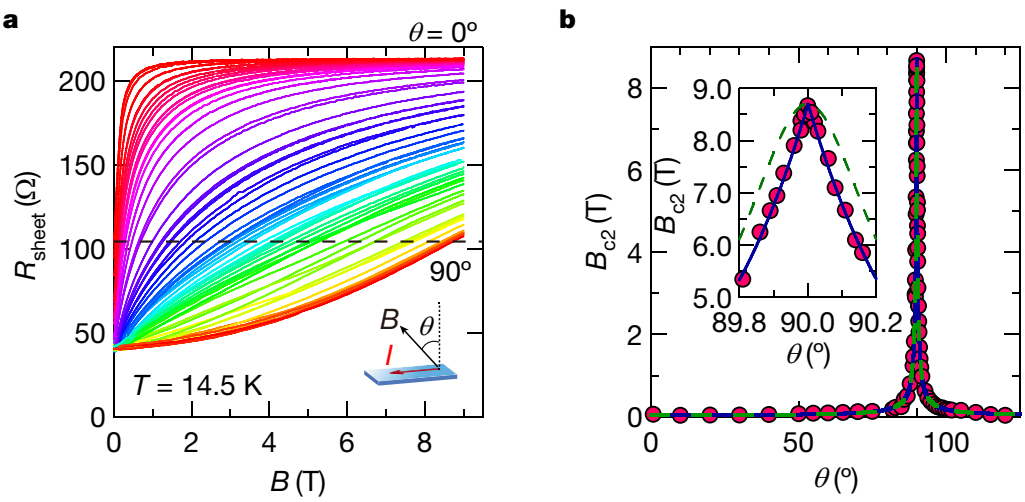

Figure 3.4 | Angular dependence of upper critical field in the ZrNCl-EDLT. a, Angular dependence of the magnetoresistance in the ZrNCl-EDLT. Dashed line is the half resistance of R_{N}. **b**, The cusp shape at peak is well fitted 2D Tinkham model $\left|\frac{B_{\mathrm{c2}}(\theta)\cos\theta}{B_{\mathrm{c2}}^{\perp}}\right| + \left(\frac{B_{\mathrm{c2}}(\theta)\sin\theta}{B_{\mathrm{c2}}^{\parallel}}\right)^2 = 1$. On the other hand, the 3D anisotropic effective mass model, $\left|\frac{B_{\mathrm{c2}}(\theta)\cos\theta}{B_{\mathrm{c2}}^{\perp}}\right| + \left(\frac{B_{\mathrm{c2}}(\theta)\sin\theta}{B_{\mathrm{c2}}^{\parallel}}\right)^2 = 1$,cannot be fitted especially at peak.

Inc.), and the angle θ is precisely determined within the error below 0.01 degree. Fig. 3.4a shows the angular dependent magnetoresistance in the ZrNCl-EDLT. As shown in this figure, magnetoresistance of ZrNCl is very anisotropic and in-plane magnetoresistance clearly shows very large upper critical field, although the resistance is not zero at that temperature. We plotted the upper critical field B_{c2} (θ) extracted from Fig. 3.4a as a function of angle θ between the c-axis and the direction of magnetic field in Fig. 3.4b, in which θ represents the angle between the c-axis of the crystal and applied magnetic field directions at 14.5 K just below T_{c}. T_{c} was defined as the temperature in which R_{sheet} becomes 50% of R_{N} at 30 K. The reason why we have to do this measurement at just below transition temperature is that the in-plane upper critical field is very large. A cusp-like peak was clearly resolved at θ = 90 degree (the inset of Fig. 3.4b), which is qualitatively different from the 3D anisotropic mass model.

$$\left(\frac{B_{\mathrm{c2}}(\theta)\cos\theta}{B_{\mathrm{c2}}^{\perp}}\right)^2 + \left(\frac{B_{\mathrm{c2}}(\theta)\sin\theta}{B_{\mathrm{c2}}^{\parallel}}\right)^2 = 1 \tag{3.10}$$

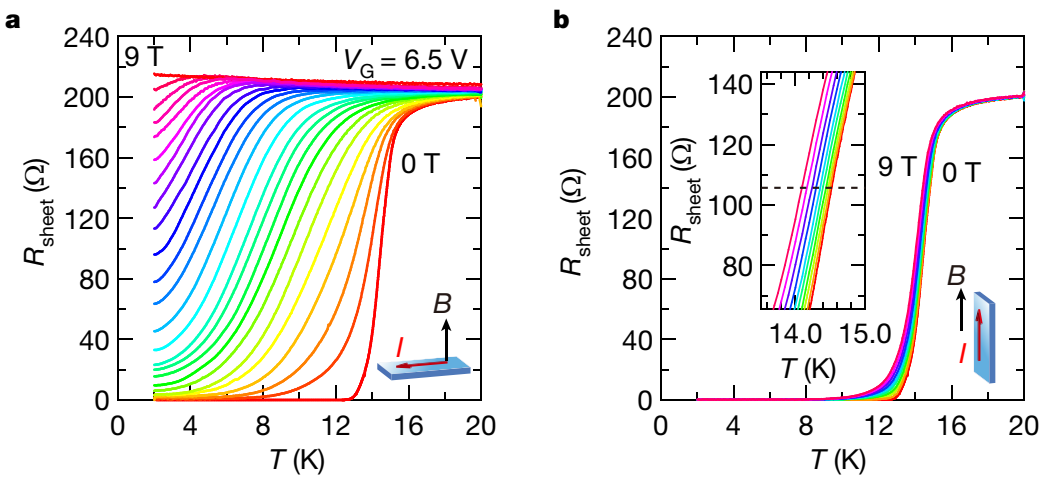

Figure 3.5 | R_{sheet} of the ZrNCl-EDLT as a function of T at V_{G} = 6.5 V, for **a** perpendicular magnetic fields $B_{\mathrm{c2}}^{\perp}$ varying in 0.05 T steps from 0 to 0.1 T, in 0.1 T steps from 0.2 to 0.8 T, and in 0.15 T steps from 0.9 to 2.7 T, and of 3 and 9 T, and **b** parallel magnetic fields $B_{\mathrm{c2}}^{\parallel}$ varying in 1 T steps from 0 to 9 T, respectively. The inset of Fig. 3.5b is the magnification near half resistance. Dashed line is the half resistance of R_{N}.

but well described by the 2D Tinkham model,

$$\left|\frac{B_{\mathrm{c2}}(\theta)\cos\theta}{B_{\mathrm{c2}}^{\perp}}\right| + \left(\frac{B_{\mathrm{c2}}(\theta)\sin\theta}{B_{\mathrm{c2}}^{\parallel}}\right)^2 = 1 \tag{3.11}$$

Figures 3.5a and b display temperature-dependent $R_{\mathrm{sheet}}(T)$ values at V_{G} = 6.5 V for magnetic fields applied perpendicular and parallel to the surface of ZrNCl, respectively. For the out-of-plane magnetic fields, T_{c} is dramatically suppressed with a considerable broadening of the SC transition even at a small magnetic field of $B = 0.05$ T, which is in marked contrast to those observed in the in-plane magnetic field geometry. Such a large anisotropy suggests that the superconductivity is strongly 2D in nature and indicates a significant contribution of the vortex motion in the out-of-plane field geometry. Figure 3.6a shows the temperature dependence of B_{c2} at θ = 90 degree and at θ = 0 degree, which exhibits a good agreement with the phenomenological GL expressions for 2D SC films:

$$B_{\mathrm{c2}}^{\perp} = \frac{\Phi_0}{2\pi\xi_{\mathrm{GL}}(0)^2}\left(1 - \frac{T}{T_{\mathrm{c}}}\right) \tag{3.12}$$

$$B_{\mathrm{c2}}^{\parallel} = \frac{\Phi_0\sqrt{12}}{2\pi\xi_{\mathrm{GL}}(0)d_{\mathrm{SC}}}\sqrt{1 - \frac{T}{T_{\mathrm{c}}}} \tag{3.13}$$

where Φ_0 is the flux quantum, $\xi_{\mathrm{GL}}(0)$ is the extrapolation of the GL coherence length, ξ_{GL}, at $T = 0$ K, and d_{SC} is the temperature-independent SC thickness. As a result of the fit, we obtained $\xi_{\mathrm{GL}}(0)$ = 12.8 nm and d_{SC} = 1.8 nm. The latter parameter approximately corresponds to the bilayer thickness of the $(ZrNCl)_2$ layer, which is less than one-unit-cell thick. The estimated thickness is indeed in the atomic scale, and demonstrates that the superconductivity persists to the extreme 2D limit. The d_{SC} for this system is much smaller than the reported value of approximately of 11 nm for the interface superconductivity on $SrTiO_3$ [169], which is presumably owing to the huge dielectric constant in the incipient ferroelectric $SrTiO_3$. Recently, it was suggested based on theoretical calculations that the depth of the induced charge carriers in ion-gated superconducting ZrNCl is only one layer [170]. The difference from the present observation might be ascribed to the proximity effect of the superconductivity, which is a phenomenon whereby the Cooper pairs in a SC layer (the topmost layer, in the present case) diffuse into the neighboring non-SC layers (the second layer), resulting in broadening of the effective thickness (see Fig. 3.6b). This could occur even if there are only a small number of electrons in the second layer. Another possibility for this discrepancy might come from the situation that the measured B_{c2} is suppressed because of the paramagnetic effect as compared with the orbital limit, leading to the estimated d_{SC} thicker than the real value.

In our system, we found that the Pippard coherence length, ξ_{Pippard}, is equal to 43.4 nm, as calculated from $\xi_{\mathrm{Pippard}} = \hbar v_{\mathrm{F}}/\pi\Delta(0)$ by using $v_{\mathrm{F}} = \hbar k_{\mathrm{F}}/m^*$ and the Bardeen-Cooper-Schrieffer (BCS) energy gap of $\Delta(0) = 1.76 k_{\mathrm{B}} T_{\mathrm{c}}$ = 2.2 meV, where $v_{\mathrm{F}}, k_{\mathrm{F}}, m^*, \hbar, s$ and s' are the Fermi velocity, the Fermi wave number, the effective mass, Planck's constant divided by 2π, the spin degree of freedom and the valley degree of freedom, respectively, for V_{G} = 6.5 V (the sheet carrier density of $n_{\mathrm{2D}} = 4.0 \times 10^{14}$ cm^{-2}) with T_{c} = 14.5 K and the effective mass of $m^* = 0.9 m_0$ [171]. Here s and s' are both 2. The Pippard coherence length is larger than k_{F}^{-1} = 0.28 nm, and much larger than $d_{\mathrm{SC}} \approx 1.8$ nm. We also note that the in-plane B_{c2} may exceed the Pauli limit for weak coupling BCS superconductors, $B_{\mathrm{P}}^{\mathrm{BCS}}$ = 1.86T_{c} = 27.0 T.

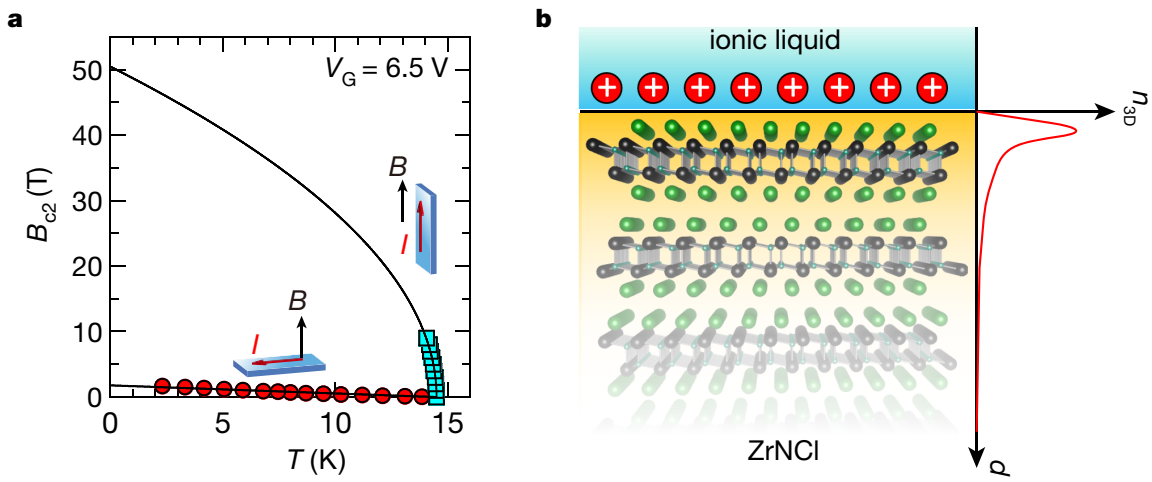

Figure 3.6 | Temperature dependence of B_{c2} perpendicular and parallel to the surface, $B_{c2}^{\perp}(T)$ and $B_{c2}^{\parallel}(T)$. **a**, Solid dashed curves correspond to theoretical curves obtained from the 2D GL equation. **b**, A shematic image of carrier profile of a ZrNCl-EDLT. Almost all carriers are accumulated on the topmost layer.

However, to confirm this phenomenon, it is necessary to investigate B_{c2} at lower temperatures by using high magnetic fields

Having estimated d_{SC}, we then compare the phase diagrams of electric-field-induced 2D and bulk superconductors [171] (Fig. 3.7). A direct comparison is made by using n_{2D} estimated from Hall effect measurements in ZrNCl-EDLTs and n_{2D} in the $(ZrNCl)_2$ bilayer for the bulk. In contrast to the bulk, where T_c abruptly appears at $n_{2D} = 1.5 \times 10^{14}$ cm^{-2} followed by a decrease with increasing n_{2D}, ZrNCl-EDLTs exhibit a gradual increase of T_c, forming a dome-like SC phase with a maximum T_c of 14.8 K at $n_{2D} = 5.0 \times 10^{14}$ cm^{-2}. The coincidence of the critical n_{2D} in the 2D and bulk system implies that the mysterious phase diagram in the bulk Li_xZrNCl; that is, an abrupt drop of T_c near $n_{2D} \sim 1 \times 10^{14}$ cm^{-2}, might be related to the quantum SIT phenomena realized in the 2D limit [144]. Similar dome-like SC phases have already been reported in EDLTs based on the band insulators $KTaO_3$ [144] and MoS_2 [30], suggesting a commonality among electric-field-induced 2D superconductors.

Scientifically, our system is dealing with is the electrochemical interface, which has a highly disordered arrangement of ions in the electrolyte side. One of the important discov-

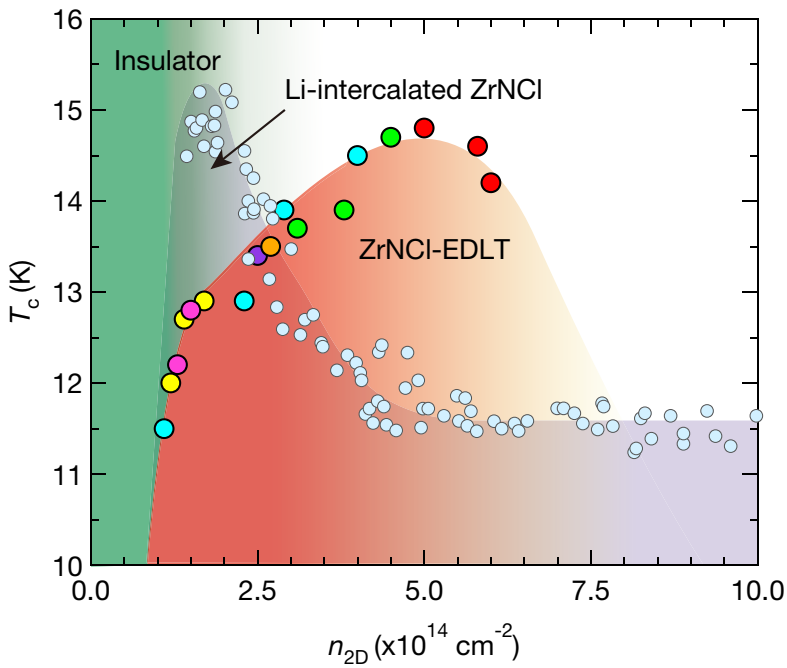

Figure 3.7 | Phase diagram of electric-field-induced and bulk superconductivity in ZrNCl. The SC transition temperature T_c (defined as the temperature where R_{sheet} reaches the half of R_N at 30 K) for ZrNCl-EDLTs was collected from seven different devices, indicated by the different color circles. The data for Li-intercalated ZrNCl were taken from ref.[172] and bilayer thickness was assumed for calculating the sheet carrier density n_{2D}. The sheet carrier densities for ZrNCl-EDLTs were determined by the Hall-effect measurements at 60 K.

eries of our work is that even such seemingly disordered electrochemical interfaces can be surprisingly a platform for investigating clean 2D superconductors, which is actually far from the dirty limit as explain below. Our work above proved this with five kinds of transport data and their analysis, including AL and MT fit, the BKT transition, the electronic phase diagram, anisotropic and angle dependence of B_{c2}.

3.3 Quantum metallic state

Let us return to discussing the sheet resistance behavior at the low temperature. In an Arrhenius plot of $R_{sheet}(T)$ for out-of-plane magnetic fields at V_G = 6.5 V (Fig. 3.8a), $R_{sheet}(T)$ exhibits an activated behavior just below T_c described by $R = R' \exp(-U(B)/k_B T)$, where k_B is Boltzmann's constant, as shown by the dashed lines. The magnetic field dependence of the extracted activation energy *U(B)* (Fig. 3.8b), and the relation between $U(B)/k_B T_c$ and

(Fig. 3.8c) are consistent with the thermally-assisted collective vortex-creep model in two dimensions [173], $U(B) \propto U_0 \ln(B_0/B)$ and $R' = U(B)/k_{\mathrm{B}}T_{\mathrm{c}}$, where $U_0 = \frac{C_{66}da_0^2}{\pi} = \frac{\phi_0^2}{256\pi^3\lambda^2}$, the activation energy necessary to nucleate a free dislocation-antidislocation vortex pairs, and causes plastic motion of dislocations of vortices. Here, C_{66}, a_0, ϕ_0, d and λ is shear modulus, flux line lattice constant, flux quantum, thickness and penetration depth, respectively. The activation energy becomes almost zero at B = 1.3 T, allowing the vortex flow motion above this field.

At low temperatures, on the other hand, R_{sheet} clearly deviates from the activated behavior and is flattened at a finite value down to low temperature even at $B \approx B_{\mathrm{c2}}$/40 (0.05 T). This implies that a metallic ground state exists for $B > 0$ and is possibly ascribed to the vortex motion driven by quantum mechanical processes. Here, we confirmed that the sheet resistance measurement of the excitation current, which means that the system is at the Ohmic regime. Our results are markedly distinct from conventional theories that predict a vortex-glass state and a direct SIT at T = 0 with R_{N} close to the quantum resistance $R_{\mathrm{Q}} = h/4e^2$ = 6.45 kΩ. The metallic ground state has been reported in MoGe [54] and Ta [13] thin film materials, where R_{N} ($\approx$ 1 kΩ) is smaller than R_{Q}. It is emphasized here that, in ZrNCl-EDLT, R_{N} at V_{G} = 6.5 V is 200 Ω, is even lower, as small as 1/30 of R_{Q}. The mean free path l ($\approx$24nm) is larger than $\xi_{\mathrm{GL}}(0)$, and $k_F l \approx 130-260$ ($R_{\mathrm{N}} \approx 100-200\ \Omega$) is much larger than the Ioffe-Regel limit ($k_F l \approx 1$), meaning that both the normal and SC states are relatively clean. Moreover, we failed in the scaling analysis for SIT using the $R_{\mathrm{sheet}} - T$ data under magnetic fields, which is expected in the disordered systems. The peculiar phenomenon is discussed in the following section.

All these features indicate that the ZrNCl-EDLT at V_{G} = 6.5 V is out of the disordered regime and potentially entering a clean regime with weak pinning. We also note that the estimated value of $l \approx 18$ nm results in the relation $\xi_{\mathrm{Pippard}} \cong 2.4l$, which is far from the dirty limit ($\xi_{\mathrm{Pippard}} >> l$). Indeed, the expression of $\xi_{\mathrm{GL}}(0)$ in the dirty limit, $0.855(\xi_{\mathrm{Pippard}}l)$, is

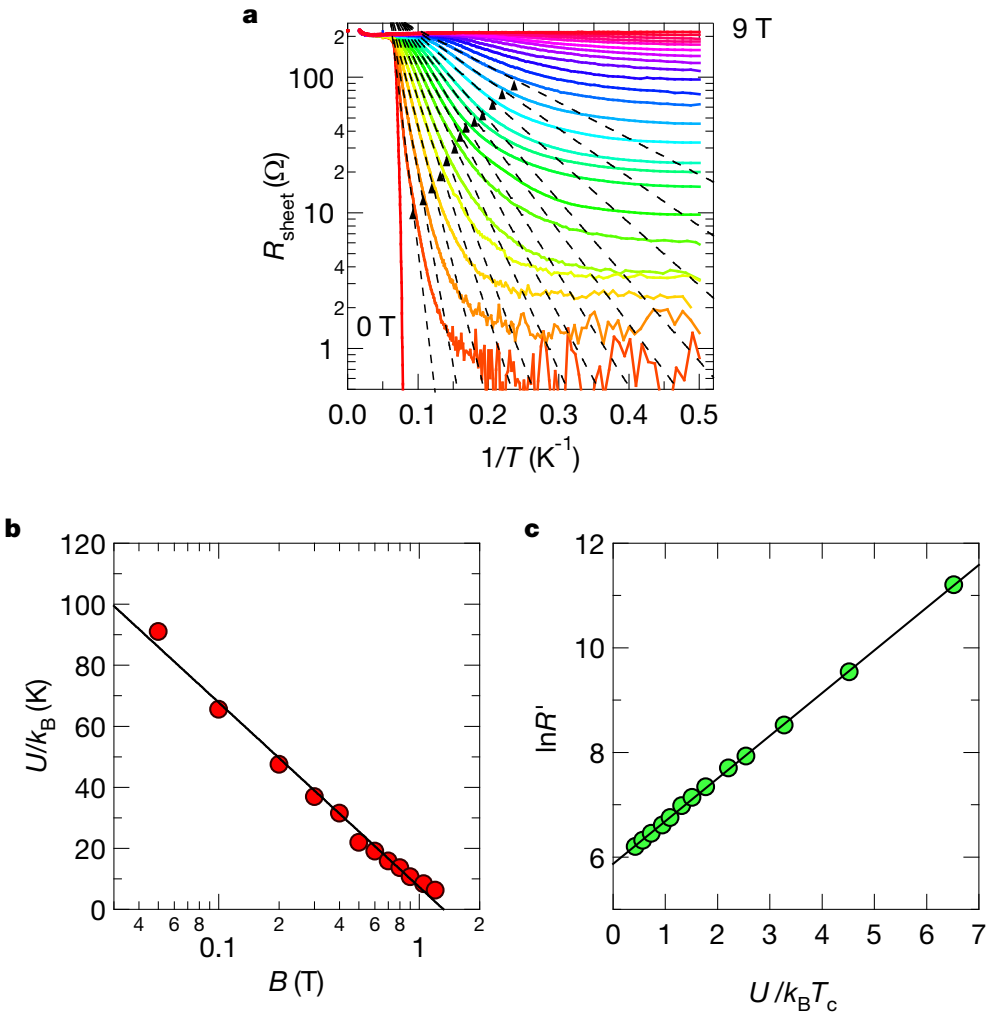

Figure 3.8 | Thermally-assisted collective vortex creep. a, Arrhenius plot of R_{sheet} of a ZrNCl-EDLT at V_{G} = 6.5 V for different magnetic fields perpendicular to the surface of ZrNCl. The black dashed lines demonstrate the activated behavior. The triangles separate the thermally activated state in the high-temperature limit and the saturated state at lower temperatures. **b**, Activation energy $U(B)$, which is derived from the slopes of the dashed lines in Fig. 3.8a, is shown on a semi-logarithmic plot as a function of magnetic field. The solid line is a fit by an equation. **c**, $\ln R'$ versus U/T_{c}. The combination of two kinds of linear plots indicates that the resistance is governed by the thermal activated motion of dislocations of 2D vortex lattice (2D thermal collective creep) [173].

not applicable to our result. We summarize the typical parameters of electric-field-induced superconductivity in ZrNCl and 2*H*-MoS_2 (MoS_2 will be discussed in the next several sections and chapters) in Table 3.1. Here, the calculation of resistivity assumes that the conducting layer is bilayer. It is noted that the resistivity in ZrNCl is two-order lower than that in polycrystalline Li_xZrNCl [172] and one-order lower than that in amorphous 2D superconductors [33], which

Table 3.1 | Typical parameters of electric-field-induced superconductivity. The calculation of resistivity assumes that the conducting layer is bilayer, and carrier distribution is homogeneous along to c-axis.

	T_c[max] (K)	$R_{\rm sheet}$ (Ω)	ρ ($\mu\Omega$cm)	$\xi_{\rm GL}$ (nm)	$\xi_{\rm Pippard}$ (nm)	L (nm)	μ (cm^2/Vs)
ZrNCl	15.2	100−200	20−40	10−15	30−50	20−50	100−300
MoS_2	10.8	100−200	15−30	5−10	50−70	30−70	200−600

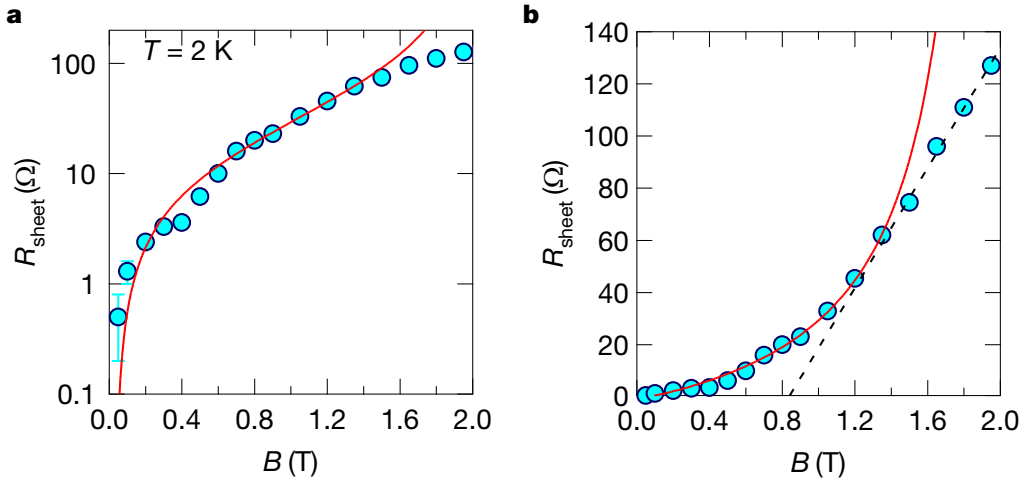

Figure 3.9 | The magnetoresistance at 2 K. **a**, Experimental data and fitting curve based on quantum creep model is white blue circles and red curve, respectively. **b**, Linear-scale plot of Fig. 3.9a. Dashed black line shows $R_{\rm sheet} - B$ linear behavior, suggestive of vortex flow.

indicate that the ion-gated ZrNCl is a highly crystalline 2D superconductor with low $R_{\rm N}$.

The most plausible description of the flattening of resistance in the low temperature is the T-independent quantum tunneling of vortices (quantum creep). In this model based on a percolating network, resistance obeys a general form in the limit of the strong dissipation,

$$R_{\rm sheet} \approx \frac{\hbar}{4e^2}\frac{\kappa}{1-\kappa}, \kappa \approx \exp\left[C\frac{(\hbar/e^2)}{R_{\rm N}}\left(\frac{B-B_{\rm c2}}{B}\right)\right] \tag{3.14}$$

where C is a dimensionless constant ($C \approx 0.005$).

As seen in Fig. 3.9a, the $R_{\rm sheet}$-B relation at 2 K is well fitted by the at up to 1.3 T over two orders of magnitude of $R_{\rm sheet}$, indicating that the quantum creep model holds in a wide range. The quantum creep means the plastic motion of dislocations of vortices due to the weak pinning and elasticity by the quantum fluctuation in sufficiently low temperatures. Such quantum creep state may be confirmed by the Nernst measurements. It is noted that recently

such quantum metallic state has been observed also in mechanically-exfoliated 2D $NbSe_2$ [38], which is one of the highly crystalline superconductors, and discussed in terms of possible Bose metal [174−177].

It should be noted that the model of random Josephson junction arrays that originate from surface roughness [179] or inhomogeneous carrier accumulation, both of which can cause the flattening of the resistance with a finite value, can be excluded because of following results took by the optical microscope. We took optical microscope and atomic-force microscope (AFM) images (Fig. 3.10a−3.10d) after the transport measurements. After the EDLT experiments, we removed the resist and took some AFM images. Some unclear lines in Fig. 3.10a are caused by the noise by the AFM. Figure 3.10b is the expanded view of the area enclosed by the yellow rectangle in Fig. 3.10a. Figure 3.10c shows the cross-sectional view along the blue line in Fig. 3.10b. Figure 3.10d shows the three-dimensional (3D) plot of Fig. 3.10b. From these AFM images, we found that the root-mean-square of the surface roughness is $\sim$ 0.068 nm, which is much smaller than the superconducting thickness $d_{\mathrm{SC}} \approx 1.8$ nm, and the thickness of one unit cell of ZrNCl ($\approx$ 2.7 nm). Such atomically flat surface excludes possibly inhomogeneous superconducting states caused by surface roughness, such as granular or Josephson junction array superconductivity where isolated superconducting islands are weakly coupled, indicating highly crystallinity of the present system. Also, all the different voltage probes used to measure the longitudinal resistances and the transverse Hall resistances in four-terminal geometry showed almost the same values with the differences of less than 5% at the high carrier concentrations (V_{G} = 6 and 6.5 V), which suggests the surface carrier accumulation in the present system should be homogeneous.

Above 1.3 T, R_{sheet} is well described as the B-linear dependence (Fig. 3.9b), suggesing that the crossover from the vortex creep to flow motion occurs at 1.3 T, where the activation barrier for the thermal creep approaches zero (Fig. 3.8b). This implies that the pinning or the elastic potential effectively disappears at high magnetic fields. Based on the above observa-

tions, we determined a $B - T$ phase diagram of ZrNCl-EDLT as shown in Fig. 3.11. A true zero resistance state occurs only at very small magnetic fields below 0.05 T, which is almost the zero field limit. The key parameters here are the dimensionality and R_{N} of the system.

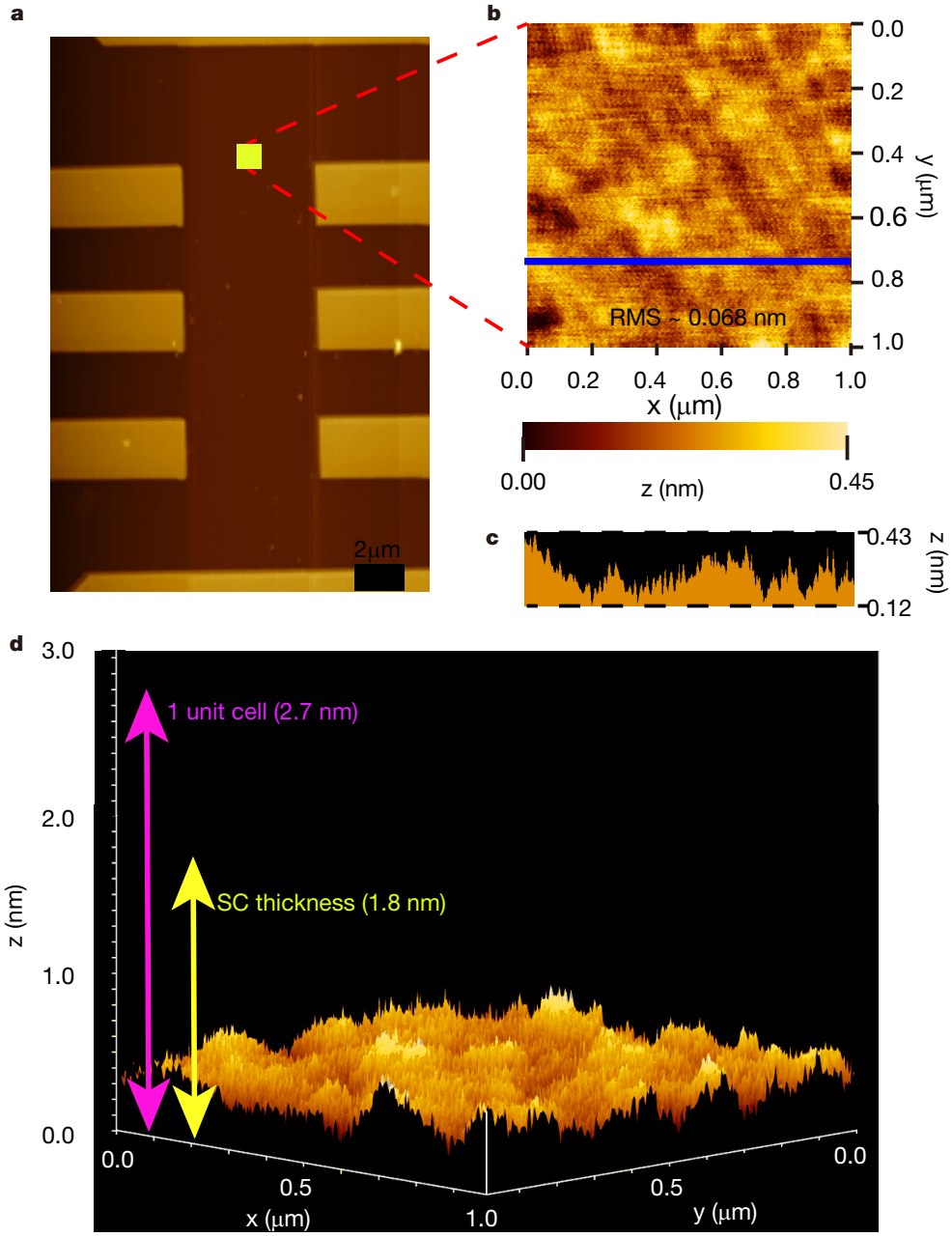

Figure 3.10 | AFM images of a ZrNCl device after EDLT measurements. **a**, The AFM images around channel area, and **b** the expanded view of the area enclosed by the yellow rectangle in Fig. 3.10a. **c**, A cross-sectional view of the blue line in Fig. 3.10b. **d**, 3D plot of Fig. 3.10b.

In particular, we emphasize that our findings of quantum metallic state in ion-gated

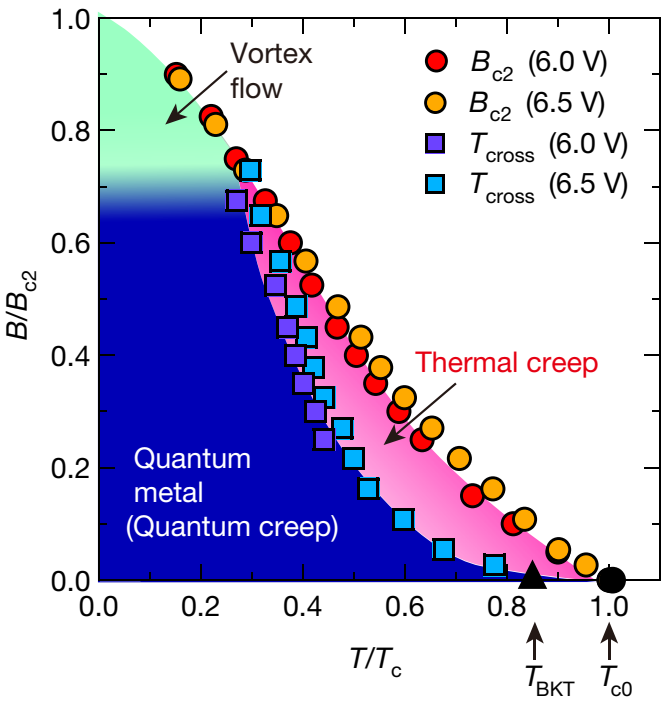

Figure 3.11 | Vortex phase diagram of the ZrNCl-EDLT. The boundary between the thermally-assisted vortex-creep regime and the quantum regime, T_{cross}, is determined from the Arrhenius plot as shown by the triangles in Fig. 3.8a. T_{BKT} is the BKT temperature and T_{c0} is the temperature extracted by the analyses of the superconducting amplitude fluctuation.

ZrNCl tells us that that the more crystalline 2D superconductors far from dirty limit are, the more easily zero-resistance is lost, sounds like counterintuitive at a glance, but is physically reasonable due to quantum fluctuations. This aspect has not been touched on in previous studies on recently found 2D superconductors, although this is a long-standing problem since 1990s when researchers discussed on metallic thin films. Our results uncovered this unique feature of 2D crystalline superconductors in a much more complete and clearer way, which is an important insight because 2D crystalline superconductors can more easily fabricated than decays ago. Finally, we conclude that the platform of gate tuned metals and superconductors, combining atomically smooth surface of single crystal with an electric field effect, is a tool to create 2D crystalline superconductors with extremely weak pinning, and has a tremendous potential for studying intrinsic quantum state without the additional complications of disorder that is unavoidable when systems are chemically doped, and clearly differentiates the system

from granular thin films.

3.4 Quantum Griffiths state

In the previous section, we discussed the quantum metallic state and possibly metallic ground state induced by small magnetic fields in highly crystalline 2D superconductors. As the magnetic field further increases, this state involving incoherent Cooper pairs is eventually broken and then weakly localized normal metal without Cooper pairs or insulating state appears through QPT. Although the resistance in the quantum metallic state is nonzero, this state starts far below the mean field upper critical field ($B_{\mathrm{c2}}^{\mathrm{MF}}$) without showing localized behavior. Thus, the crossover or transition from the quantum metallic state to the normal state at low temperatures including superconducting fluctuation regime, emerges as a new unsolved problem of the QPTs in highly crystalline 2D superconductors.

In this section, we propose a comprehensive $B-T$ phase diagram including superconducting fluctuation outside the mean field phase boundary of highly crystalline 2D superconductors. Based on the magneto-transport study in ion-gated ZrNCl and 2*H*-MoS_2, we found that these 2D superconducting systems commonly show the wide range of the quantum phase stemming from the very low magnetic field to a QCP beyond $B_{\mathrm{c2}}^{\mathrm{MF}}$. Especially, the observed QPT is characterized by the diverging behavior of critical exponent toward a QCP known as quantum Griffiths singularity. This implies that the critical phenomenon below the QCP is described by the exponentially small but nonzero probability of large ordered regions, so called rare regions. Such rare regions are interpreted as the superconducting puddles surviving in the normal state background with a long time and length scale at $T \to 0$ K, which evolves from the short-range ordered vortex state accompanied by the quantum vortex creep at low magnetic fields below $B_{\mathrm{c2}}^{\mathrm{MF}}$. Our result strongly indicates that quantum fluctuation governs the wide quantum metallic state and its crossover to the quantum Griffiths state consisting of superconducting puddles, leading to a generic feature of highly crystalline 2D superconductors.

We here use both ZrNCl and 2*H*-MoS_2 to investigate the universal nature of ion-gated 2D crystalline superconductors. We prepared EDLTs with those single-crystal flakes, in which almost all the carriers are accumulated in the topmost layer with thickness of 1∼2 nm at high gate voltages, resulting in truly 2D superconductivity at low temperatures as is explained in the previous section and next chapter.

Figure 3.12a displays temperature-dependent $R_{\mathrm{sheet}}(T)$ at V_{G} = 6.0 V (sheet carrier density n_{2D} is 4.8×10^{14} cm^{-2} at 30 K) for zero and finite B applied perpendicular to the surface of ion-gated ZrNCl. In zero magnetic field, the ZrNCl-EDLT exhibits superconductivity with a critical temperature T_{c} of 14.6 K. Here, T_{c} is defined as the temperature where R_{sheet} becomes 50% of the R_{N}, and is almost equal to the mean-field transition temperature T_{c0} estimated using thermal fluctuation theories [36]. By applying *B*, the resistive transitions considerably broadened because of the thermal phase fluctuation, and then level off at low temperatures due to the quantum phase fluctuation, indicating the quantum metallic state. Such a stable quantum metallic state does not appear in atomically ordered 2D superconductors grown by layer-by-layer growth with molecular-beam-epitaxy [85, 87], possibly because of the atomic steps of substrate working as strong pinning centers. In the mechanically-exfoliated 2D superconductors like ZrNCl, MoS_2 and $NbSe_2$, such atomic steps are basically absent.

A reliable determination of the mean field upper critical field $B_{\mathrm{c2}}^{\mathrm{MF}}(T)$ or transition temperature $T_{\mathrm{c}}^{\mathrm{MF}}(B)$ is indispensable to a proper understanding of the vortex state and various fluctuation effects, leading to the comprehensive description of the field−temperature (B-T) phase diagram. In two dimensional (2D) or highly anisotropic superconductors, however, the significant thermal fluctuation, which smears out the critical behavior at $B_{\mathrm{c2}}^{\mathrm{MF}}(T)$ or $T_{\mathrm{c}}^{\mathrm{MF}}(B)$ in the mean field theory, makes it difficult to obtain the appropriate value of it directly from the transport properties. For instance, the T dependence of electrical conductivity in B observed in this case is in rather continuous function of T from the normal to the vortex state without the divergence at $T_{\mathrm{c}}^{\mathrm{MF}}(B)$. It is well known that the AL type fluctuation theory assuming only

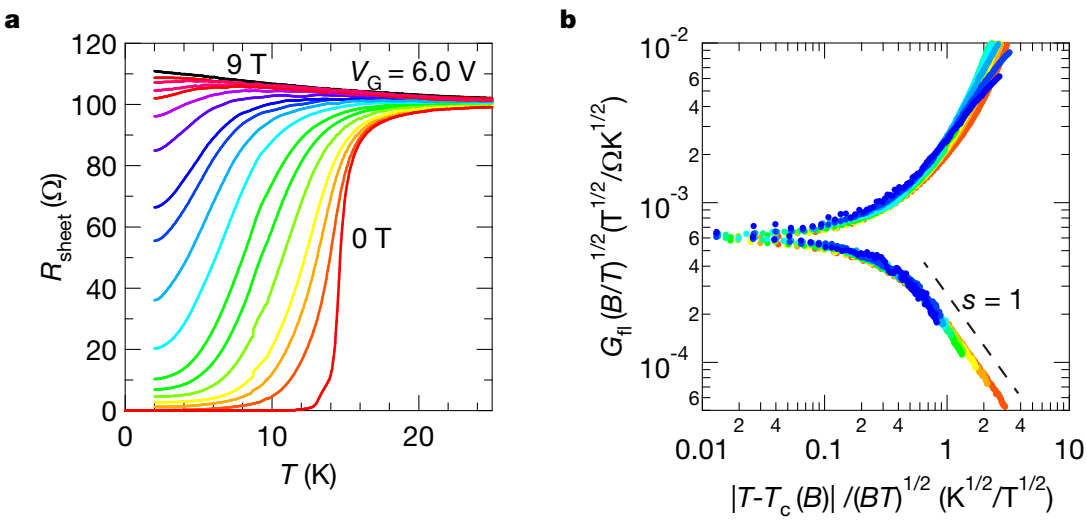

Figure 3.12 | Gate-induced-superconductivity in ZrNCl and Ullah-Dorsey scaling. a, R_{sheet} of a ZrNCl-EDLT as a function of T at V_{G} = 6.0 V, for perpendicular magnetic fields varying in 0.1 T steps from 0 to 0.3 T, in 0.2 T steps from 0.5 to 0.9 T, in 0.3 T steps from 1.2 to 1.8 T, in 0.5 T steps from 2.0 to 5.0 T, and in 1.0 T steps from 6.0 T to 9.0 T. **b**, Ullah-Dorsey (UD) scaling of fluctuation conductivity using the data of Fig. 3.12a from 0.1 to 1.8 T according to eq. 3.15

Gaussian fluctuations [44], implying no interaction between the fluctuations, fails to fit the conductivity just around $T_{\mathrm{c}}^{\mathrm{MF}}(B)$ due to this divergence.

In this work, in order to estimate $T_{\mathrm{c}}^{\mathrm{MF}}(B)$ from the temperature dependence of $R_{\mathrm{sheet}}(T)$ in B, we adopted the Ullah and Dorsey theory based on the time-dependent GL (TDGL) equation with the Hartree approximation [181], which takes into account the interaction between fluctuations [182]. This interpolates smoothly between the high-temperature Gaussian fluctuation regime and the low-temperature vortex-flow regime, resulting in successful fitting the transport properties of cuprates and low-T_{c} films [183, 184]. According to their scaling formula, the 2D conductance $G_{\mathrm{fl}}^{\mathrm{2D}}$ due to thermal fluctuations are given using the reduced temperature $t = T/T_{\mathrm{c}}^{\mathrm{MF}}(0)$ and field $b = B/B_{\mathrm{c2}}^{\mathrm{MF}}(0)$ as follows [181, 182].

$$G_{\mathrm{fl}}^{\mathrm{2D}} = C_0 A_0 \left(\frac{t}{b}\right)^{1/2} F\left(A_0 \frac{\epsilon_B}{(bt)^{1/2}}\right), \tag{3.15}$$

where $C_0 = \Gamma_0^{-1} m^* \xi(0)^2 / 4\pi\hbar^2 \Lambda_{T_{\mathrm{c}}}$, $A_0 = [d_{\mathrm{eff}} \Lambda_{T_{\mathrm{c}}} / (2\kappa^2 - 1)\xi^2(0)]^{1/2}$ and $\epsilon_B = t - 1 + b$ with Γ_0^{-1} the scattering factor, m^* the effective mass of electron, $\xi(0)$ the coherence length at zero temperature, $\Lambda_{T_{\mathrm{c}}} = \phi_0^2 / 4\pi\mu_0 k_{\mathrm{B}} T_{\mathrm{c0}}$ the thermal length at T_{c0} (= $T_{\mathrm{c}}^{\mathrm{MF}}(0)$) and d_{eff} the effective

thickness. The universal function $F(x)$, which is implicitly given by

$$x = \frac{1}{F(x)} + F(x), \tag{3.16}$$

leads to $F(x) \sim x^{-1}$ for $x >> 0$ and $F(x) \sim -x$ for $x << 0$. By using the GL expression of $B = B_{\mathrm{c2}}^{\mathrm{MF}}(0)(1 - T(T_{\mathrm{c}}^{\mathrm{MF}}(B)))$ near $T_{\mathrm{c}}^{\mathrm{MF}}(0)$, eq. 3.15 is transformed to

$$G_{\mathrm{fl}}^{\mathrm{2D}} \left(\frac{B}{T}\right)^{1/2} = \tilde{F}\left(\frac{T - T_{\mathrm{c}}^{\mathrm{MF}}(B)}{(BT)^{1/2}}\right), \tag{3.17}$$

where $F(x) = C_0 A_1 F(A_1 x)$ with $A_1 = A_0(B_{\mathrm{c2}}^{\mathrm{MF}}(0)/T_{\mathrm{c}}^{\mathrm{MF}}(0))^{1/2}$. By using this scaling law for the fluctuation conductance, which is equal to $1/R_{\mathrm{sheet}}(T) - 1/R_{\mathrm{N}}$ with the R_{N}, we can derive $T_{\mathrm{c}}^{\mathrm{MF}}(B)$ as a fitting parameter. As noted in [182, 183], the scaling law in Eq. 3.17 does not give the correct expression in the vortex flow regime due to the effect of pinning and the interaction between the vortices, which are not considered in the theory. Therefore, we used the scaling at high temperature above $T_{\mathrm{c}}^{\mathrm{MF}}(B)$.

As shown in Fig. 3.12b, by using $R_{\mathrm{sheet}}(T)$ at B = 9.0 T as $R_{\mathrm{N}}(T)$ and $T_{\mathrm{c}}^{\mathrm{MF}}(B)$ as fitting parameters, $G_{\mathrm{fl}}(T)$ curves in the ZrNCl-EDLT at $T > T_{\mathrm{c}}^{\mathrm{MF}}(B)$ and B = 0.1−1.8 T collapse onto a single curve with the slope of -1 in log-log plots, obeying the UD scaling law of eq.3.15. Then, we plotted $T_{\mathrm{c}}^{\mathrm{MF}}(B)$ or $B_{\mathrm{c2}}^{\mathrm{MF}}(T)$ as shown in Fig. 3.16a together with the superconducting onset temperature and field, T_{onset} and B_{c}, which are defined later. The $T_{\mathrm{c}}^{\mathrm{MF}}(B)$ at 0.1 T is close to the temperature for 50% of R_{N}. With increasing B, $R_{\mathrm{sheet}}(T_{\mathrm{c}}^{\mathrm{MF}})/R_{\mathrm{N}}$ increases and goes over 90% around $T_{\mathrm{c}}^{\mathrm{MF}}(B) \sim T_{\mathrm{c0}}/2$. At lower temperatures below $T_{\mathrm{c0}}/2$, where the UD scaling theory does not holds [181], we simply defined $T_{\mathrm{c}}^{\mathrm{MF}}(B)$ as the temperature for 95% of R_{N}. $T_{\mathrm{c}}^{\mathrm{MF}}(B)$ or $B_{\mathrm{c2}}^{\mathrm{MF}}(T)$ thus obtained obeys the Wertharmer-Helfand-Hohenberg (WHH) theory [185] as shown in the dashed curve in Fig. 3.16a. By using the similar process as the ZrNCl-EDLT, we determined $T_{\mathrm{c}}^{\mathrm{MF}}(B)$ or $B_{\mathrm{c2}}^{\mathrm{MF}}(T)$ curve of the MoS_2-EDLT as shown in Fig. 3.16b.

After knowing the mean field curve, we next investigate the superconducting onset. Figures 3.14 show the magnetoresistance at various temperatures in ZrNCl and MoS_2. In both

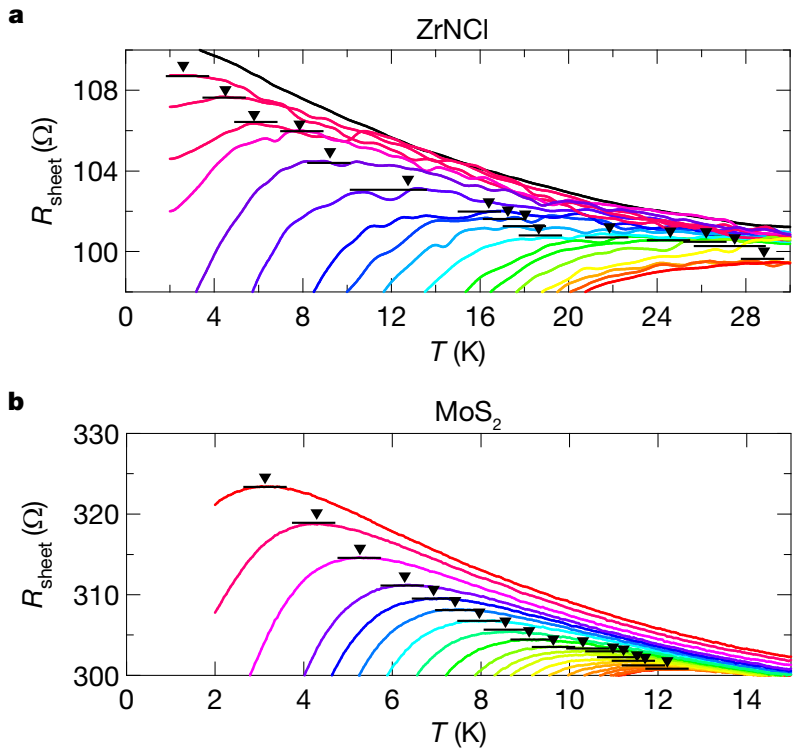

Figure 3.13 | Close-ups of the R_{sheet} as a function of temperature for ion-gated ZrNCl (a, c) and MoS_2 (b, d). a, **b**, R_{N} as a function of temperature at zero magnetic field for ZrNCl (**a**) and MoS_2 (**b**). The black dashed line is a linear fitting before the superconducting transition. The arrows show Tonset at zero magnetic field. **c**, **d**, R_{sheet} as a function of *T* in out-of-plane magnetic fields for ZrNCl (**c**) and MoS_2 (**d**). The applied magnetic fields are 0.1, 0.2, 0.3, 0,5 and 0.7 T, and vary in 0.3 T steps from 0.9 T to 1.8 T and in 0.5 T steps from 2 T to 5 T, and 7 and 8.5 T for ion-gated ZrNCl. They are 0.05, 0.1, 0.2 and 0.4 T, and vary in 0.3 T steps from 0.6 T to 3 T, in 0.5 T steps from 3.5 T to 6 T and in 1 T steps from 7 T to 9 T for ion-gated MoS_2.

cases, the isotherms show multiple crossing points, indicating that each $R - B$ curve cross at different points. The cross points of $R - B$ curves at neighboring temperatures, which are defined as $B_{\text{c}}(T)$, are plotted in Figs. 3.16a and b as orange squares. In these figures, we also plot the onset temperature T_{onset} of resistance drop in a magnetic field, defined by the temperature where $dR_{\text{sheet}}/dT = 0$

To complete the $B - T$ phase diagram, we determined the onset temperature of superconducting fluctuation T_{onset} from the $R - T$ curve at zero and finite magnetic fields as following. The resistance drop in superconducting transition starts to occur at much higher temperature than T_{c}^{MF}, reflecting significant contribution of 2D superconducting fluctuation.

In zero magnetic field, the onset was defined as *T* where R_{sheet} deviates the linear fit (black dashed line) in the normal state. In finite magnetic fields, since the $R - T$ data show the localized behavior, T_{onset} was defined as *T* where R_{sheet} becomes flat as a function of *T*, namely $\mathrm{d}R/\mathrm{d}T$ = 0, which is indicated as black solid lines in Figs. 3.13a and b. T_{onset} are plotted by green diamonds in Figs. 3.16a and b for ZrNCl and MoS_2, respectively. Interestingly, T_{onset} traces almost the same curve as that of $B_{\mathrm{c}}(T)$. Because both $T_{\mathrm{onset}}(B)$ or $B_{\mathrm{c}}(T)$ curve is above the mean field curve, it is interpreted as the onset temperature (or magnetic field) of superconducting fluctuation. This is consistent with the idea that the boundary between the superconducting and insulating behavior corresponds to the crossing point of magnetoresistance in the localized system. Thus, the plots of B_{c} also describe the onset of superconducting fluctuations well. More importantly, the interval between $B_{\mathrm{c}}(T)$ and $B_{\mathrm{c2}}^{\mathrm{MF}}(T)$ increases with decreasing *T*, opposing to the case of the thermal fluctuation, for both samples. This behavior signifies the occurrence of the quantum fluctuation at low temperature and high magnetic fields.

The multi-crossing behavior at low temperatures in Figs. 3.14a and b shows stark contrast to the single crossing point observed in amorphous metallic films, e.g., MoGe [54] and Ta films [13], suggesting that the present system is not classified into the conventional universality class, which exhibits a direct SIT with a single crossing point. A possible scenario for the quantum fluctuation above $B_{\mathrm{c2}}^{\mathrm{MF}}(T)$ is the quantum Griffiths state, which was first theoretically proposed to understand the divergence of the dynamical exponent in QPTs in various lattice models with randomness [186, 187].

The diverging behavior of dynamical critical exponent is nowadays discussed within the context of the theoretical model based on the Griffiths singularity, where the rare ordered regions play a significant role for describing the quantum phase transition. The concept of the rare region was first pointed out by Griffiths in showing the nonanalytic behavior of magnetization in randomly diluted Ising ferromagnets. In such a system, due to the random quenched

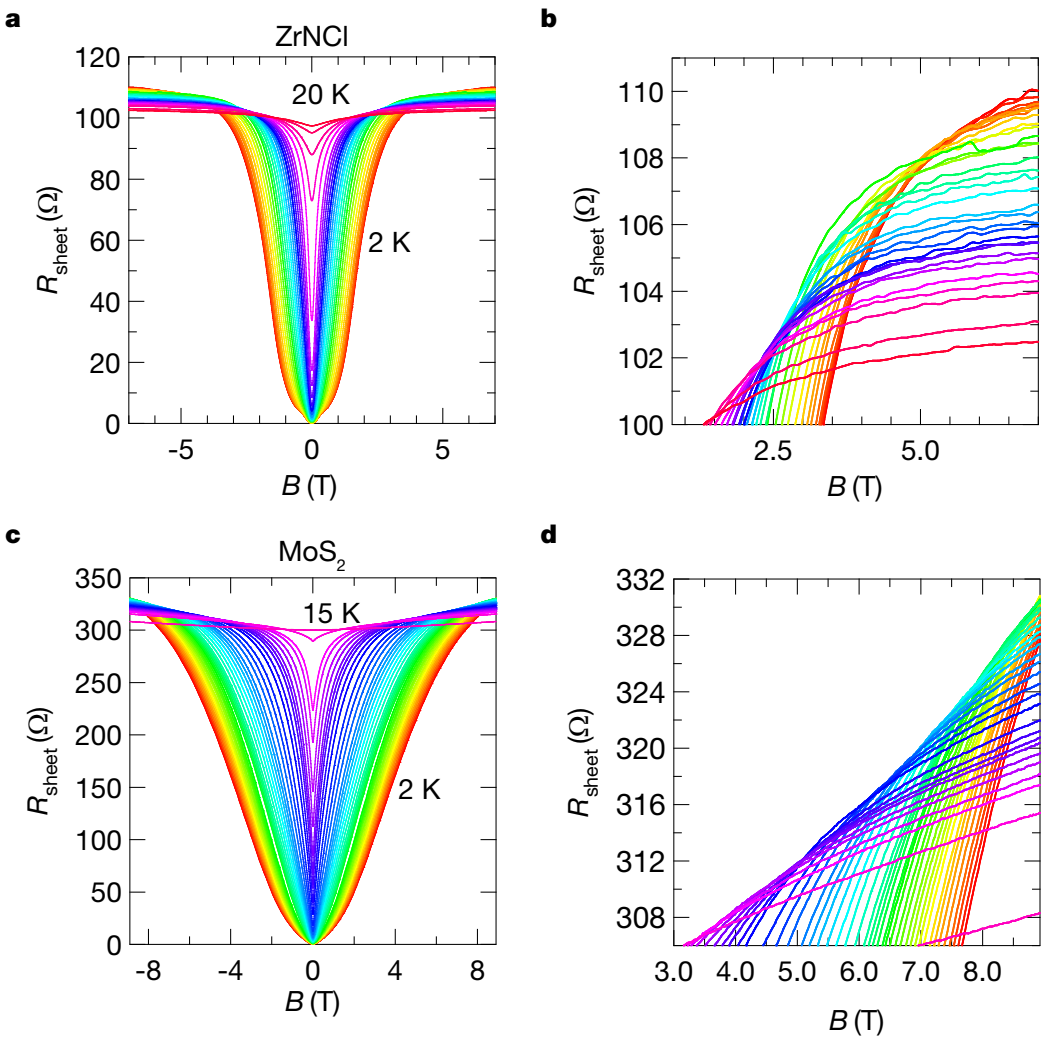

Figure 3.14 | Magnetoresistance and multiple critical points in a ZrNCl- and a MoS_2-EDLT. a, **c**, R_{sheet} as a function of $B_{c2}^{\perp}$ at various temperatures in the ZrNCl-EDLT and the MoS_2-EDLT. The measurement temperatures for the ZrNCl-EDLT range from 2 to 20 K (2, 2.3, 2.5, 2.7, 3, 3.3, 3.7 K, in 0.5 K steps from 4 to 13 K, in 1.0 K steps from 14 to 18 K, and 20 K). The measurement temperatures for the MoS_2-EDLT range from 2 K to 15 K (in 0.1 K steps from 2 to 4 K, in 0.2 K steps from 4.2 K to 5.4 K, 6, 6.3, 6.7, 7, 7.3, 7.5, 8, 8.3, 8.7, 9,1 10 and 15 K). **b**, **d**, A close-up view of around multiple crossing points of $R-B$ curves for the ZrNCl-EDLT (**b**) and MoS_2-EDLT (**d**).

disorder such as impurity and defects, the rare spatial regions that are locally in the magnetic persists in non-magnetic bulk. Although there are many theoretical works describing the Griffiths state and Griffiths singularity using lattice (Ising) systems [188−192], the related experimental works have been limited within 3*d*-ferromagnets, $Sr_{1-x}Ca_xRuO_3$ [193], $Ni_{1-x}V_x$ [194], and *f*-electron systems [195, 196].

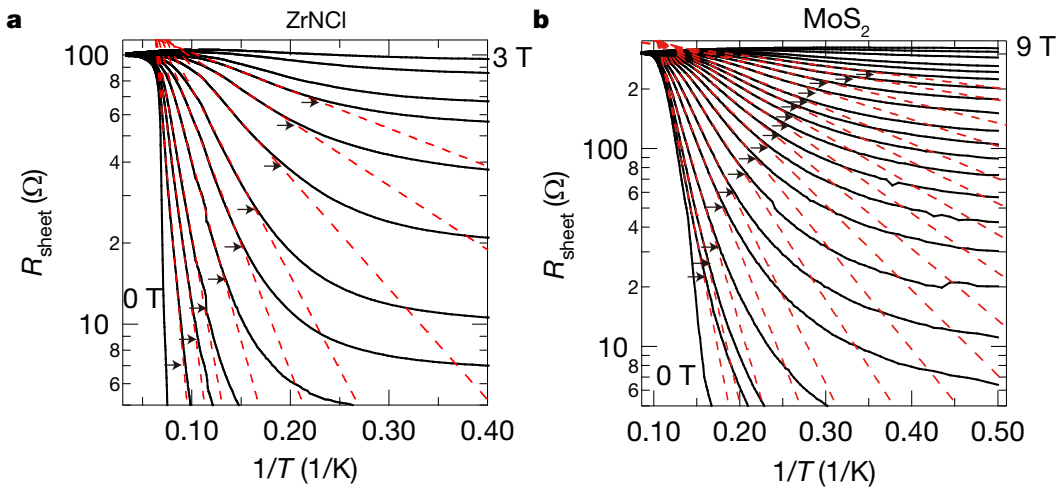

Figure 3.15 | Arrhenius plot of the sheet resistance of ion-gated ZrNCl and MoS_2. a, For ion-gated ZrNCl, the applied magnetic fields vary in 0.1 T steps from 0 to 0.3 T, in 0.2 T steps from 0.5 to 0.9 T, in 0.3 T steps from 1.2 to 1.8 T and in 0.5 T steps from 2.0 to 3.0 T. **b**, For ion-gated MoS_2, they vary in 0.1 T steps from 0 to 0.2 T, in 0.2 T steps from 0.4 to 0.6 T, in 0.3 T steps from 0.9 to 3.0 T in 0.5 T steps from 4 to 7 T and in 1 T steps from 8 to 9 T. The red dashed lines show the activated behavior based on the 2D collective creep model. The crossover temperature T_{cross} is defined as the temperature at the deviation point from the red dashed lines, shown by arrows.

The possibility of the Griffiths singularity in superconducting systems has been discussed in ultrathin disordered nanowires [197], but there is no example in 2D systems. Very recently, the quantum Griffiths singularity is experimentally observed in two-kinds of 2D superconductors: molecular-epitaxy-grown Ga trilayer [37], $NbSe_2$ monolayer [198] and $LaAlO_3/SrTiO_3$ (110) polarized-interface [199]. In these two systems, multiple critical points were observed as is reported in our study. To analyze the experimental data, they used the finite size scaling (FSS) analysis for different temperature regimes, and they found the dynamical critical exponent shows a power-law form. This anomalous scaling behavior, as is observed in the present study, is suggested in the quantum random transverse field Ising model [190, 191], which shows the activated scaling with continuously varying dynamical critical exponent z, when approaching the infinite-randomness QCP. Such critical behavior originates from the special condition of disorder in the statistical treatment, where the average strength of disorder (magnitude of inhomogeneity) increases without limit under coarse graining, that is theoret-

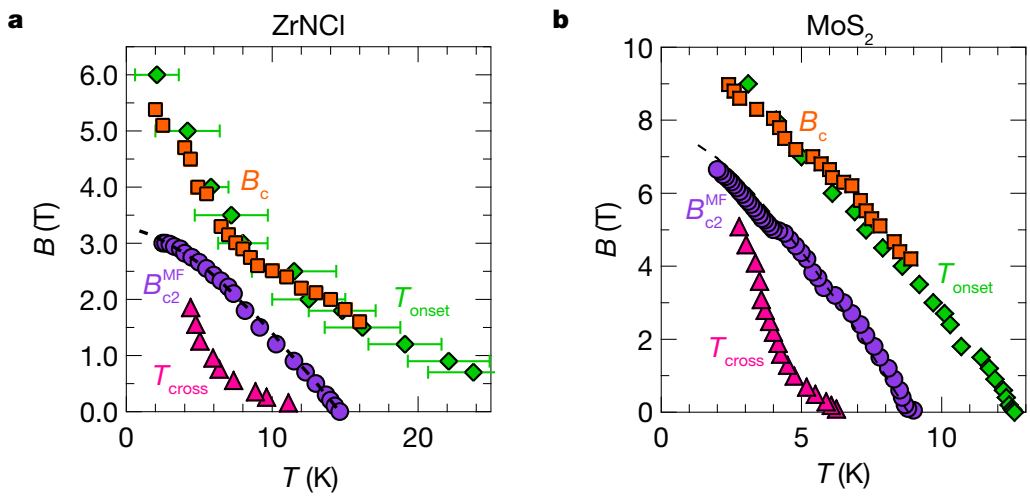

Figure 3.16 | $B - T$ phase diagram of 2D superconducting ZrNCl and MoS_2. The magnetic field-temperature phase diagram of the ZrNCl- (**a**) and MoS_2-EDLT (**b**). Orange squares show the crossing points B_2 of $R - B$ curves in Figs. 3.14a and b at neighboring temperatures. Pink circles show the mean field upper critical field B_{c2}^{MF} derived from the UD scaling. Green diamonds show the onset of superconducting fluctuation T_{onset}. Error bars of green diamonds represent the ambiguity of T_{onset} defined by $dR_{sheet}/dT = 0$ due to the experimental resolution (see Fig. 3.13). Blue triangles show the crossover temperature T_{cross} from the thermal creep regime to the quantum creep regime defined as the deviation points from the linear dependence of R_{sheet} in the Arrhenius plot. Dashed curve shows the fitting of $B_{c2}^{MF}(T)$ by the WHH theory [185].

ically equivalent to $d\nu < 2$ (, which means that Harris criterion is violated [189]) with the dimension of system (d)and the correlation length exponent (ν). Therefore, the Griffith state with the diverging z should satisfy this condition. Indeed, ν is theoretically predicted as 0.5 for the superconductor-metal transition in a clean 2D superconducting system [200], the Harris criterion is violated with $d\nu$ = 1. In this case, the introduction of finite quenched disorder can lead to the infinite-randomness QCP, observed as the quantum Griffith singularity. Following this scenario, the product of the critical exponents $z\nu$ is expressed by the activated scaling law [197, 201−203]:

$$z\nu \approx C|B - B_c^*|^{v\Psi} \tag{3.18}$$

with the constant C and the 2D infinite-randomness critical exponents of $v \approx 1.2$ and $\Psi \approx 0.5$ [204, 205]. Here, B_c^* is infinite randomness QCP. This formula is consistent with the experimental data of Ga [37], $NbSe_2$ thin films [198], $LaAlO_3/SrTiO_3$ [199] and our systems. To

investigate the multiple-crossing behavior of magnetoresistance shown in Figs. 3.14a and b, and test the possible application of quantum Griffiths singularity, we performed the FSS law of magnetoresistance for QPT expressed as,

$$R(B,T) = R_{\mathrm{c}} f((B - B_{\mathrm{c}})/(T/T_0)^{1/z\nu}) \tag{3.19}$$

in various temperature regimes around the crossing points based on the data shown in Figs. 3.14a and b. Here, B_{c}, R_{c}, T_0, $f(x)$ are the critical magnetic field, the asymptotic critical sheet resistance (, both of which are defined as the values at the crossing points), the lowest temperature used in the scaling of $R - B$ curves, and the scaling function with $f(0) = 1$, respectively. To investigate the evolution of the effective critical exponents zν with the decrease (or increase) in *T* (or *B*), five representative crossing points were selected both for ZrNCl and MoS_2, and then the FSS analysis in the narrow temperature regimes around these crossing points were performed.

During the scaling, we derived $z\nu$ by assuming that the functional forms of $f(x)$ both for $x > 0$ and $x < 0$ unchanged. In Fig. 3.17 and 3.18, the left graphs show R_{sheet} as a function of *B* close to the selected crossing points. The right graphs shows normalized R_{sheet} as a function of $|B - B_{\mathrm{c}}|(T/T_0)^{-1/z\nu}$.

The obtained values of $z\nu$ in ZrNCl and MoS_2 are plotted as a function of *B* as shown in Figs. 3.19a and b, respectively. $z\nu$ is not constant as observed in conventional films and varies as a function of *B* (it T) in both systems, and seems to diverge toward a certain critical field following the relation of $z\nu \approx C|B - B_{\mathrm{c}}^{*}|^{-0.6}$, which is consistent with eq. 3.18. This diverging behavior of the critical exponent with multiple crossing points is in stark contrast to the conventional dirty metallic films, which shows temperature-independent constant critical exponents with a single critical field [33].Such a divergent critical exponent consistent with the Griffiths singularity indicates that rare ordered regions are existing even above $B_{\mathrm{c2}}^{\mathrm{MF}}$ with a rather long time-scale and finite length scale due to the quantum fluctuation. Such rare regions are interpreted as superconducting puddles in this particular case.

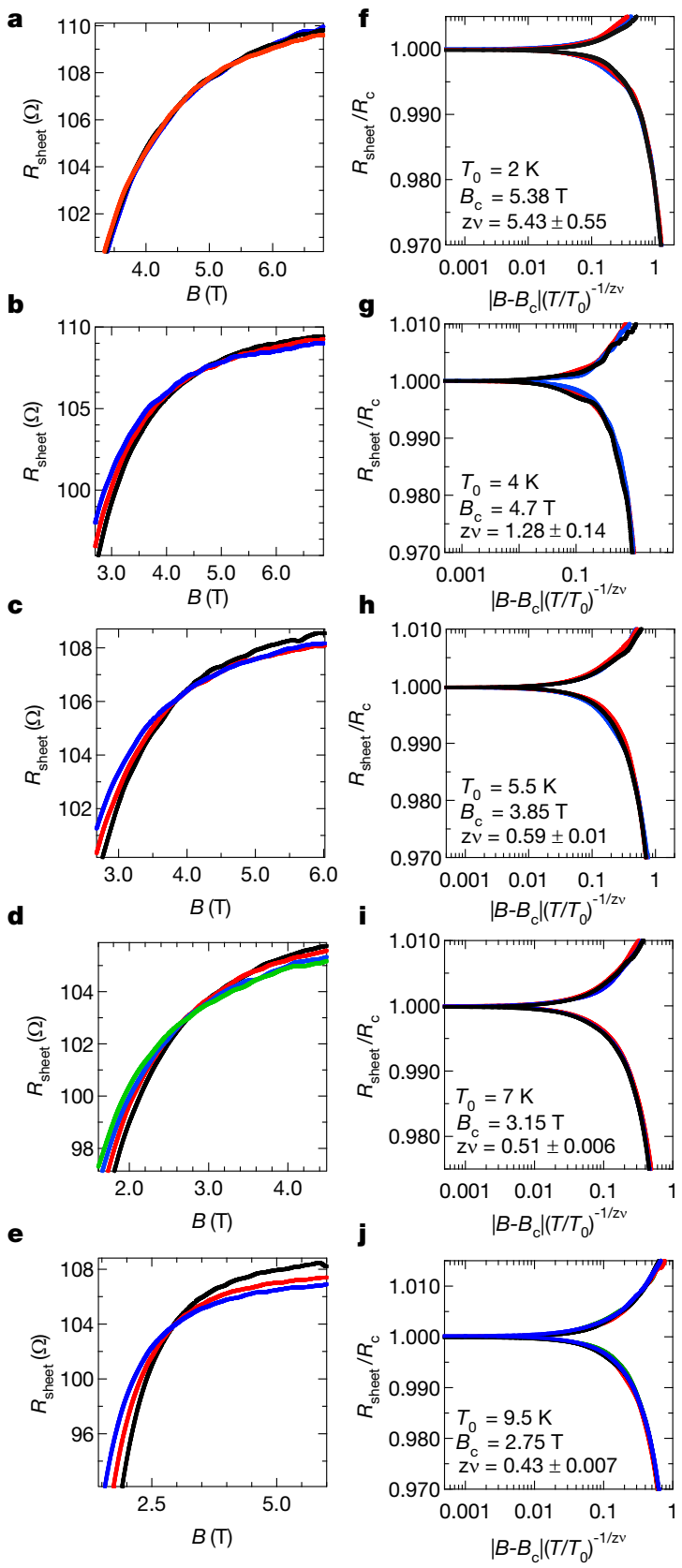

Figure 3.17 | FSS analysis at different temperatures for ion-gated ZrNCl. a–e, R_{sheet} as a function of B close to the transition boundary at different temperatures. **f–j**, Normalized R_{sheet} as a function of $|B - B_{\mathrm{c}}|(T/T_0)^{-1/z\nu}$. Here, the B_{c} determined the crossing points of $R_{\mathrm{sheet}}(B)$ curves, and T_0 is the lowest temperature in each set of the $R - B$ curves.

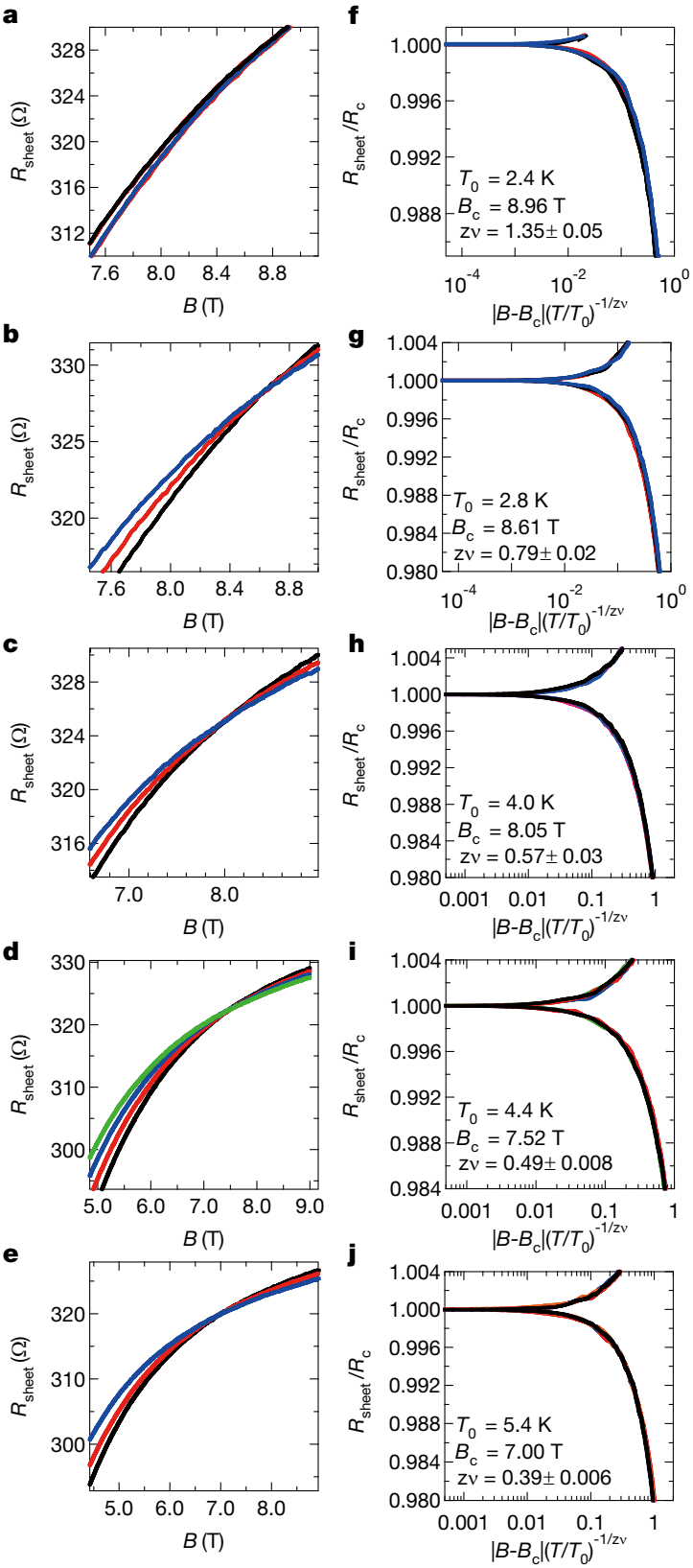

Figure 3.18 | FSS analysis at different temperatures for ion-gated MoS_2. a–e, R_{sheet} as a function of B close to the transition boundary at different temperatures. **f–j**, Normalized R_{sheet} as a function of $|B - B_{\mathrm{c}}|(T/T_0)^{-1/z\nu}$. Here, the B_{c} determined the crossing points of $R_{\mathrm{sheet}}(B)$ curves, and T_0 is the lowest temperature in each set of the $R - B$ curves.

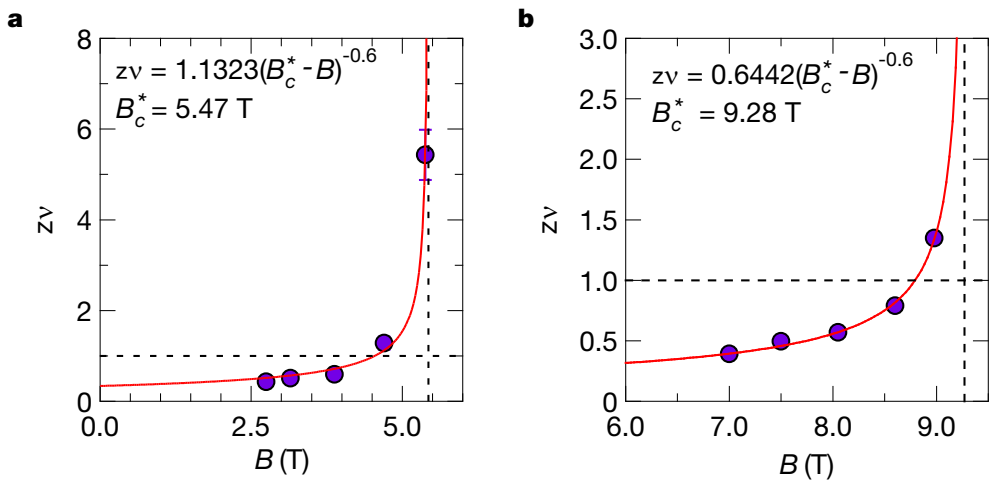

Figure 3.19 | Divergent behavior of critical exponent in ion-gated ZrNCl and MoS_2. a, **b**, Critical exponent $z\nu$ as a function of B for ZrNCl- (**a**) and MoS_2-EDLT (**b**). The $z\nu$ values in each temperature regime is calculated by the FSS analysis. Error bars represent the width of zν value with which the FSS scaling behavior is established in the whole range of B for the data of Fig. 3.17. With increasing magnetic field and decreasing temperature, the value of $z\nu$ increases and finally shows divergent behavior with no signature of saturation. The red curve shows a fitting based on $z\nu \approx C(B - B_c^*)^{-0.6}$ (activated scaling law). Two black dotted lines in each graph mean the constant values of $z\nu$ = 1 and B_c^* = 5.43 T for **a**, and $z\nu$ =1 and B_c^* = 9.27 T for **b**, respectively.

3.5 Discussion

Based on the experimental data of the ZrNCl-EDLT, we propose a comprehensive phase diagram of highly crystalline 2D superconductors in Fig. 3.20, which is characterized by two crossover curves, $B_c(T)$ (orange squares) and $T_{\rm cross}(B)$ (blue triangles), and a mean field curve (black solid curve in Fig. 3.20). The former corresponds to the onset of superconducting fluctuation terminating at the QCP (B_c^*) characterized by the quantum Griffiths singularity at a high magnetic field at T = 0 K. The latter $T_{\rm cross}(B)$ represents the crossover boundary between the thermal and quantum vortex creep region derived from the Arrhenius plot analysis of $R_{\rm sheet}(T)$ data in Fig. 3.12a. Because $B_c(T)$ is extrapolated to the onset temperature $T_{\rm onset}$ of the AL type fluctuation [44] at $B = 0$, the region above $T_c^{\rm MF}(B)$ at low magnetic fields is dominated by thermal fluctuation of the order parameter amplitude. This state crossovers to the thermal creep (thermal phase fluctuation) below $T_c^{\rm MF}(B)$ and then to the quantum creep (quantum phase fluctuation) region below $T_{\rm cross}(B)$ with decreasing temperature. At high magnetic fields, on the

other hand, thermal fluctuation region shrinks because of the decrease of $T_{\mathrm{c}}^{\mathrm{MF}}(B)$. However, with further decreasing temperature, $B_{\mathrm{c}}(T)$ shows an upturn, which is a signature of the emergence of quantum fluctuation. The $T_{\mathrm{cross}}(B)$ curve seems smoothly connected to the upturn of $B_{\mathrm{c}}(T)$ at low temperatures. This feature suggests that the quantum fluctuations in highly crystalline 2D superconductors govern the evolution of the ground state, stemming from a very low magnetic field with quantum metallic state to the quantum Griffiths state, followed by the QPT above $B_{\mathrm{c2}}^{\mathrm{MF}}(0)$ with quantum Griffiths singularity. Such upturn behavior as observed in ZrNCl-EDLT was not observed in the MoS_2-EDLT. The absence of upturn behavior is possibly because of lower T_{c} and thus narrower measurement range in the MoS_2-EDLT compared with the that in ZrNCl-EDLT as discussed in the case of $LaAlO_3/SrTiO_3$ [199]. Nevertheless, the signature of divergent behavior of zν observed in the MoS_2-EDLT suggests the existence of the quantum Griffiths state.

Figure 3.20 suggests that the quantum fluctuations governs the phase evolution particularly at low temperatures. The crossover from the quantum metallic state to the Griffiths state is rationalized as follows. Although the ground state predicted in disorder-free 2D superconductors is the vortex lattice phase [206], which is similar to the 3D disorder-free type-II superconductors [207, 208], the long-range order of a vortex lattice easily becomes unstable because of the fluctuations caused by disorder in the absence of the longitudinal elasticity of vortices. This leads to the imperfect vortex lattice state containing many dislocations even in relatively clean system. At low magnetic fields, the plastic motion of dislocations based on the weak pinning and weak elasticity occurs by the thermal [173] and quantum fluctuation in high and sufficiently low temperatures, respectively, as shown in Fig. 3.20. In this situation, the sample consists of the superconducting puddles with short-range ordered vortices and the dissipation regime surrounding them at low temperatures. With increasing magnetic field above $B_{\mathrm{c2}}^{\mathrm{MF}}$, the dissipation region evolves into the normal state, but it is possible that puddle-like superconducting islands remain at very low temperature because of the effect of the quantum

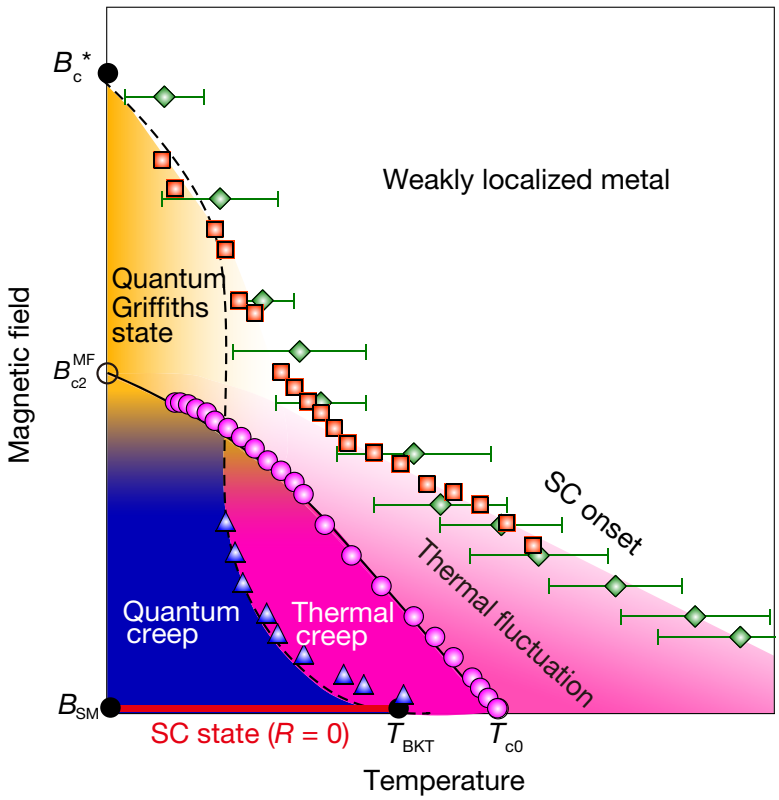

Figure 3.20 | $B - T$ phase diagram of highly crystalline 2D superconductors. The plotted data based on Fig. 3.16a. T_{c0} is the transition temperature determined by the thermal fluctuation theories (AL and MT model), and true superconducting state (zero resistance state) is realized below the BKT transition temperature (T_{BKT}). Blue triangles show the crossover temperature T_{cross} between the thermal creep regime and the quantum creep regime. Orange squares, green diamonds and pink circles show the crossing points B_{c} of $R - B$ curves in Figs. 3.14a and b at neighboring temperatures, the superconducting onset T_{onset} and the $B_{\mathrm{c2}}^{\mathrm{MF}}$ calculated by UD scaling, respectively. Under a relatively low B, finite resistance state occurs due to the thermal creep (pink region) and quantum creep (blue region) in the relatively high and low temperature region, respectively. B_{SM} is the hypothetical transition magnetic field from the zero-resistance state to the quantum metal (vortex liquid). The system eventually exhibits the quantum Griffiths state (orange region) up to the infinite randomness QCP B_{c}^*. The black solid and dashed curves show the $B_{\mathrm{c2}}^{\mathrm{MF}}(T)$ based WHH model and, crossover curve between thermal fluctuation region and quantum fluctuation region, respectively.

fluctuation stabilized by quenched disorder, resulting in the quantum Griffiths state with rare superconducting regions. Thus, the quantum creep region (quantum metallic state) is naturally connected to the quantum Griffiths state at low temperature. This situation can be a consequence of strong quantum fluctuation in the 2D superconductor with the very weak but finite pinning effect, leading to a standout effect of randomness.

The difference of quantum Griffiths state and quantum metallic state is considered to

originate from two kinds of fluctuation: the amplitude and phase fluctuation, using the analogy to the case of the thermal fluctuations. In other words, the quantum Griffiths state and quantum metallic state correspond to quantum fluctuations of amplitude and phase of order parameter, respectively. In the quantum metallic state, the individual motion of vortices is suppressed by the elasticity of the vortices (in other words, the vortices locally form lattices), and vortex creep occurs at the connecting region of local lattices, where the elastic energy of vortices is small. Therefore, the phase fluctuation locally appears in the quantum metallic state. As the magnetic field increases, the vortex-lattice mismatch regions, where the quantum creep frequently occurs, widen and eventually become normal states. However, there remain the locally ordered regions due to the pinning by quenched disorder, which form the puddle-like regions with nonzero order parameter. This situation may evolve into to a quantum Griffiths state with spatial amplitude fluctuation of order parameter.

It is noted that the quantum Griffiths state, which shows activated critical behavior with divergent critical exponent, is fundamentally different from the phase separation or originally spatial inhomogeneity of the superconducting state as discussed in $LaTiO_3/SrTiO_3$, which shows multiple constant critical exponents [35, 209]. In those inhomogeneous systems, the critical exponent shows temperature-independent constant value, as frequently observed in conventional systems. More importantly, the channel area possesses atomically flat surface (Fig. 3.10), and accumulation of carrier is homogeneous as explained in the section of quantum metallic state. Thus, the divergent behavior of critical exponent observed in the previous section is one of the strong evidence of the quantum Griffiths state.

Also, we note that in the previous studies, amorphous InO_x exhibited temperature dependent multiple crossing points in magnetoresistance isotherms [11, 159, 210, 211], which is similar to the Griffiths phenomenon. However, in some reports the critical divergent behavior of the transport critical exponents is different from that discussed above: crossing magnetic fields decreases with decreasing temperature [11, 211], while it increases in the other way in

other reports [11, 211]. These phenomena were also discussed in terms of the different view from the Griffiths effect [212], but still remains yet to be understood.

In the early works on amorphous 2D superconductors such as MoGe [54] and Ta [13], the quantum Griffiths singularity was not observed even at ultra-low temperatures. One possible reason for the absence of quantum Griffiths singularity, in addition to the measurement temperature range, is the large amount of homogeneously distributed quenched disorder, in the conventional 2D superconductors, which give a rather homogeneous effect. On the other hand, in highly crystalline 2D systems, the ordered regions and weakly disordered regions can coexist, which causes rare regions under sufficiently large magnetic fields, and thus leads to quantum Griffiths singularity. Therefore, the quantum Griffiths state is a signature of high crystallinity of the system with random disorder. In the recent study of mechanically exfoliated $NbSe_2$[38] bilayer, neither the single crossing nor the multiple crossing behavior has been observed, leading to the absence of the quantum Griffiths state. This is possibly due to the further reduction of the quenched disorder in 2D single crystalline $NbSe_2$. In this case, the localization effect at low temperatures might be too small to observe the quantum Griffiths state.

In summary, we established the comprehensive quantum phase diagram including superconducting fluctuation regime in ion-gated 2D crystalline superconductors. This class of superconductors commonly exhibit the wide range of quantum metallic state and quantum Griffiths state as a ground state, which transfers into the weakly localized normal metal through a QPT showing the quantum Griffiths singularity. It is actually surprising that the quenched disorder effect due to quantum fluctuation, namely quantum Griffiths effect can be observed in ion-gated 2D crystalline superconductors, not in highly disordered 2D superconductors. Furthermore, our results indicate that the coexistence of the puddle-like superconducting regions and the dissipation region, occurring owing to the combined effect of the strong quantum fluctuation and extremely weak pinning or random disorder, is universal nature above B_{c2}^{MF} in the

low temperatures in highly crystalline 2D superconductors.

4

2D superconductivity protected by spin-valley locking in ion-gated MoS_2

4.1 Introduction

In 2D superconductors, the upper critical field determined by the orbital limit becomes infinitely large, and instead the Pauli limit can be dominant in the in-plane magnetic field geometry. In early stage works, the parallel upper critical field $B_{\mathrm{c2}}^{\parallel}$ larger than the usual Pauli limit $B_{\mathrm{P}}^{\mathrm{BCS}} \sim 1.86T_{\mathrm{c}}$ based on the BCS theory for weak-coupling superconductors had frequently been attributed to the effect of strong spin-orbit scattering causing the spin randomization in high-Z elements (a-Bi or a-Pb) or layered materials with large atomic SOI [59, 60], because these metallic thin films superconductors were dirty systems with very short mean free length compared to coherence lengths in most cases. However, once the system becomes crystalline with less disorder and then enter the clean regime, the spin-orbit scattering effect becomes weak, and instead the effect of spin-momentum locking based on SOI can much contribute to enhancement of the upper critical field, especially in noncentrosymmetric superconductors with large spin orbit coupling. However, previous experimental works related to large upper critical field enhanced by spin-momentum locking have been limited to the system

with Rashba-type SOI as is represented mainly by heavy fermions [92, 213−215].

Superconducting atomic layers based on TMDs are highly crystalline 2D systems with large SOI. In the monolayer limit with threefold symmetry, the in-plane mirror symmetry is broken, which causes a special type of spin-orbit interaction producing out-of-plane spin polarization together with effective Zeeman fields, namely the Zeeman-type spin polarization, leading to the spin split band at the K valleys [216, 217] at zero magnetic field. This Zeeman-type spin splitting is in stark contrast to the Rashba-type spin splitting with the helical spin texture, and is the intrinsic nature of TMDs monolayer that originates from its D_{3h} crystal symmetry. Such a spin splitting is not observed in bulk $2H$-polytype TMDs with D_{6h}^4 symmetry [218] showing the global inversion symmetry. In the case of $2H$-MoS_2, which is the most famous example in TMD family, this Zeeman-type spin splitting reaches 3 and 148 meV at the bottom of conduction band and the top of the valence band, respectively, both of which are located at the K-points, the corner of the hexagonal first Brillouin zone. In addition, in the in-plane magnetic field geometry, 2D superconducting MoS_2 can be an ideal platform to investigate the relation between superconductivity and intrinsic Zeeman-type spin-splitting.

4.2 Two-dimensionality and huge anisotropy in 2D superconducting MoS_2

In this chapter, I describe the anomalously enhanced upper critical field in electric-filed-induced superconductivity in $2H$-MoS_2 single crystals [219]. In order to extract anomalous features of electric-field-induced superconductivity at the highly crystalline multilayer MoS_2 surface, we first fabricated an EDLT structure with a 20-nm-thick flake prepared by mechanical exfoliation (Device L1), and then performed magneto-transport measurements. The device exhibited a superconducting transition at V_G = 6.5 V and $n_{2D} = 1.5 \times 10^{14}$ cm^{-2} at 15 K.

The T_c of this device was 9.7 K, as defined at the mid-point of the transition with R_{sheet} being 50% of the normal state sheet resistance at 15 K. This carrier density is slightly larger

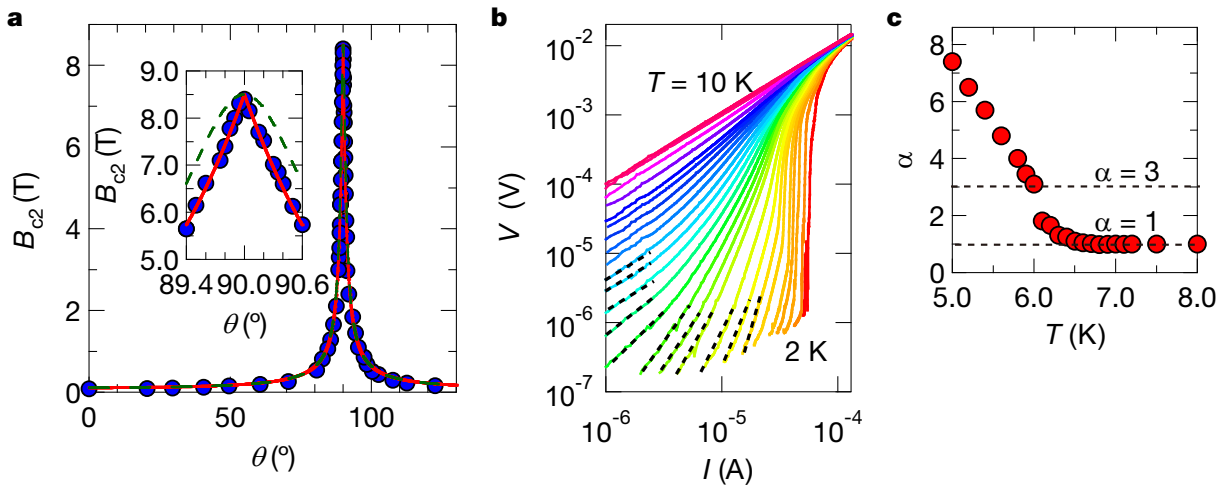

Figure 4.1 | Two-dimensionl superconductivity in ion-gated MoS_2. **a**, Angular dependence of the upper critical field B_{c2} at 9.6 K (θ is the angle between a magnetic field and the perpendicular direction to the surface of MoS_2). The inset displays a magnified view of the region around $\theta = 90$ degree. The red solid line and the green dashed line correspond to the theoretical representation of B_{c2}, the 2D Tinkham's formula and the 3D anisotropic mass model (3D-GL), respectively. **b**, The $I - V$ characteristic at different temperatures close to T_c, plotted on a logarithmic scale. The black dashed line shows the slope of $I - V$ relationship at small current. **c**, Temperature dependence of α from fitting the power law dependence of $V \propto I^{\alpha}$. T_{BKT} = 5.9 K is obtained for α =3

than the optimum value in the dome-shaped phase diagram [30]. As observed in ZrNCl-EDLT, the MoS_2-EDLT also shows typical 2D behavior in terms of angular dependence of upper critical field and BKT-transition like $I-V$ characteristic (Fig. 4.1). Here, we used another device (Device L2) to investigate $I-V$ characteristics.

Figure 4.2 displays a zoom-up of the resistive transition in the low temperature region under the application of perpendicular and parallel magnetic fields from 0 to 9 T, respectively. The superconducting state is completely quenched at 9 T for the perpendicular magnetic fields (Fig. 4.2a), whereas it remains almost unchanged in the in-plane magnetic field geometry (Fig. 4.2b). This behavior indicates a substantially large anisotropy in the superconductivity. As is observed in ZrNCl-EDLTs in chapter 3, T dependence of B_{c2} for both the out-of-plane and in-plane magnetic fields are well fitted by the phenomenological GL model, $B_{c2}^{\perp} = \frac{\Phi_0}{2\pi\xi_{GL}(0)^2}\left(1 - \frac{T}{T_c}\right)$ and $B_{c2}^{\parallel} = \frac{\Phi_0\sqrt{12}}{2\pi\xi_{GL}(0)d_{SC}}\sqrt{1 - \frac{T}{T_c}}$, where Φ_0, $\xi_{GL}(\theta)$, and d_{SC} denote a flux quantum, the in-plane GL coherence length at T = 0 K, and the effective thickness of

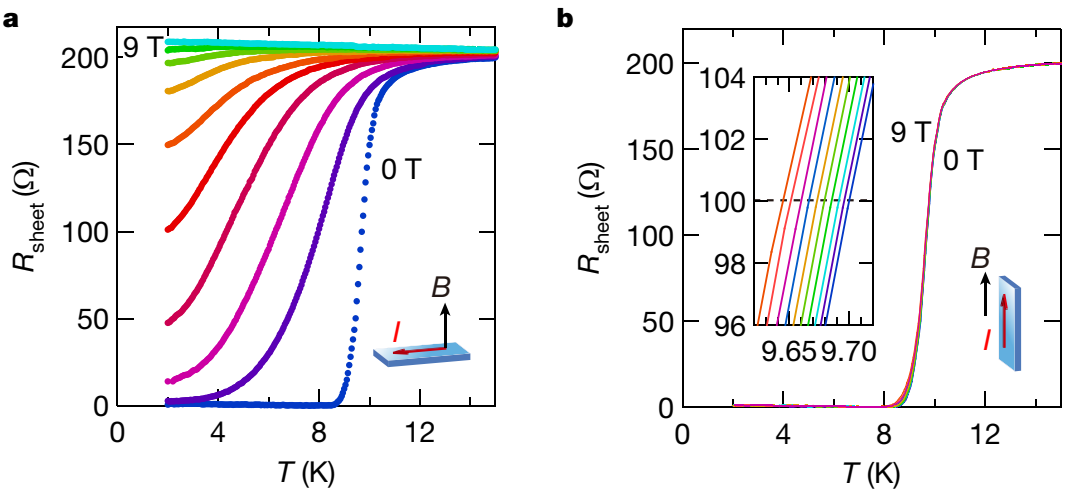

Figure 4.2 | Sheet resistance of a MoS_2-EDLT as a function of out-of-plane and in-plane magnetic fields at V_G = 6.5 V. a, b, R_{sheet} of a MoS_2-EDLT as a function of temperature at V_G = 6.5 V, for (**b**) perpendicular magnetic fields, and (**c**) parallel magnetic fields, $B_{c2}^{\parallel}$, varying in 1 T steps from 0 to 9 T, respectively. The inset shows a close-up of the resistive transition near the mid-point of the normal state sheet resistance (black dashed line).

superconductivity, respectively. We find $\xi_{GL}(\theta)$ = 8.0 nm and d_{SC} = 1.5 nm. It is noted that the extremely sharp rise of $B_{c2}^{\parallel}$ near T_c shows a marked contrast to that in the conventional bulk layered superconductors, demonstrating that the present system is extremely 2D in nature. In fact, $B_{c2}^{\parallel}$ can seemingly go far beyond the Pauli limit, B_P^{BCS}, for weak coupling BCS superconductors, $B_P^{BCS} = 1.86T_c$ = 18 T, where k_B and θ are the Boltzmann constant and the superconducting gap at T = 0 K, based on the BCS theory, respectively.

4.3 Observation of the anomalously enhanced upper critical field

To investigate at much lower temperatures, we measured the magnetoresistance of another MoS_2-EDLT (Device H1) applying pulsed magnetic fields up to 55 T. We performed all the magnetoresistance measurements in a four-probe configuration using a 55 T magnet with the duration time of 36 ms and a rotator probe at the International MegaGauss Science Laboratory (Fig. 4.3). The voltage signals were recorded on National Instruments PXIe-6124 digitizers using a homemade numerical lock-in technique at a frequency of f = 80 kHz. The sensitivity

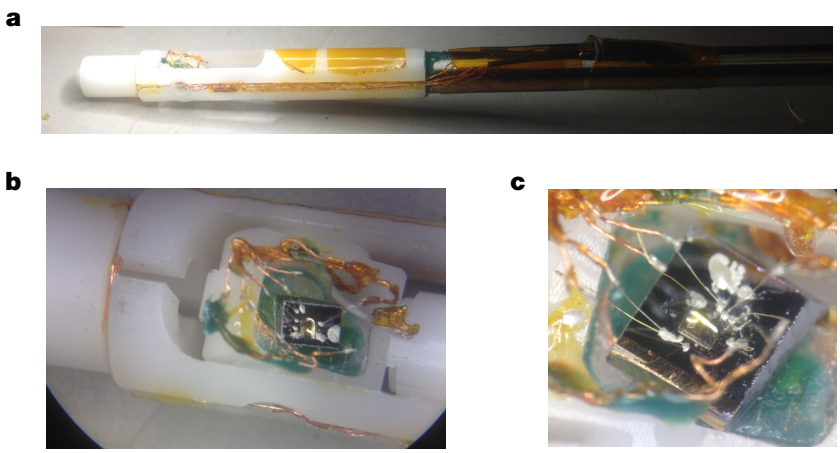

Figure 4.3 | Pictures of the probe for high magnetic field measurements. a, Part of a sample probe near the sample stage. **b**, Sample stage and samples on a rotator. **c**, Close-up of the sample.

of the angle measurement is within $\sim$ 0.1 degree in our rotator probe. To align the field direction, we performed the B_{c2} measurement as a function of angle in pulsed magnetic fields. The misalignments for the in-plane magnetic fields and out-of-plane magnetic fields are estimated to be less than $\sim$ 0.02 and $\sim$ 1.0 degree, respectively. We observed clear voltage signals of the magnetoresistance from the MoS_2-EDLT, followed by pulsed magnetic fields. Figure 4.4 shows a typical time dependent voltage signal under a pulsed magnetic field. The magnetoresistance data were obtained during the down sweep of a pulsed magnetic field. All these magnetoresistance measurements have been performed out under the condition that the source-drain current, I_{DS}, was less than 10 μA, in which we confirmed that the behavior of the temperature-dependent resistance and magnetoresistance below 8 K were almost unchanged. Some eddy current heating was observed in measurements between 4 and 8 K. Below 4 K, the MoS_2-EDLT was immersed in liquid helium, which prevents heating in the device.

T_{c} of the present device was defined by the temperature where R_{sheet} reached 75% of the normal state sheet resistance, indicating a superconducting signature, although this MoS_2-EDLT used for the high magnetic field measurements ($n_{\mathrm{2D}} = 8.5 \times 10^{13}$ cm^{-2} at V_{G} = 5.5 V and T = 15 K) did not exhibit zero resistance. Figure 4.5a and b displays the magnetoresistance of the MoS_2-EDLT for out-of-plane and in-plane magnetic fields, respectively, at several

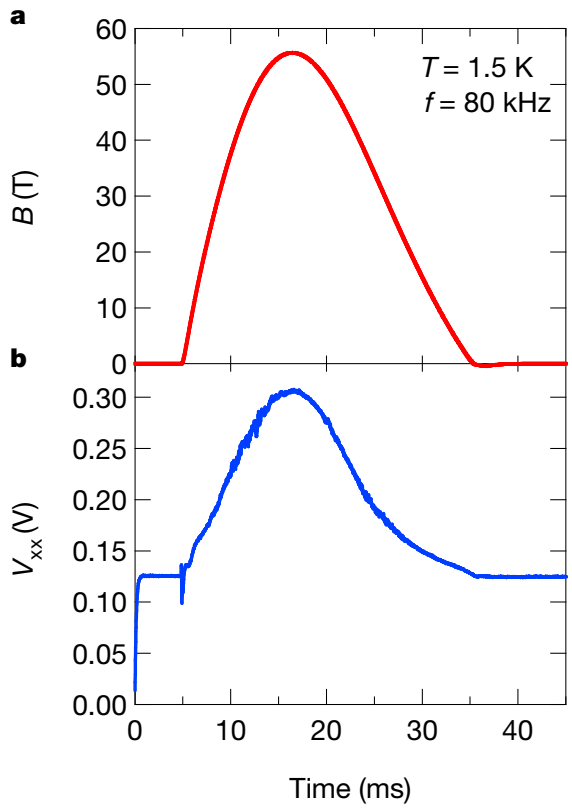

Figure 4.4 | Time-dependent magnetic field and voltage probe signal in a MoS_2-EDLT at V_G = 5.5 V. a, **b**, A pulsed magnetic field (**a**) and the voltage probe signal (**b**) as a function of time, respectively. This measurement was made at T = 1.5 K with an AC measurement set up with a frequency of f = 80 kHz.

temperatures between 1.5 and 8.0 K. In the out-of-plane magnetic field geometry, the superconducting state is completely destroyed by the application of more than 5 T magnetic fields as is observed in lab-level measurement. On the other hand, for the in-plane magnetic fields, the superconductivity is not completely suppressed nor does it revert to the normal state even by applying a 55 T magnetic field at 1.5 K (Fig. 4.5b). We summarize both $B_{c2}^{\perp}(T)$ and $B_{c2}^{\parallel}(T)$ in Fig. 4.6. We note that $B_{c2}^{\parallel}(T)$ increases with decreasing temperature and eventually saturates approximately 52 T at 1.5 K, which is more than four times larger than B_{P}^{BCS} = 12 T. Because the orbital limit is supposed to be large owing to the confined geometry by the EDLT, the saturating behavior of $B_{c2}^{\parallel}(T)$ at low temperatures is suggestive of the Pauli limit, as seen in the Pauli limited superconductor. Similar experimental results have been observed in ion-gated MoS_2 [220] and mechanically-exfoliated $NbSe_2$ [221].

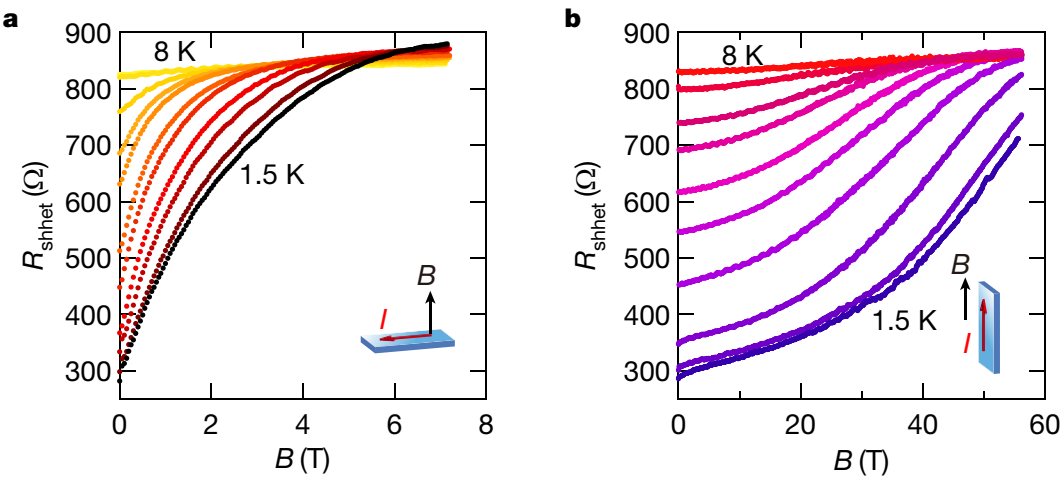

Figure 4.5 | High magnetic field measurement on ion-gated MoS_2. a, R_{sheet} of a MoS_2-EDLT as a function of B up to 55 T at V_{G} = 5.5 V, for the out-of-plane direction at 1.5, 2.9, 3.9, 4.4, 5.1, 5.6, 6, 6.5, 6.8, 7.3 and 8.0 K, and **b**, for in-plane direction at 1.5, 2.8, 4.2, 5.3, 6, 6.4, 6.5, 6.8, 7.1, 7.6 and 8.0 K.

The enhancement of B_{c2} in dirty-limit superconductors with strong spin orbit interaction has been discussed in terms of the spin-orbit scattering caused by disorder. This is supposed to cause randomization of electron spins, and thus result in suppression of the effect of spin paramagnetism [185, 222, 223]. To evaluate the contribution of this effect, we used the microscopic Klemm-Luther-Beasely (KLB) theory [223], which is applicable to dirty-limit layered superconductors with strong spin orbit interaction ($l << \xi_{\mathrm{Pippard}}$ and $\tau << \tau_{\mathrm{SO}}$, where $l, \xi_{\mathrm{Pippard}}, \tau$ and τ_{SO} are the mean free length, the Pippard coherence length, the total scattering time and the spin orbit scattering time, respectively). Then, we fitted B_{c2} values of three devices (Device H1, H2, L1; those devices showed different T_{c} at different carrier densities (Fig. 4.7a and b) by using this microscopic KLB theory, and then estimated the values of τ_{SO} as fitting parameters (Table 4.1). In this theory, B_{c2} arising from a monolayer satisfies the following equations,

$$\ln\left(\frac{T}{T_{\mathrm{c}}}\right) + \Psi\left(\frac{1}{2} + \frac{3\tau_{\mathrm{SO}}(B_{\mathrm{c2}}^{\parallel})^2}{4\pi T}\right) - \Psi\left(\frac{1}{2}\right) = 0 \tag{4.1}$$

where $\psi(x), \mu_B$ and T_{c} are digamma function, the Bohr magnetism and T_{c}, respectively. Although all $B_{\mathrm{c2}}^{\parallel}$ values seem to be quite well fitted by the KLB theory, τ estimated by the

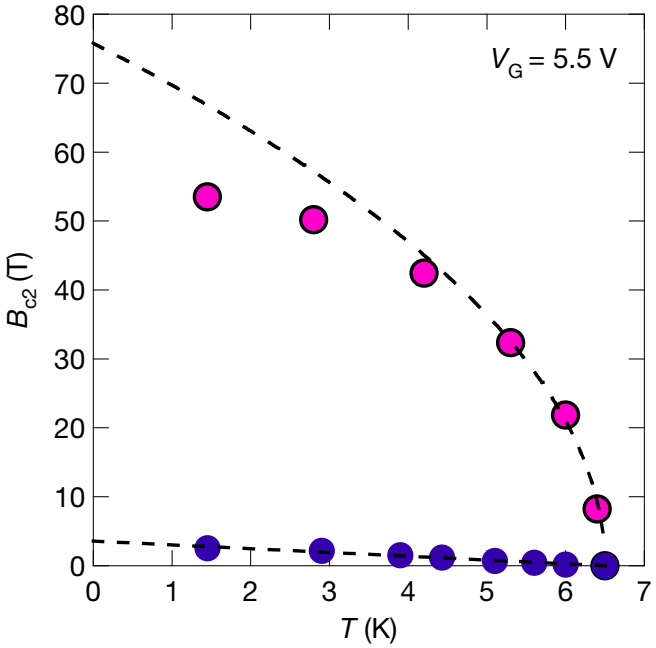

Figure 4.6 | In-plane and out-of-plane upper critical fields as a function of temperature at V_G = 5.5 V. B_{c2} is defined as the magnetic field where R_{sheet} reached 75% of the normal state sheet resistance. The black dashed line and curve show the 2D-GL model for out-of-plane and in-plane magnetic field geometry, respectively. The value of B_{c2} increases with decreasing temperature, following the 2D-GL model near T_c, but deviates from the model at lower temperatures and eventually saturates at approximately 52 T at 1.5 K, suggestive of an enhancement of the Pauli limit.

Table 4.1 | Device properties of MoS_2-EDLTs.

	T_c (K)	n_{2D} (cm^{-2})	μ_H (cm^2/Vs)	τ (fs)	τ_{SO} (fs)
Device L1	10.0	1.5×10^{14}	208	59.3	11.1
Device H1	6.5	0.85×10^{14}	86	25.5	17.9
Device H2	7.4	1.8×10^{14}	165	47.1	21.3

transport is larger τ_{SO}, being unphysical (Table 4.1). This is an unphysical situation which contradicts with the initial assumption required for this theory ($\tau << \tau_{SO}$). Thus, the model with the effect of spin orbit scattering does not explain for the enhancement of $B_{c2}^{\parallel}$, consistently.

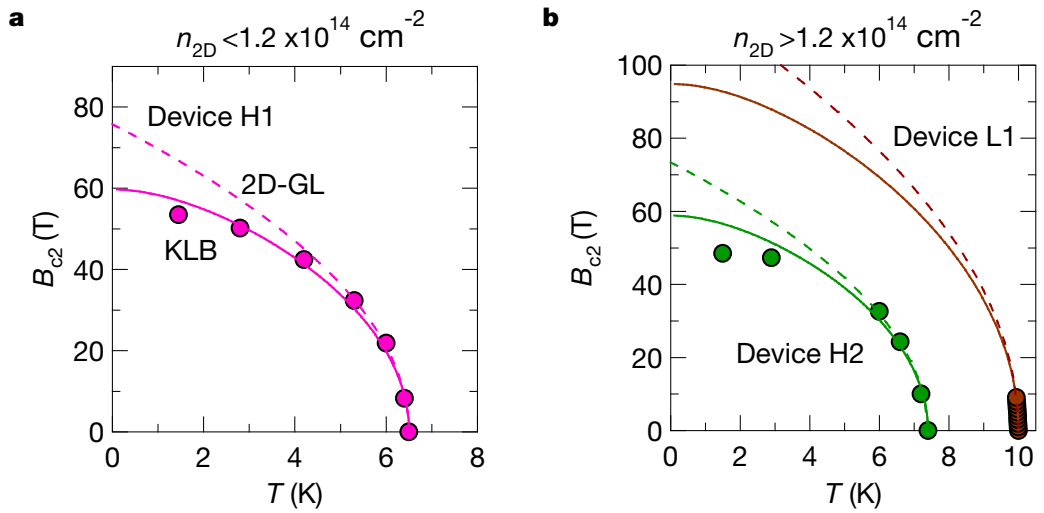

Figure 4.7 | $B_{c2}^{\parallel}$ values at different carrier densities. **a**, **b**, Temperature dependence of $B_{c2}^{\parallel}$ at different carrier densities (**a**: $n_{2D} < 1.2 \times 10^{14}$ cm^{-2}, **b**: $n_{2D} > 1.2 \times 10^{14}$ cm^{-2}). Solid and dashed curves show the 2D-GL and the KLB fittings, respectively.

4.4 Discussion

4.4.1 Band calculation of MoS_2 under an electric field

To find a more plausible origin of the enhancement of the Pauli limit in the present system, Bahramy performed a set of *ab-intio*-based tight-binding supercell calculations on bulk MoS_2, using the full potential augmented plane-wave method and Perdew-Burke-Ernzerhof exchange-correlation functional modified by Becke-Johnson potential, as implemented in WIEN2K program [224]. For each atom, the muffin-tin radius, RMT, was chosen such that its product with the maximum modulus of reciprocal vectors, $K_{\max}$, becomes RMT $K_{\max}$ = 7.0. The relativistic effects, including spin-orbit interaction were fully included and the Brillouin zone was sampled by a $12 \times 12 \times 6$ k-mesh. He then downfolded the bulk Hamiltonian using maximally localized Wannier functions [225−227] and generated a large tight-binding supercell Hamiltonian with an additional potential term to account for the band bending. Finally, he solved this self-consistently using the Poisson equation.

His calculations suggest that under the application of a strong electric field, a high density 2DES is created at the surface of MoS_2. This situation results in formation of an

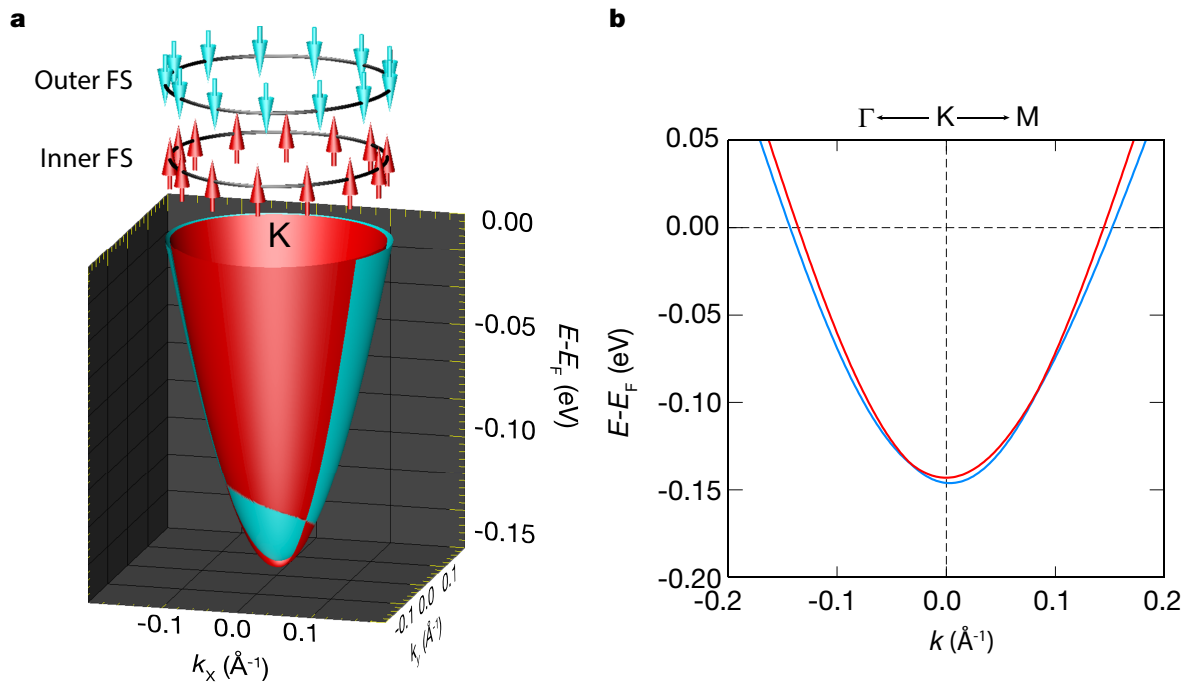

Figure 4.8 | Spin-valley locking in multilayer MoS_2 under an electric field. **a**, Energy band dispersion and spin texture of the conduction band around the K point of bulk MoS_2 under a strong electric field at $n_{2D} = 8.7 \times 10^{13}$ cm^{-2}. Inner Fermi surface (FS) and outer FS at the K points have out-of-plane spin-polarization with opposite directions because each band is almost fully out-of-plane spin polarized by effective Zeeman fields, while the in-plane Rashba-type component is very small with less than 2% of the total spin polarization. **b**, Two-dimensional energy band dispersion near the K point. The spin-split bands cross with each other. The splitting at the Fermi level becomes approximately 13 meV, while that at the K point is approximately 3 meV.

accumulation layer, which is effectively confined within the topmost MoS_2 layer [228]. Such a "quasi-single-layer" 2DES, therefore, ought to have an effective C_{3v} symmetry, leading to many interesting features in the momentum space. For example, once a positive gate voltage is switched on, the conduction band minimum shifts to the ±K points [228]. This situation is in stark contrast to the case of bulk MoS_2, where the conduction band minima are located at six symmetrically equivalent k points along Γ−K directions, also known as the T (or Q) points. Accordingly, the electric-field-induced superconductivity in MoS_2 is expected to be solely mediated by the ± K valleys, and thus the most likely ground state of the Cooper pair should be the inter-valley pairing between the K and -K valleys in order to maintain the zero-momentum for the center-of-mass of the Cooper pairs. Note that the intra-valley spin-singlet

Cooper pairs are not stabilized in the presence of the Zeeman-type SOI, which requires the non-zero momentum.

4.4.2 Possible mechanisms

At a sheet carrier density of $n_{2\mathrm{D}} = 8.7 \times 10^{13}$ cm^{-2}, which is nearly the same as the value in the high magnetic field measurement, the bands are spin-split by $\sim$ 3 meV at the ± K points, at zero magnetic field. Slightly away from the K point, these spin-split bands cross each other such that the splitting becomes $\sim$ 13 meV at the Fermi level. The corresponding band dispersion and spin texture at the Fermi surface are shown in Figs. 4.8a and b, respectively. All these features of the band structure are qualitatively equivalent to those in the monolayer MoS_2 derived from both the tight-binding method [229] and the $\boldsymbol{k} \cdot \boldsymbol{p}$ model [230]. This agreement indicates that bulk or multilayer TMDs under a strong electric field can effectively behave as monolayers.

As shown in Fig. 4.8a, each valley is almost fully out-of-plane spin polarized (spin-valley locking), which is expected to lock the inter-valley Cooper pairs to out-of-plane direction. The in-plane Rashba-type component, which originates from the asymmetric potential along the c-axis produced by the electric field, is calculated to be very small with less than 2% of the total spin polarization. This is indeed expectable by group theory, ruling that no in-plane component is allowed at the K-points owing to their threefold rotational symmetry. In the presence of the finite Rashba-type SOI, a Fulde-Ferrell-Larkin-Ovchinnikov (FFLO) state [90, 91], where Cooper pairs have nonzero momentum, with *s*+*f*-wave symmetry [231], is likely to be realized.

However, we confirmed by a numerical calculation that the enhancement of the upper critical field due to the FFLO state or induced spin-triplet components is negligible. Note that this FFLO state, where Cooper pairs have a finite center of mass momentum which is much smaller than K, should be distinguished from the intra-valley pairing. In addition, (I) the

Rashba SOI, (II) quantum critical point and (III) modified g-factor can be ruled out as origins for the enhancement of upper critical field in the following reasons.

(I) Rashba SOI: Rashba spin-orbit coupling (SOC) will lock the spin to the in-plane direction, which can enhance the out-of-plane B_{c2} beyond the Pauli limit [232]. However, for in-plane magnetic fields, most of the electron spins can contribute to Pauli paramagnetism. Therefore, the enhancement of B_{c2} can be only $\sqrt{2}B_{\mathrm{P}}^{\mathrm{BCS}}$ [233]. In the present case, B_{c2} is enhanced by a factor of 4, which is much larger than the enhancement due to the Rashba SOI. Furthermore, according to his calculations, the Rashba component in the present system is very small, and thus the pure Rashba SOI effect does not contribute to the enhancement of B_{c2}.

(II) Quantum critical point: No ordered state (ex. antiferromagnetic state) has been observed in ion-gated MoS_2 system in the vicinity of the superconducting phase. In that narrow sense, ion-gated MoS_2 system has no QCP, which is known to dramatically enhance the upper critical field. Thus, the enhancement of B_{c2} by the QCP can be ruled out.

(III) Modified electron g-factor: The enhancement of upper critical fields owing to modified electron g-factor may become effective in the case that the LS coupling of multiple d-orbitals competing with crystal field splitting [232] stabilizes the spin-orbital coupled ground state. In the present system, the conduction band at the Fermi level is composed of only single d orbital (d_{z^2})), and therefore, the effect of modified electron g-factor is supposed to be negligible.

Therefore, the spin-valley locking owing to intrinsic Zeeman-type SOI is considered to be the most promising origin for the enhancement of $B_{\mathrm{c2}}^{\parallel}$.

4.4.3 Estimation of the Pauli limit based on the tight-binding model

Nakamura and Yanase numerically estimated the realistic Pauli limit of the present system. The calculation of was carried out based on the tight-binding model which reproduces the conduction band of the effectively single layer MoS_2. The single particle component of the

Hamiltonian is given by $H = H_{\rm kin} + H_{\rm Z} + H_{\rm R}$. Each term is given as following:

$$\hat{H}_{\rm kin} = \sum_{\mathbf{k},s} \epsilon_{\rm Mo}(\boldsymbol{k}) \hat{c}_{\mathbf{k},s} \dagger \hat{c}_{\mathbf{k},s} \tag{4.2}$$

$$\hat{H}_{\rm Z} = \sum_{\mathbf{k},s,s'} \alpha_{\rm Z} \boldsymbol{g}_{\rm Z}(\boldsymbol{k}) \cdot \boldsymbol{\sigma}_{s,s'} \hat{c}_{\mathbf{k},s} \dagger \hat{c}_{\mathbf{k},s'} \tag{4.3}$$

$$\hat{H}_{\rm R} = \sum_{\mathbf{k},s,s'} \alpha_{\rm R} \boldsymbol{g}_{\rm R}(\boldsymbol{k}) \cdot \boldsymbol{\sigma}_{s,s'} \hat{c}_{\mathbf{k},s} \dagger \hat{c}_{\mathbf{k},s'} \tag{4.4}$$

The dispersion relation obtained by the first-principles-based band structure calculation (shown in Fig. 4.8b) is reproduced well by taking into account the nearest-, next-nearest-, and third-nearest-neighbor hopping,

$$\begin{aligned} \epsilon_{\rm Mo}(\boldsymbol{k}) = 2t_1 &\left(\cos k_y a + 2\cos\frac{\sqrt{3}}{2}k_x a \cos\frac{1}{2}k_y a \right) \\ + 2t_2 &\left(\cos\sqrt{3}k_x a + 2\cos\frac{\sqrt{3}}{2}k_x a \cos\frac{3}{2}k_y a \right) \\ + 2t_3 &\left(\cos 2k_y a + 2\cos\sqrt{3}k_x a \cos k_y a \right) - \mu \end{aligned} \tag{4.5}$$

where a is the lattice constant. They determined the hopping parameters t_1, t_2, and t_3, and the chemical potential μ so as to reproduce the band structure calculation. The Zeeman-type SOI arising from the intrinsic mirror symmetry breaking in the crystal structure of MoS_2 is represented by $B_{\rm Z}$, whereas the Rashba-type SOI induced by the extrinsic electric field is represented by $B_{\rm R}$. They are characterized by the g-vector as

$$H_{\rm Z} = \alpha_{\rm Z} \sum_{\mathbf{k}ss'} \mathbf{g}_{\rm Z} \sigma_{ss'} c^{\dagger}_{\mathbf{k}s} c_{\mathbf{k}s'}, H_{\rm R} = \alpha_{\rm R} \sum_{\mathbf{k}ss'} \mathbf{g}_{\rm Z} \sigma_{ss'} c^{\dagger}_{\mathbf{k}s} c_{\mathbf{k}s'} \tag{4.6}$$

and where

$$g_{\rm R}(\boldsymbol{k}) = \left(-\sin k_y - \cos\frac{\sqrt{3}}{2}k_x \sin 12k_y, \sqrt{3}\sin\sqrt{3}2k_x \cos\frac{1}{2}k_y, 0 \right) \tag{4.7}$$

$$g_{\rm Z}(\boldsymbol{k}) = \left(0, 0, \sin k_y - 2\cos\frac{\sqrt{3}}{2}k_x \sin\frac{1}{2}k_y \right) \tag{4.8}$$

and they introduced a trial function $F(\mathbf{k}) = \beta \tanh[\mathbf{f}(\mathbf{K}) - \mathbf{f}(\mathbf{k})] - \mathbf{1}$ in order to reproduce the sign change of the spin-splitting from the K point to the Γ point in the Brillouin

zone. $\mathbf{K} = \left(0, \frac{4\pi}{3a}\right)$ is the wave vector at the K points. They chose the symmetric function $f(\mathbf{k}) = \left|\sin k_{\mathrm{y}}a - 2\cos\frac{\sqrt{3}}{2}k_x a \sin\frac{1}{2}k_y a\right|$ for simplicity. By diagonalizing the single particle Hamiltonian, they obtained the spin-split bands $E_+(\mathbf{k})$ and $E_-(\mathbf{k})$, and fitted parameters α_Z, α_R, and β to the results of band structure calculation, $E_+(\mathbf{k}_{\mathrm{F}}) - E_-(\mathbf{k}_{\mathrm{F}}) = 13$ meV, $E_+(\mathbf{K}) - E_-(\mathbf{K}) = 3$ meV at $n_{2\mathrm{D}} = 8.7 \times 10^{13}$ cm^{-2}, and the ratio of the Rashba- and Zeeman-type SOIs $\langle S_{\mathrm{R}}\rangle/\langle S_{\mathrm{Z}}\rangle = |\alpha_{\mathrm{R}}\mathbf{g}_{\mathrm{R}}(\mathbf{k}_{\mathrm{F}})|/|\alpha_{\mathrm{Z}}\mathbf{g}_{\mathrm{Z}}(\mathbf{k}_{\mathrm{F}})|$. The last equation relies on the results of *ab-intio*-based band calculations that the Rashba-type spin-splitting is at most 2% of the Zeeman-type spin-splitting on the Fermi surface. They defined the Fermi momentum along the K-M line, $\mathbf{k}_{\mathrm{F}}$, where $E_+(\mathbf{k}_{\mathrm{F}}) + E_-(\mathbf{k}_{\mathrm{F}}) = 0$. Adopting these parameters, we obtained the band structure, which matches with Fig. 4.8b obtained by the band structure calculation for the MoS_2-EDLT.

4.4.4 Numerical calculation of the Pauli limit

They calculated the Pauli limit in the present system based on the BCS model $H = H_0 + H_{\mathrm{P}} + H_{\mathrm{I}}$. Taking into account the Zeeman field by an external magnetic field, $H_{\mathrm{P}} = -\sum_{\mathbf{k}ss'} \sigma_{ss'} c^{\dagger}_{\mathbf{k}s} c_{\mathbf{k}s'}$ and the pairing interaction in the s-wave channel $H_{\mathrm{I}} = V\sum_i n_{i\uparrow}n_{i\downarrow}$, they solved the linearized gap equation $1 - V\chi^0_{\mathrm{SC}}(T_{\mathrm{c}}, B_{\mathrm{c2}}) = 0$ where V is the pairing interaction and the irreducible superconducting susceptibility as a function of *T* and *B*, and determined both T_{c} and B_{c2} [234]. They focused on the in-plane magnetic field $\mathbf{H} = H\hat{x}$. The irreducible superconducting susceptibility is obtained as

$$\chi^0_{\mathrm{SC}} = T\sum_{\omega_l}\sum_{\mathbf{k}}\left[G_{\uparrow\uparrow}(\mathbf{k}, i\omega_l)G_{\downarrow\downarrow}(-\mathbf{k}, -i\omega_l) - G_{\downarrow\uparrow}(\mathbf{k}, i\omega_l)G_{\downarrow\uparrow}(-\mathbf{k}, -i\omega_l)\right] \tag{4.9}$$

by using the Matsubara Green function, $\hat{G}(k) = (i\omega_l - \hat{H}_0 - \hat{H}_{\mathrm{P}})^{-1}$. they assumed an attractive interaction $V/t_1 = -2.32$ so that the transition temperature of T_{c} = 6.5 K experimentally observed at zero magnetic field was reproduced.

Figure 4.9a shows the theoretical curves of the Pauli limit in this system. Considering only the Zeeman-type SOI, the Pauli limit is considerably enhanced as it is larger than 70 T

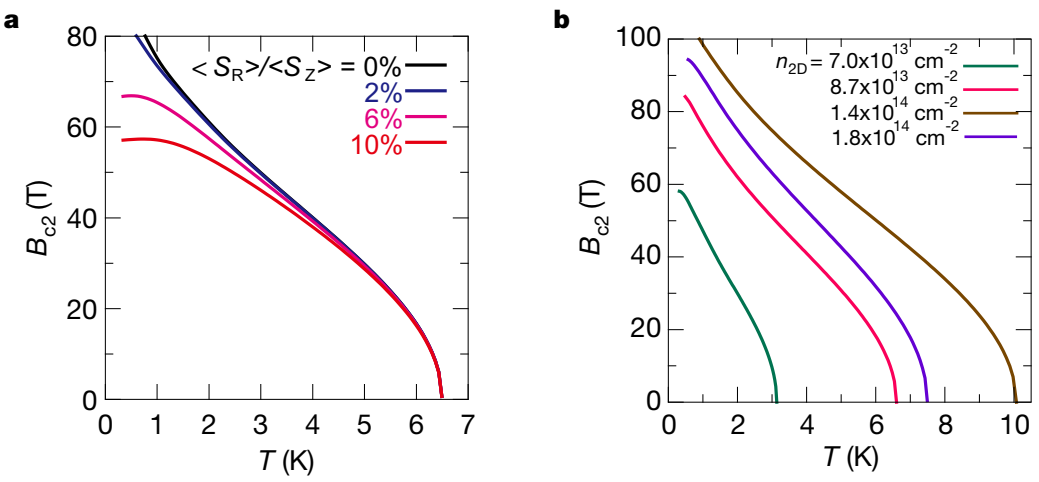

Figure 4.9 | Theoretical calculations of the Pauli limit. **a**, Theoretical curves of the Pauli limit considering both the Zeeman- and small Rashba-type SOI. Black curve is the upper critical field in the tight-binding model reproducing the band structure calculation. The ratio of the Rashba- and Zeeman-type SOI is varied from 0% to 10%. **b**, Theoretical curves of the Pauli limit at different carrier densities and T_c.

at T = 1 K. Also, these strongly enhancement can be observed in different carrier densities (Fig. 4.9b). This result indicates that the large valley-dependent Zeeman-type spin-splitting in the vicinity of the K points ($\sim$ 13 meV) protects singlet Cooper pairing between the K and -K valleys (Fig. 4.10), namely, the Cooper pairing locked by out-of-plane spin polarization to the two opposite directions, termed Ising pairing, enhances $B_{c2}^{\parallel}$ much higher than the $B_{\mathrm{P}}^{\mathrm{BCS}}$.

By contrast, once the small Rashba-type SOI is included, the enhanced Pauli limit is considerably suppressed, indicating that the symmetrical protection by spin-valley locking is weakened (Fig. 4.9a). This is because the in-plane polarized spin components due to the Rashba-type SOI is much more susceptible to an external in-plane magnetic field in comparison to the out-of-plane polarized spins due to intrinsic Zeeman-type SOI. The best agreement with the experimental data is obtained for a moderate Rashba-type SOI of 10% of the Zeeman-type SOI, although such Rashba-type SOI is unlikely in according to the first-principles-based band calculations as mentioned above. We discuss three possible origins for this discrepancy between the theoretical results based on a single-layer tight-binding model and experimental results. We here discuss three possible origins for the discrepancy between the theoretical re-

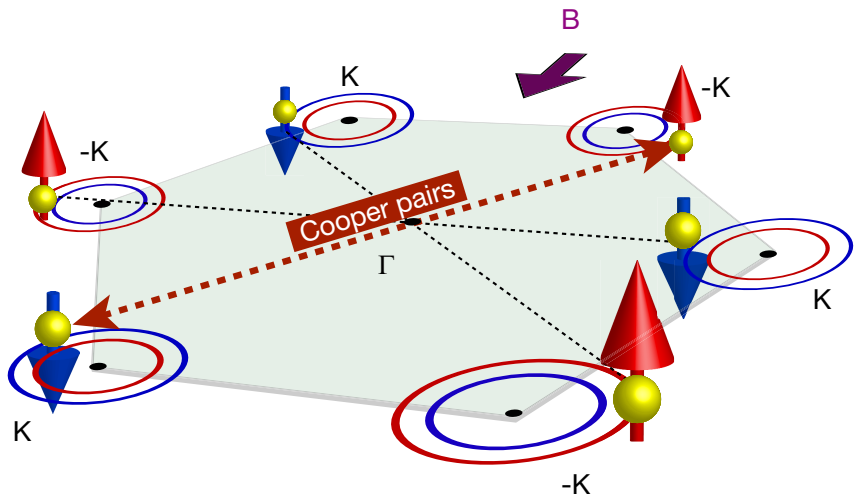

Figure 4.10 | Schematic image of intervalley Cooper pairing protected by spin-valley locking in the in-plane magnetic field geometry. Each spin at K and -K valleys is aligned in the the out-of-plane direction due to internal magnetic field. Inter-valley Cooper pairing formed between the K and -K valleys is robust against an external in-plane magnetic field.

sults based on a single-layer tight-binding model and experimental results. One is the weak proximity of carriers to the second MoS_2 layer, in which small number of carriers are considered to be accumulated. Because the second layer acquires Zeeman-type SOI with an opposite sign to the first layer, the proximity leads to a suppression of SOI and suppresses the enhancement of the Pauli limit. The second possibility is a small misalignment of the pulsed magnetic fields. The pulsed magnetic fields may not be precisely parallel to the surface of the channel, because of an error in the angle or the non-uniformity of pulsed magnetic fields. However, taking the size of device into account, the non-uniformity of pulsed magnetic fields is considered to be less than 0.1 T. The third possibility is impurity scattering effect, which is known to suppress the upper critical field. According to the recent theoretical work [235], the moderate inter-valley scattering can explain the flattening of the in-plane upper critical field at low temperatures. Their assumption of inter-valley scattering time is $\sim 10^{12}$ s, which is one order larger than the scattering time ($10^{13} - 5 \times 10^{14}$) calculated from transport data (Table 4.1) [236].

According to their calculation including the dependence both the carrier density and

T_c, the Pauli limit is predominantly controlled by the Zeeman-type SOI and T_c and the contribution of Rashba-type SOI is negligibly small, in the range of the carrier density where superconductivity realizes in this system (Fig. 4.9b). These results demonstrate that, by the application of a strong electric field, MoS_2, which is believed to be a conventional superconductor in bulk forms, becomes an unconventional 2D Ising superconductor in which Cooper pairs are protected by spin-valley locking and thereby very robust against external magnetic fields, which results in the dramatic enhancement of the Pauli limit. Our findings thus indicate that, combined with highly crystalline materials, unprecedented exotic nature of superconductivity has become accessible by the geometrical confinement owing to a strong electric field, which suggests that electric-field-induced superconductivity offers a new platform to unveil the intrinsic nature of 2D crystalline superconductors.

5
Nonreciprocal transport in a 2D trigonal superconductor

5.1 Introduction

Noncentrosymmetric superconductors have been widely studied since they provide a variety of interesting phenomena as introduced in the previous section. In addition to these exotic phenomena, the noncentrosymmetric nature can be detected directly as a nonlinear electrical resistance under a magnetic field and discussed in terms of superconducting fluctuation [237]. In the system where both spatial inversion and time reversal symmetry are broken, the electrical resistance generally depends on the current direction, which can be probed as the second harmonic magnetoresistance. Such nonreciprocal transport has been originally studied in artificial helical structure or interface [238, 239]. Nowadays, the progress in sample fabrications have made it possible to investigate the nonreciprocal phenomena reflecting the intrinsic crystal structure. In a polar semiconductor [240] and a chiral molecular conductor [241], the nonreciprocal signal coming from their crystal structure has been confirmed. While these nonreciprocal charge transport phenomena have been studied in the normal state [240−242], only two experimental examples were recently found for superconducting systems. One is a

potassium intercalated WS_2 chiral nanotube showing the nonreciprocity overlapped with the Little-Parks oscillation because of its chiral and tubular structure [243]. The other example is the gate-induced 2D superconductivity in 2*H*-MoS_2 [237], where the nonreciprocal resistance in longitudinal direction due to its in-plane broken inversion symmetry is enhanced at the superconducting state.

Recent state-of-the-art techniques enable to fabricate highly crystalline 2D materials, with which we can access to the symmetry-breaking-related physics in 2D superconducting systems [34]. Mechanically-exfoliated atomic layers and field-effect devices based on TMD single crystals such as $NbSe_2$ [26, 27], TaS_2 [244] atomic layers and ion-gated MoS_2 [30] belong to such a new class for investigating exotic phenomena of 2D noncentrosymmetric superconductors because they possess threefold symmetry in the single layer form. 2*H*-MoS_2, which is originally a layered semiconductor, becomes a 2D crystalline superconductor with a maximum transition temperature T_{c} of around 10 K in an EDLT configuration [30, 219]. Although multilayer MoS_2 possesses centrosymmetric structure with D_{6h}^4 symmetry, by the application of a strong electric field, almost all carriers are confined in the topmost layer and thus the neighboring monolayers become inequivalent as is explained in chapter 4. Therefore, ion-gated multilayer MoS_2 can be regarded as a quasi-monolayer-superconductor with C_{3v} symmetry, namely a 2D trigonal superconductor. Since there are few examples for a 2D trigonal superconductor, ion-gated MoS_2 is an ideal platform to investigate the intrinsic properties in such a system [245].

In this chapter, I report a comprehensive study on the superconducting nonreciprocal transport phenomena in ion-gated 2*H*-MoS_2 single crystals. We found that second harmonic resistance in longitudinal and transverse direction appears only in the configuration of excitation current parallel to the zigzag and armchair edge, respectively, while no discernible signal in the other direction has been observed. This experimentally observed results are satisfied selection rules in threefold symmetry. Remarkably, the second harmonic Hall effect, termed

as magnetochiral Hall effect, which has never been reported in nonmagnetic conductors or superconducting state, is found in the present system. Furthermore, the nonreciprocal signals are found to be observed in the lowest temperature under the magnetic field and can be tuned by the excitation bias current. Such behavior unique to the present system could be explained by a picture that vortices are rectified by the microscopically asymmetric potentials originating from the structural threefold symmetry because the region where signals appear is governed by vortices'motion, rather than the paraconductivity contribution around T_{c} [237].

5.2 Selection rules reflecting threefold symmetry

We prepared two EDLT samples with different configurations: the direction of the current is parallel to the zigzag (configuration A; sample 1) or armchair directions (configuration B; sample 2) as shown in Fig. 5.1. The crystal orientations of obtained MoS_2 flakes were determined from the shape of the edge according to the previous study [246], which demonstrated that the straight line in exfoliated MoS_2 flakes corresponds to a zigzag edge with a high statistical rate. We then performed the AC measurement and observed the first (R^{ω}) and second ($R^{2\omega}$) harmonic signals of longitudinal (R_{xx}) and transverse (R_{xy}) resistance. The second harmonic AC measurement is useful for detecting difference of the resistance depending on the current direction [240]. The T_{c} of sample 1 and 2, defined as T where R_{sheet} becomes the midpoint of the resistive transition is 8.8 and 6.8 K, respectively.

To investigate the nonreciprocal component in superconducting MoS_2, we performed the second harmonic measurement. Figures 5.2a and b (c and d) show the R^{ω} and $R^{2\omega}$ harmonic signals as a function of B, respectively, when $T = 2$ K and $I = 13$ μA (15 μA) in the configuration A (B). In configuration A (B), $R^{2\omega}$ component of R_{xx} (R_{xy}) was only observed and no discernible signal was present in the other component. The linear component observed in sample 2 (Fig. 5.2b) is possibly attributed to the second harmonic component of source-drain current, which inevitably appears due to the geometrical difference of source-drain electrodes

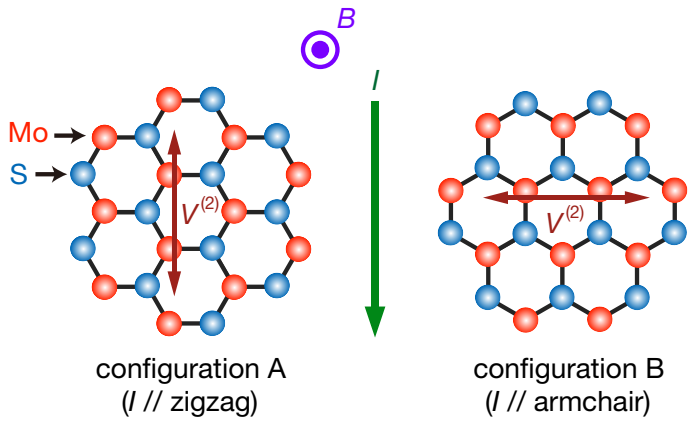

Figure 5.1 | Two kinds of device configurations depending on the MoS_2. In configuration A (B), the applied current is parallel to the zigzag (armchair) direction and the second harmonic signal of longitudinal (transversal) component can be observed.

in the device structure. It is noted that the detected second harmonic signal in the Hall component in the configuration B, which we call magnetochiral Hall effect, has never been observed in nonmagnetic materials or superconducting state. The observed nonreciprocal signals, second order resistance antisymmetric against a magnetic field, completely satisfying the selection rules derived from trigonal structure in ion-gated MoS_2, suggests that the obtained signal originates from the crystal structure of MoS_2 because such behavior in the second harmonic signals are expected from the threefold symmetry. As B increases, the $R^{2\omega}$ signal observed in both configurations first increases, then reaches the peak and finally decreases down to almost zero. The $R^{2\omega}$ signal was negligibly small in the normal state. This peak behavior in $R^{2\omega}$ versus B indicates that the nonreciprocal signals are enhanced in the vortex flow region because they are suppressed in both zero-magnetic field where no vortices exist and high magnetic field where superconductivity is destroyed. It is noted that the zero resistance state under magnetic fields is very fragile and the B-T phase diagram is dominated by the quantum metallic state in the ion-gated 2D superconductors [36]. This is a common characteristic of highly crystalline 2D superconductors owing to the weak pinning and the quantum fluctuations [38], and also the intermediate metallic state between zero resistance state and normal state is governed by vortex flow because the relatively large excitation current is applied in the present system. This

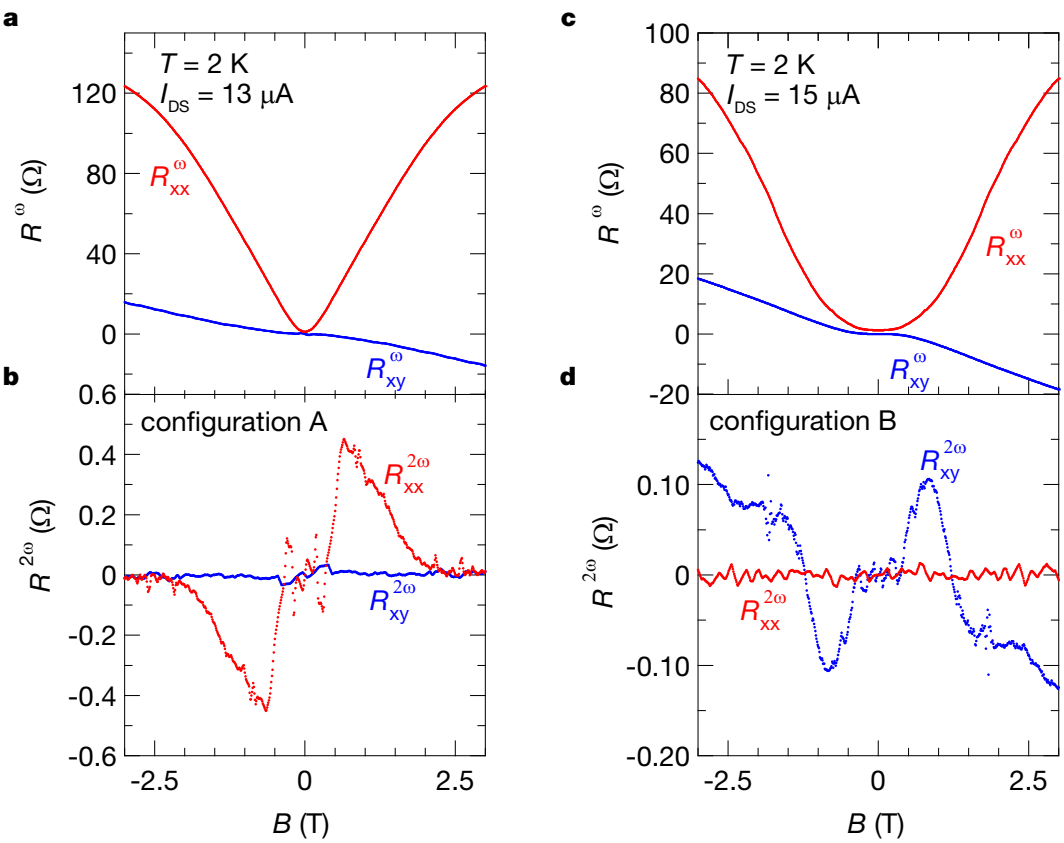

Figure 5.2 | Confirmation of the selection rules reflecting threefold symmetry. **a**, **b**, Longitudinal (R_{xx}: red) and transversal (R_{xy}: blue) (**a**) first (R^{ω}) and (**b**) second ($R^{2\omega}$) harmonic magnetoresistance when T = 2 K, I = 13 μA in configuration A, which is shown in the inset. R^{ω}_{xx} is symmetrized and others are antisymmetrized. **c**, **d**, Longitudinal (R_{xx}: red) and transversal (R_{xy}: blue) (**c**) first (R^{ω}) and (**d**) second ($R^{2\omega}$) harmonic magnetoresistance when T = 2 K, I = 15 μA in configuration B, which is shown in the inset. R^{ω}_{xx} is symmetrized and others are antisymmetrized.

broadening of the resistive transition under magnetic fields is advantageous for detecting the nonreciprocal resistance in the present system.

The possible origin for the linear component observed in Fig. 5.2d and 5.3d can be attributed to Hall effect of the nonlinear component of source-drain current ($I^{2\omega}$), namely a component which is proportional to the square of in-put AC voltage in the current flowing through the sample. This $I^{2\omega}$ possibly comes from geometrical difference of each electrode in the sample. When out-of-plane magnetic field is applied, $I^{2\omega}$ generates the transverse second harmonic resistance in the similar manner as normal Hall effect in the first harmonic component, which cannot be distinguished from intrinsic nonreciprocal resistance in the normal state.

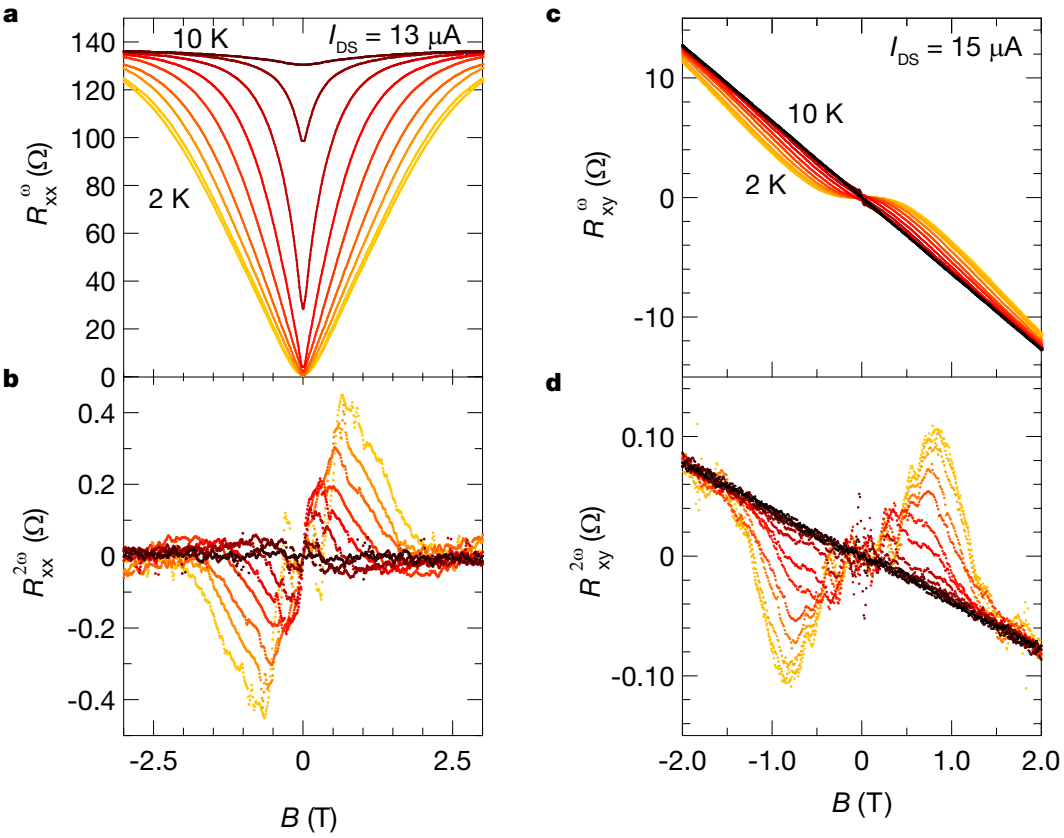

Figure 5.3 | First and second harmonic magnetoresistance at various temperatures for the longitudinal and transverse direction. **a**, **b**, Longitudinal first (R^{ω}_{xx}) (**a**) and second ($R^{2\omega}_{\mathrm{xx}}$) (**b**) harmonic magnetoresistance for temperatures varying in 0.5 K steps from 2 to 7 K, and 8, 9 and 10 K when I = 13 μA in configuration A, which is shown in the inset. R^{ω}_{xx} is symmetrized and $R^{2\omega}_{\mathrm{xx}}$ is antisymmetrized. **c**, **d**, Transverse first (R^{ω}_{xy}) (**c**) and second ($R^{2\omega}_{\mathrm{xx}}$) (**d**) harmonic magnetoresistance for temperatures varying in 0.5 K steps from 2 to 7 K and in 1 K steps from 7 to 10 K when I = 15 μA in configuration B, which is shown in the inset. R^{ω}_{xy} and $R^{2\omega}_{\mathrm{xy}}$ are both antisymmetrized.

However, the anomalous increase of 2ω component in fluctuation or vortex flow regime in the present system cannot be explained by the effect of $I^{2\omega}$, and thus we can conclude that this behavior intrinsically comes from the crystal symmetry of MoS_2. Figures 5.3a and b (c and d) show R^{ω} and $R^{2\omega}$ as a function of B at various temperatures (2−10 K) in sample 1 (sample 2), respectively. The $R^{2\omega}$ signal disappears as temperature increases, and cannot be discernible at the normal state. Figure 5.4a shows the peak values of the second harmonic signal ($R^{2\omega}_{\mathrm{peak}}$) versus T extracted from Figs. 5.3b and d in configuration A (red circle) and B (blue square), respectively. $R^{2\omega}_{\mathrm{peak}}$ increases with decreasing temperature, and concomitantly the corresponding

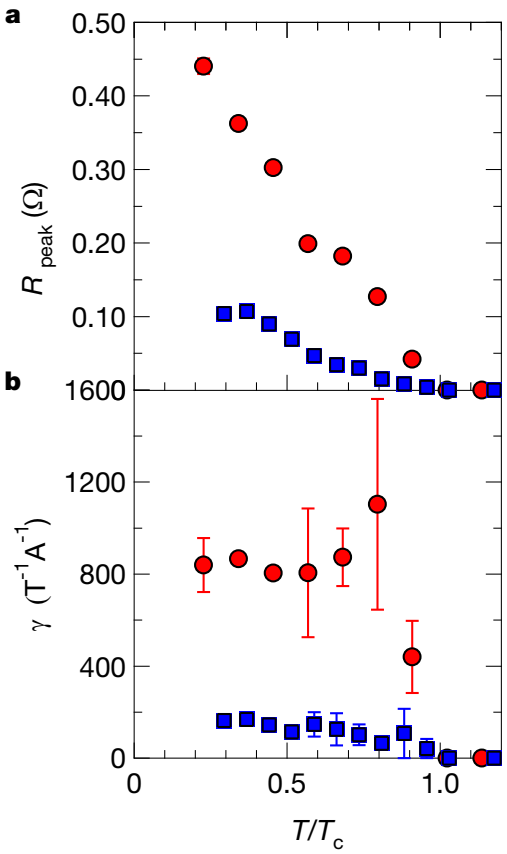

Figure 5.4 | The peak value and the γ value at various temperatures for the longitudinal and transverse direction. a, Peak values of nonreciprocal resistance in configuration A (red) and B (blue). **b**, γ values as a function of normalized temperature calculated from $R^{2\omega}_{peak}$ and B_{peak}, which is the magnetic field at the peak, in configuration A (red) and B (blue). T/T_{c} is the temperature normalized by T_{c}, which are 8.8 K and 6.8 K in sample 1 and 2, respectively. Error bars represent the uncertainties of the γ because of the broad peak of the $R^{2\omega}_{\mathrm{xx}}$ and $R^{2\omega}_{\mathrm{xy}}$.

peak position of B (B_{peak}) (Fig. 5.4a) increases, which may suggest that the increase of upper critical field at lower temperature causes the larger nonreciprocal signals. Figure 5.4b shows the value of γ, which represents the strength of nonreciprocal transport as defined below, in sample 1 (red circle) and 2 (blue square) as a function of T/T_{c}.

When the resistance has a term that is proportional to both *B* and *I*, the output voltage is expressed by

$$V = R^{(1)}I + \Gamma BI^2 \tag{5.1}$$

where $R^{(1)}$ is the resistance of first order and Γ the coefficient of nonreciprocal resistance.

When the AC bias current (source-drain current) with a frequency of ω ($I = I_0 \cos \omega t$) is applied, the output voltage is expressed as follows:

$$V = R^{(1)} I_0 \cos \omega t + \frac{\Gamma B I_0^2}{2}(1 + \cos 2\omega t) \tag{5.2}$$

At that time, by extracting ω component (R^{ω}),

$$R^{\omega} = R^{(1)}, \tag{5.3}$$

is obtained. On the other hand, by extracting 2ω component ($R^{2\omega}$),

$$R^{2\omega} = \frac{1}{2}\Gamma B I_0, \tag{5.4}$$

is obtained. Thus, Γ is defined as

$$\Gamma = \frac{2R^{2\omega}}{BI_0}. \tag{5.5}$$

However, the $R^{2\omega}$ signal in superconducting systems has a peak as a function of *B*, which makes it difficult to simply make a linear fit. Hence, we approximated $R^{2\omega}$ and B by the peak value ($R^{2\omega}_{\mathrm{peak}}$) and the magnetic field at the peak (B_{peak}), respectively. Finally, we normalized the value of γ with the normal state resistance (T = 15 K) in zero magnetic field and defined it as $\gamma = \frac{2R^{2\omega}}{R_{\mathrm{sheet}} B I_0}$. Actually, the gamma can be defined with the expression of $j = \sigma_1 E + \sigma_2 E^2$. If we solve in terms of *E*, then we obtained

$$E = \frac{-\sigma_1 \pm \sqrt{\sigma_1^2 + 4\sigma_2 j}}{2\sigma_2} \approx \frac{1}{\sigma_1} j + \frac{\sigma_2}{\sigma_1^3} j^2 \tag{5.6}$$

Here, we chose the plus sign to satisfy the linear order relation. With the sample width and length L, we had the current $I = Wj$, and we have obtained,

$$V = -\frac{L}{\sigma_1 W} I - \frac{\sigma_2 L}{\sigma_1^3 W^2} I^2 \tag{5.7}$$

Then, assumming $I = I_0 \cos \omega t$, we obtain $\gamma = \frac{2R^{2\omega}}{R_{\mathrm{sheet}} B I_0}$.

The γ value suddenly increases once the temperature goes below the transition temperature, which may be attributed to the paraconductivity effect as discuss below. However, large

nonlinear magnetoresistance survives even at the lowest temperature. The γ values at 2 K are approximately 850 $T^{-1}A^{-1}$ and 200 $T^{-1}A^{-1}$ in longitudinal (configuration A) and transversal direction (configuration B), respectively, which are much higher than those reported for the normal state in a variety of materials [238, 240−242].

5.3 Current dependence of nonreciprocal transport

Next, we investigated the excitation current dependence of the nonreciprocal resistance. Figures 5.5a and b represent R^{ω} and $R^{2\omega}$ in sample 1, respectively, as a function of B at various source-drain currents (5−45 μA) at 2 K. Figure 5.5a indicates a quenching of superconductivity because of an increase of the current. The gradual quenching behavior of the current dependence reflects the 2D nature of the system. From Fig. 5.5b, we plotted $R^{2\omega}_{\mathrm{peak}}$ (left, purple square) and B_{peak} (right, orange triangle) as a function of source-drain current in Fig. 5.5c. According to Fig. 5.5c, $R^{2\omega}_{\mathrm{peak}}$ first increases and then begins to decrease while B_{peak} monotonically decreases, as the current increases. This monotonic decrease in B_{peak} reflects a weakened superconductivity (decrease of upper critical field) by increasing excitation current. Meanwhile, as the current increases, the nonreciprocal signal $R^{2\omega}_{\mathrm{peak}}$ first increases reflecting nonlinear nature of observed signals. Then, with further increase of current, $R^{2\omega}_{\mathrm{peak}}$ begins to decrease because an increase of current weakens and finally destroys the superconductivity. The γ value shows dome-like shape as a function of excitation current (Fig. 5.5d), which is due to the similar behavior in $R^{2\omega}_{\mathrm{peak}}$. This excitation current dependent behavior of nonreciprocal signals is very similar to the ratchet effect in superconducting system [247−249].

5.4 Discussion

To discuss the origins for nonreciprocal transport phenomena observed in the present system, Wakatsuki, Hoshino, Ezawa and Nagaosa describe the theoretical analysis of nonreciprocal transport near and above the mean field superconducting transition temperature T_{c} for MoS_2

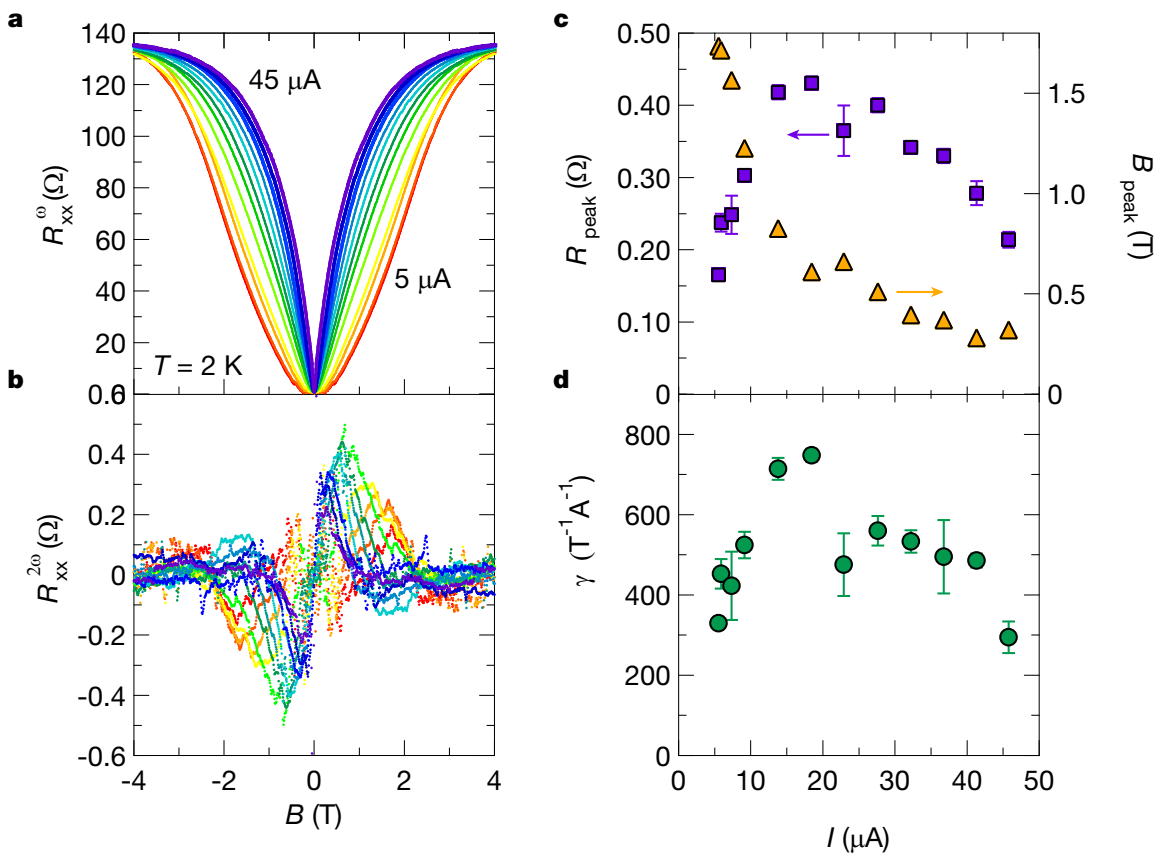

Figure 5.5 | First and second harmonic magnetoresistance, the peak value, the magnetic field at the peak and the γ values at various source-drain currents. **a**, **b**, The longitudinal (R_{xx}) (**a**) first (R^{ω}) and (**b**) second ($R^{2\omega}$) harmonic magnetoresistance for currents at 5, 6, 7, 9, 13, 18, 23, 28, 32, 36, 41 and 45 μA when T = 2 K in configuration A. R^{ω}_{xx} is symmetrized and $R^{2\omega}_{\mathrm{xx}}$ is antisymmetrized. **c**, Peak values of $R^{2\omega}_{\mathrm{xx}}$ ($R^{\omega}_{\mathrm{peak}}$: left, purple square) and the magnetic field at the peak (B_{peak}: right, yellow triangle) as a function of current, The γ value as a function of current calculated from $R^{2\omega}_{\mathrm{peak}}$ and B_{peak} in configuration A. Error bars represent the uncertainties of the R_{peak} and γ because of the broad peak of the $R^{2\omega}_{\mathrm{xx}}$.

under an out-of-plane magnetic field. 2D MoS_2 is well described by the Hamiltonian [229, 250],

$$H_{\mathbf{k}\sigma\tau} = \frac{\hbar^2 \boldsymbol{k}^2}{2m} + \tau_z \lambda k_x (k_x^2 - 3k_y^2) - \Delta_{\mathrm{Z}} \sigma_{\mathrm{z}} - \Delta_{\mathrm{SO}} \sigma_{\mathrm{z}} \tau_{\mathrm{z}} \tag{5.8}$$

around the K and -K points. Here, λ is the parameter of the trigonal warping [251], Δ_{Z} and Δ_{SO} are the spin splittings due do the Zeeman effect and the spin-orbit interaction, respectively, and $\sigma_{\mathrm{z}} = \pm 1$ (or $\uparrow, \downarrow$) and $\tau_z = \pm\ 1$ (or +,−) represent the spin and valley degrees of freedom, respectively. For simplicity, they have omitted the Rashba spin-orbit interaction because of the electric field in the EDLT device because the Rashba term does not contribute

to the nonreciprocal response. They first derive the GL free energy as,

$$F = \int d\boldsymbol{r}\Psi^* \left[a + \frac{p^2}{4m} + \frac{\Lambda B}{\hbar^3}(p_x^3 - 3p_x p_y^2) \right] \Psi + \frac{b}{2}\int d\boldsymbol{r}|\Psi(\boldsymbol{r})|^4, \tag{5.9}$$

with $p = -i\hbar\nabla$, $\Lambda = \frac{93\zeta(5)}{28\zeta(3)}\frac{g\mu_B\Delta_{\mathrm{SO}}\lambda}{(\pi k_{\mathrm{B}}T_{\mathrm{c}})}^2$, the g factor g and the Bohr magneton μ_{B}. a and b are the conventional coefficients in the GL theory. In 2D superconductors in the type-II limit, there are two characteristic temperatures. One is the mean field transition temperature T_{c}, which indicates the crossover temperature around which the amplitude of the order parameter develops, while the phase fluctuation remains due to the unbound vortices and anti-vortices. At the BKT temperature $T_{\mathrm{BKT}} < T_{\mathrm{c}}$, these vortices and anti-vortices form bound pairs and hence the phase rigidity appears. Here they theoretically discuss the Gaussian fluctuation region $T_{\mathrm{c}} \leq T$. Following the analysis of Schmid [252], employing the time-dependent GL equation, they obtain the excess current because of the superconducting fluctuation [237], which is called paraconductivity, as

$$\boldsymbol{j} = \frac{e^2}{16\hbar}\epsilon^{-1}\boldsymbol{E} - \frac{\pi e^3 m\lambda B}{64\hbar^3 k_{\mathrm{B}}T_{\mathrm{c}}}\epsilon^{-2}\boldsymbol{F}(\boldsymbol{E}) \tag{5.10}$$

with $\epsilon = \frac{T-T_{\mathrm{c}}}{T_{\mathrm{c}}}$ and $F(E) = (E_{\mathrm{x}}^2 - E_{\mathrm{y}}^2, -2E_{\mathrm{x}}E_{\mathrm{y}})$, which satisfies the transformation rule of the $C_{3\mathrm{v}}$ point group. There is finite nonreciprocal current, which develops around the critical region.

On the other hand, the normal phase does not carry the nonreciprocal current in this model because the contributions from the two pairs of the bands cancel out in the lowest order. Hence, neglecting the nonreciprocal current in the normal state, one can define the linear and nonlinear transport coefficients as $\boldsymbol{j} = (\sigma_1 + \sigma_{\mathrm{N}})\boldsymbol{E} + \sigma_2\boldsymbol{F}(\boldsymbol{E})$, where σ_1 and σ_2 are the contributions from superconducting fluctuation, and σ_{N} is the normal conductivity. Around the critical region, the fluctuation conductivity gets larger than the normal conductivity, and the γ value is approximately

$$\gamma = \frac{\sigma_2}{\sigma_1^2 WB} = \frac{4\pi m\lambda}{eW\hbar k_{\mathrm{B}}T_{\mathrm{c}}} \tag{5.11}$$

with the channel width *W*. We will estimate the amplitude of the γ value and show below that

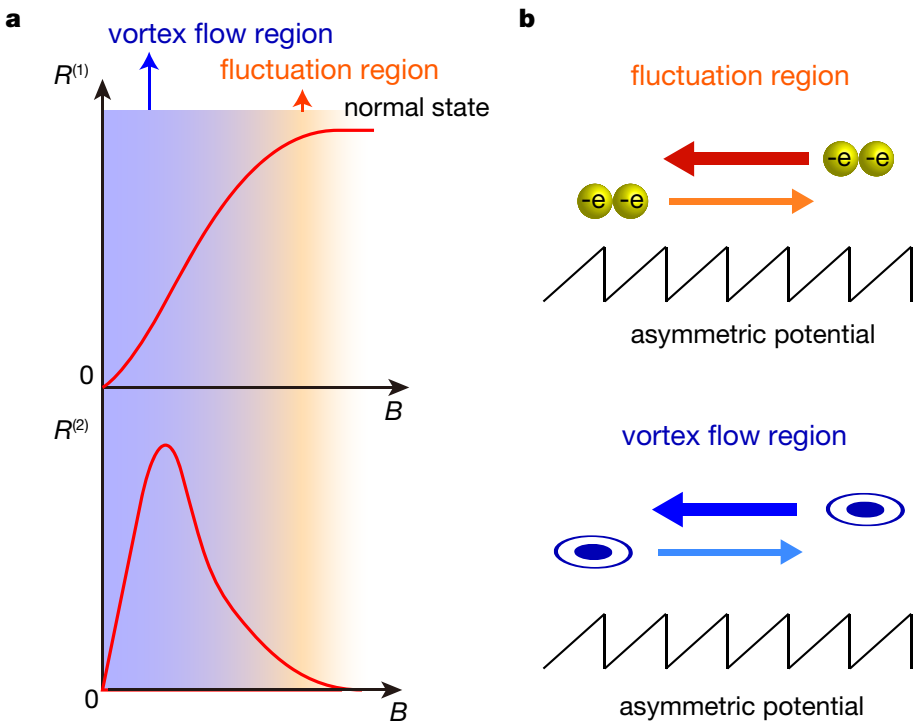

Figure 5.6 | Possible mechanism for nonreciprocal superconducting transport. a, Schematic image of the first and second harmonic resistance as a function of B in 2D noncentrosymmetric superconductors. **b**, Schematic image of recertified paraconductivity and vortex ratchet effect in fluctuation regime and vortex flow regime, respectively.

it is dramatically enhanced in the superconducting state. Although the normal state does not carry nonreciprocal current in this model, one can estimate its typical order of magnitude by using the current from only one of the pairs of the bands. Then, the ratio of the γ values in the normal region (γ_{N}) and the resistive superconducting region (γ_{SC}) is

$$\frac{\gamma_{\mathrm{SC}}}{\gamma_{\mathrm{N}}} \sim \left(\frac{\epsilon_{\mathrm{F}}}{k_{\mathrm{B}}T_{\mathrm{c}}}\right)^3 \tag{5.12}$$

which is quite large. We emphasize that this anomalous enhancement of the γ parameter should be a universal feature in noncentrosymmetric superconductors because it derives from the energy scale difference between the Fermi energy and the superconducting gap.

In addition to the unidirectional paraconductivity, which is theoretically investigated as a possible mechanism as mentioned above [237], another mechanism to be considered for nonreciprocal superconducting transport is the vortex ratchet effect reflecting the asymmetric

crystal structure or asymmetric pinning potentials reflecting trigonal symmetry (Fig. 5.6). The vortex ratchet effect has been originally studied in systems with artificial asymmetric potentials, in which AC driven vortices rectified by artificial asymmetric potential arrays cause a DC electric field. In MoS_2, this ratchet effect may originate from its intrinsic asymmetric potentials arising from the crystal symmetry, which is in marked contrast to the macroscopic artificial structure in conventional systems [245−247] because the nonreciprocal signals observed in the present system are enhanced in the vortex flow regime and strongly dependent on the excitation current. According to the theoretical prediction based on semi-classical model, the shape of vortices is determined by lower symmetry of either the anisotropic Fermi surface or superconducting gap symmetry [253−255]. In the present system, the shape of vortices is affected by the trigonally-warped Fermi surface at the conduction band, and thus vortices should be trigonally-warped. Also, it is noted that the extrinsic effect from surface steps and inhomogeneous carrier accumulation can be negligible in the present system because we chose the step-free region for the channel as confirmed in AFM measurement in chapter 3. Therefore, the trigonally-warped vortices feeling microscopic crystal potential and/or pinning potential reflecting threefold symmetry is possibly the most plausible origin for the observation of nonreciprocal signals in the vortex flow regime. This vortex ratchet effect derived from crystal symmetry should be universal nature for noncentrosymmetric superconductors.

In summary, we found the magnetochiral Hall effect through a comprehensive study of nonreciprocal transport in 2D superconducting MoS_2. The observed nonreciprocal signals, second order resistance antisymmetric against a magnetic field, completely satisfying the selection rules derived from trigonal structure in ion-gated MoS_2, prove that the obtained signal arises from the crystal structure and is enhanced in superconducting state. From the experimental results, we propose that rectification of trigonally-warped vortices by the microscopic crystal potential and/or pinning potential reflecting threefold symmetry is a dominant origin for the nonreciprocal charge transport including magnetochiral Hall effect in the low temperature

region, in addition to the paraconductivity contribution, which might be important around T_{c}. The present results suggest that 2D trigonal superconductors can be not only a potential platform for investigating intrinsic physical properties in 2D noncentrosymmetric superconductors but also a key tool towards future superconducting nanoelectronics.

6 Conclusions and future perspective

6.1 Thesis summary

In the long history of superconductivity since 1938, major playgrounds to study the fundamental physics of superconductors in the 2D limit have been dirty systems such as deposited amorphous or granular thin films and/or the layer materials with large amount of disorder until recently. One of the most important issues in 2D superconductors is QPT at crystalline form, which has been discussed in terms of the vortex dynamics and the quantum critical scaling analysis in highly disordered system. Another issue is the intrinsic properties originating from broken inversion symmetry and/or spin-orbit coupling. Newly-emerged 2D crystalline superconductors enable us to study QPT and intrinsic phenomena due to broken inversion symmetry and/or spin-orbit coupling.

In this thesis, I studied 2D superconducting nature, quantum phase transitions, in-plane upper critical field and nonreciprocal charge transport in electric-field-induced superconductivity realized in mechanically-exfoliated layered crystals. A series of unprecedented phenomena observed in this study has not been expected in conventional highly disordered 2D superconductors.

First, we investigated the quantum states under a magnetic field and found a wide range of quantum metallic state in ZrNCl-EDLT. This quantum metallic state and possible metallic ground state has been regarded as an exception in conventional SITs for a long time. In addition, we discovered the Griffiths singularity between quantum metal and weakly localized metal state, which has been long expected to occur. We argued that these new quantum states can be typical of the crystalline or less-disordered 2D superconductor. The third is the huge upper critical fields far beyond the usual Pauli limit for the in-plane magnetic field geometry, observed in MoS_2-EDLT. It was not the traditional spin-orbit scattering model, but a recently developed band-structure-based model that explained this anomalous enhancement of upper critical fields in a semi-quantitative level. The key concept was the spin-valley locking based on the Zeeman-type SOI with in-plane broken inversion symmetry, which is peculiar to this monolayer material. Finally, we have investigated the nonreciprocal charge transport in 2D superconducting MoS_2, and found not only longitudinal unidirectional magnetoresistance but also magnetochiral Hall effect originating from trigonal structure.

These series of unprecedented phenomena suggest that highly crystalline 2D superconductors, including electric-field-induced superconductivity realized by combination of mechanically exfoliated crystals and ionic-liquid gating, evidently offer tremendous opportunities to unveil the intrinsic quantum phase and exotic nature of superconductors, leading to a new era of superconductivity.

6.2 Future perspective

The observations of these states on 2D crystalline superconductors including those by other groups have all been achieved only through electrical transport measurements, leaving unclear the microscopic origin for energy dissipation. Clarifying the microscopic energy dissipation processes and thermodynamics in superconducting 2D crystals and complex heterostructures is essential for future applications such as the superconducting transistor and integrated quantum

bit. Another important issue to be investigated for realizing superconducting nanoelectronics devices toward future quantum computing is the relationship between dissipationless state and vortex dynamics realized in topological superconductors.

Motivated my PhD study, I would like to propose to directly image quantum states of 2D crystalline superconductors and more complex heterostructures using nanoSQUID-on-tip (nSOT) microscopy [256], under development. nSOTs have been recently demonstrated as exceptionally sensitive nanoscale magnetometers [256, 257] and thermometers [258]. Imaging quantum states in 2D crystalline superconductors will give us clues for understanding microscopic origin for quantum energy dissipation process and thermodynamics, which will become a basis for establishing scientific principle of 2D superconductors and also a key role to design and fabricate 2D superconducting nanoelectronics devices with minimal energy dissipation, for example, to use in superconducting quantum bits.

Bibliography

[1] A. Shal'nikov, Superconducting thin films. *Nature* **142**, 74 (1938).

[2] W. Buckel, R. Hilsch, Einfluss der kondensation bei tiefen temperaturen auf den elektrischen widerstand und die supraleitung fr verschiedene metalle. *Zeitschrift fr Phys.* **138**, 109−120 (1954).

[3] R. Hilsh, Noncrystalline Solids. *John Wiley Sons, Inc., New York* (1958).

[4] D. M. Ginsberg, J. S. Shier, Basic Problems in Thin Films Physics (eds Niedermayer, R. & Mayer, H.) 543 (Vandenhoeck and Ruprecht,1966)

[5] M. Strongin, O. F. Kammerer, Ginsberg, D. M., Shier, J. S. Basic Problems in Thin Films Physics (eds Niedermayer, R. & Mayer, H.) 543 (Vandenhoeck and Ruprecht,1966).

[6] J. M. Graybeal, M. R. Beasley, Localization and interaction effects in ultrathin amorphous superconducting films. *Phys. Rev. B* **29**, 4167−4169 (1984).

[7] B. G. Orr, H. M. Jaeger, A. M. Goldman, Local superconductivity in ultrathin Sn films. *Phys. Rev. B* **32**, 7586−7589 (1985).

[8] H. M. Jaeger, D. B. Haviland, A. M. Goldman, B. G. Orr, Threshold for superconductivity in ultrathin amorphous gallium films. *Phys. Rev. B* **34**, 4920−4923 (1986).

[9] H. M. Jaeger, D. B. Haviland, B. G. Orr, A. M. Goldman, Onset of superconductivity in ultrathin granular metal films. *Phys. Rev. B* **40**, 182−196 (1989).

[10] D. B. Haviland, Y. Liu, A. M. Goldman, Onset of superconductivity in the two-dimensional limit. *Phys. Rev. Lett.* **62**, 2180−2183 (1989).

[11] A. F. Hebard, M. A. Paalanen, Magnetic-field-tuned superconductor-insulator transition in two-dimensional films. *Phys. Rev. Lett.* **65**, 927−930 (1990).

[12] Y. Liu, D. B. Haviland, B. Nease, A. M. Goldman, Insulator-to-superconductor transition in ultrathin films. *Phys. Rev. B* **47**, 5931−5946 (1993).

[13] Y. Qin, C. L. Vicente, J. Yoon, Magnetically induced metallic phase in superconducting tantalum films. *Phys. Rev. B* **73**, 100505 (2006).

[14] T. Terashima, K. Shimura, Y. Bando, Superconductivity of one-unit-cell thick $YBa_2Cu_3O_7$ thin film. *Phys. Rev. Lett.* **67**, 1362−1365 (1991).

[15] C. Dekker, P. J. M. Woltgens, Absence of a finite-temperature vortex-glass phase transition in two-dimensional $YBa_2Cu_3O_{7-\delta}$ films. *Phys. Rev. Lett.* **69**, 2717−2720 (1992).

[16] Y. Guo *et al.*, Superconductivity modulated by quantum size effects. *Science*. **306**, 1915−1918 (2004).

[17] T. Nishio, M. Ono, T. Eguchi, H. Sakata, Y. Hasegawa, Superconductivity of nanometer-size Pb islands studied by low-temperature scanning tunneling microscopy. *Appl. Phys. Lett.* **88**, 113115 (2006).

[18] D. Eom, S. Qin, M. Y. Chou, C. K. Shih, Persistent superconductivity in ultrathin Pb films: A scanning tunneling spectroscopy study. *Phys. Rev. Lett.* **96**, 027005 (2006).

[19] S. Qin, J. Kim, Q. Niu, C.-K. Shih, Superconductivity at the two-dimensional limit. *Science*. **324**, 1314−1317 (2009).

[20] T. Zhang *et al.*, Superconductivity in one-atomic-layer metal films grown on Si(111). *Nat. Phys.* **6**, 104−108 (2010).

[21] N. Reyren *et al.*, Superconducting interfaces between insulating oxides. *Science*. **317**, 1196−1199 (2007).

[22] A. Gozar *et al.*, High-temperature interface superconductivity between metallic and insulating copper oxides. *Nature* **455**, 782−785 (2008).

[23] Q.-Y. Wang *et al.*, Interface-induced high-temperature superconductivity in single unit-cell FeSe films on $SrTiO_3$. *Chin. Phys. Lett.* **29**, 037402 (2012).

[24] N. E. Staley *et al.*, Electric field effect on superconductivity in atomically thin flakes of $NbSe_2$. *Phys. Rev. B* **80**, 184505 (2009).

[25] D. Jiang *et al.*, High-T_c superconductivity in ultrathin $Bi_2Sr_2CaCu_2O_{8+x}$ down to half-unit-cell thickness by protection with graphene. *Nat. Commun.* **5**, 5708 (2014).

[26] Y. Cao *et al.*, Quality heterostructures from two-dimensional crystals unstable in air by their assembly in inert atmosphere. *Nano Lett.* **15**, 4914−4921 (2015).

[27] X. Xi *et al.*, Strongly enhanced charge-density-wave order in monolayer $NbSe_2$. *Nat. Nanotechnol.* **10**, 765−769 (2015).

[28] K. Ueno *et al.*, Electric-field-induced superconductivity in an insulator. *Nat. Mater.* **7**, 855−858 (2008).

[29] J. T. Ye *et al.*, Liquid-gated interface superconductivity on an atomically flat film. *Nat. Mater.* **9**, 125−128 (2010).

[30] J. T. Ye *et al.*, Superconducting dome in a gate-tuned band insulator. *Science* **338**, 1193−1196 (2012).

[31] D. Costanzo, S. Jo, H. Berger, A. F. Morpurgo, Gate-induced superconductivity in atomically thin MoS_2 crystals. *Nat. Nanotechnol.* **11**, 339−344 (2016).

[32] M. P. A. Fisher, Quantum phase transitions in disordered two-dimensional superconductors. *Phys. Rev. Lett.* **65**, 923−927 (1990).

[33] A. M. Goldman, Superconductor-insulator transitions. *Int. J. Mod. Phys. B.* **24**, 4081−4101 (2010).

[34] Y. Saito, T. Nojima, Y. Iwasa, Highly crystalline 2D superconductors. *Nat. Rev. Mater.* **2**, 16094 (2016).

[35] J. Biscaras *et al.*, Multiple quantum criticality in a two-dimensional superconductor. *Nat. Mater.* **12**, 542−548 (2013).

[36] Y. Saito, Y. Kasahara, J. Ye, Y. Iwasa, T. Nojima, Metallic ground state in an ion-gated two-dimensional superconductor. *Science* **350**, 409−413 (2015).

[37] Y. Xing *et al.*, Quantum Griffiths singularity of superconductor-metal transition in Ga thin films. *Science* **350**, 542−545 (2015).

[38] A. W. Tsen *et al.*, Nature of the quantum metal in a two-dimensional crystalline superconductor. *Nat. Phys.* **12**, 208−212 (2016).

[39] C. K. Schiller, Angular dependence of the critical field of quenched thin Pb and Sn films. *J. Appl. Phys.* **40**, 4179−4183 (1969).

[40] M. Tinkham, Effect of fluxoid quantization on transitions of superconducting films. *Phys. Rev.* **129**, 2413−2422 (1963).

[41] J. E. Mooij, Percolation, localization and superconductivity. Plenum, New York, 433 (1984).

[42] J. M. Blatt, C. J. Thompson, Shape resonances in superconducting thin films. *Phys. Rev. Lett.* **10**, 332−334 (1963).

[43] B. G. Orr, H. M. Jaeger, A. M. Goldman, Transition-temperature oscillations in thin superconducting films. *Phys. Rev. Lett.* **53**, 2046−2049 (1984).

[44] L. G. Aslamasov, A. I. Larkin, The influence of fluctuation pairing of electrons on the conductivity of normal metal. *Phys. Lett. A.* **26**, 238−239 (1968).

[45] K. Maki, The critical fluctuation of the order parameter in type-II Superconductors. *Prog. Theor. Phys.* **39**, 897−906 (1968).

[46] R. Thompson, Microwave, flux flow, and fluctuation resistance of dirty type-II superconductors. *Phys. Rev. B* **1**, 327−333 (1970).

[47] V. L. Berezinskii, Destruction of long-range order in one-dimensional and two-dimensional systems having a continuous symmetry group I. classical systems. *Sov. Phys. JETP.* **32**, 493−500 (1971).

[48] V. L. Berezinskii, Destruction of long-range order in one-dimensional and two-dimensional systems possessing a continuous symmetry group. II. quantum systems. *Sov. Phys. JETP.* **34**, 610−616 (1972).

[49] J. M. Kosterlitz, D. J. Thouless, Long range order and metastability in two dimensional solids and superfluids. (Application of dislocation theory). *J. Phys. C Solid State Phys.* **5**, 124−126 (1972).

[50] A. F. Hebard, A. T. Fiory, Critical-exponent measurements of a two-dimensional superconductor. *Phys. Rev. Lett.* **50**, 1603−1606 (1983).

[51] M. P. A. Fisher, G. Grinstein, S. M. Girvin, Presence of quantum diffusion in two dimensions: Universal resistance at the superconductor-insulator transition. *Phys. Rev. Lett.* **64**, 587−590 (1990).

[52] W. Krauth, N. Trivedi, S. Ullah, Superfluid-insulator transition in disordered boson systems. *Phys. Rev. Lett.* **67**, 2307−2310 (1991).

[53] R. T. Scalettar, G. G. Batrouni, G. T. Zimanyi, Localization in interacting, disordered, Bose systems. *Phys. Rev. Lett.* **66**, 3144−3147 (1991).

[54] A. Yazdani, A. Kapitulnik, Superconducting-insulating transition in two-dimensional α-MoGe thin films. *Phys. Rev. Lett.* **74**, 3037−3040 (1995).

[55] D. Ephron, A. Yazdani, A. Kapitulnik, M. R. Beasley, Observation of quantum dissipation in the vortex state of a highly disordered superconducting thin film. *Phys. Rev. Lett.* **76**, 1529−1532 (1996).

[56] J. Chervenak, J. Valles, Absence of a zero-temperature vortex solid phase in strongly disordered superconducting Bi films. *Phys. Rev. B* **61**, 9245−9248(R) (2000).

[57] A. M. Goldman, N. Markovic, Superconductor-insulator transitions in the two-dimensional limit. *Phys. Today* **51**, 39−44 (1998).

[58] Y. H. Lin, J. Nelson, A. M. Goldman, Superconductivity of very thin films: The superconductor-insulator transition. *Physica C* **514**, 130−141 (2015).

[59] R. Meservey, P. M. Tedrow, Spin-orbit scattering in superconducting thin films. *Phys. Lett. A.* **58**, 131−132 (1976).

[60] P. M. Tedrow, R. Meservey, Critical magnetic field of very thin superconducting aluminum films. *Phys. Rev. B* **25**, 171−178 (1982).

[61] S. Gariglio, J. M. Triscone, Oxide interface superconductivity. *Comptes Rendus Phys.* **12**, 591−599 (2011).

[62] S. Gariglio, M. Gabay, J. Mannhart, J.-M. Triscone, Interface superconductivity. *Physica C* **514**, 189−198 (2015).

[63] K. Ueno *et al.*, Field-induced superconductivity in electric double layer transistors. *J. Phys. Soc. Jpn.* **83**, 32001 (2014).

[64] C. Xu *et al.*, Large-area high-quality 2D ultrathin Mo_2C superconducting crystals. *Nat. Mater.* **14**, 1135−1141 (2015).

[65] L. Wang *et al.*, Magnetotransport properties in high-quality ultrathin two-dimensional superconducting Mo_2C crystals. *ACS Nano* **10**, 4504−4510 (2016).

[66] Y. Mizukami *et al.*, Extremely strong-coupling superconductivity in artificial two-dimensional Kondo lattices. *Nat. Phys.* **7**, 849−853 (2011).

[67] M. Xue, G. Chen, H. Yang, Y. Zhu, Superconductivity in potassium-doped few-layer graphene. *J. Am. Chem. Soc.* **134**, 6536−6539 (2012).

[68] B. M. Ludbrook *et al.*, Evidence for superconductivity in Li-decorated monolayer graphene. *Proc. Natl. Acad. Sci. U.S.A.* **112**, 11795−11799 (2015).

[69] S. Ichinokura, K. Sugawara, A. Takayama, T. Takahashi, S. Hasegawa, *ACS Nano* **10**, 2761 (2016).

[70] X.-L. Qi, S.-C. Zhang, Topological insulators and superconductors. *Rev. Mod. Phys.* **83**, 1057−1110 (2011).

[71] A. Ohtomo, H. Y. Hwang, A high-mobility electron gas at the $LaAlO_3/SrTiO_3$. *Nature* **427**, 423−426 (2004).

[72] A. D. Caviglia *et al.*, Electric field control of the $LaAlO_3/SrTiO_3$ interface ground state. *Nature* **456**, 624−627 (2008).

[73] C. Richter *et al.*, Interface superconductor with gap behavior like a high-temperature superconductor. *Nature* **502**, 528−531 (2013).

[74] G. Cheng *et al.*, Electron pairing without superconductivity. *Nature* **521**, 196−199 (2015).

[75] J. Biscaras *et al.*, Two-dimensional superconductivity at a Mott insulator/band insulator interface $LaTiO_3/SrTiO_3$. *Nat. Commun.* **1**, 89 (2010).

[76] J. Biscaras *et al.*, Two-dimensional superconducting phase in $LaTiO_3/SrTiO_3$ heterostructures induced by high-mobility carrier doping. *Phys. Rev. Lett.* **108**, 247004 (2012).

[77] A. Gozar, I. Bozovic, High temperature interface superconductivity. *Physica C* **521**, 38−49 (2016).

[78] Q. L. He *et al.*, Two-dimensional superconductivity at the interface of a Bi_2Te_3/FeTe heterostructure. *Nat. Commun.* **5**, 4247 (2014).

[79] M. M. Ozer, J. R. Thompson, H. H. Weitering, Hard superconductivity of a soft metal in the quantum regime. *Nat. Phys.* **2**, 173−176 (2006).

[80] T. Nishio *et al.*, Superconducting Pb island nanostructures studied by scanning tunneling microscopy and spectroscopy. *Phys. Rev. Lett.* **101**, 167001 (2008).

[81] M. M. zer, Y. Jia, Z. Zhang, J. R. Thompson, H. H. Weitering, Tuning the quantum stability and superconductivity of ultrathin metal alloys. *Science* **316**, 1594−1597 (2007).

[82] J. J. Paggel, Quantum-well states as Fabry-Pe'rot modes in a thin-film electron interferometer. *Science* **283**, 1709−1711 (1999).

[83] T. C. Chiang, Photoemission studies of quantum well states in thin films. *Surf. Sci. Rep.* **39**, 181−235 (2000).

[84] T. Uchihashi, P. Mishra, M. Aono, T. Nakayama, Macroscopic superconducting current through a silicon surface reconstruction with indium atoms: Si(111)-($\sqrt{7} \times \sqrt{3}$)-In. *Phys. Rev. Lett.* **107**, 207001 (2011).

[85] M. Yamada, T. Hirahara, S. Hasegawa, Magnetoresistance measurements of a superconducting surface state of In-induced and Pb-induced structures on Si(111). *Phys. Rev. Lett.* **110**, 237001 (2013).

[86] S. Yoshizawa *et al.*, Imaging josephson vortices on the surface superconductor SI (111)-($\sqrt{7} \times \sqrt{3}$)-In using a scanning tunneling microscope. *Phys. Rev. Lett.* **113**, 247004 (2014).

[87] A. V Matetskiy *et al.*, Two-dimensional superconductor with a giant Rashba effect: one-atom-layer Tl-Pb compound on Si(111). *Phys. Rev. Lett.* **115**, 147003 (2015).

[88] D. V. Gruznev *et al.*, A strategy to create spin-split metallic bands on silicon using a dense alloy layer. *Sci. Rep.* **4**, 4742 (2014).

[89] T. Sekihara, R. Masutomi, T. Okamoto, Two-dimensional superconducting state of monolayer Pb films grown on GaAs(110) in a strong parallel magnetic field. *Phys. Rev. Lett.* **111**, 057005 (2013).

[90] P. Fulde, A. R. Ferrell, Superconductivity in a strong spin-exchange field. *Phys. Rev. A* **135**, 550−563 (1964).

[91] A. I. Larkin, Y. N. Ovchinnikov, Nonuniformstate of superconductors. *Sov. Phys. JETP.* **20**, 762−769 (1965).

[92] R. P. Kaur, D. F. Agterberg, M. Sigrist, Helical vortex phase in the noncentrosymmetric $CePt_3Si$. *Phys. Rev. Lett.* **94**, 137002 (2005).

[93] H.-M. Zhang *et al.*, Detection of a superconducting shase in a two-atom layer of hexagonal Ga film grown on semiconducting GaN(0001). *Phys. Rev. Lett.* **114**, 107003 (2015).

[94] M. M. Ugeda *et al.*, Characterization of collective ground states in single-layer $NbSe_2$. *Nat. Phys.* **12**, 92−97 (2016).

[95] F.-C. Hsu *et al.*, Superconductivity in the PbO-type structure alpha-FeSe. *Proc. Natl. Acad. Sci. U.S.A.* **105**, 14262−14264 (2008).

[96] J.-F. Ge *et al.*, Superconductivity above 100 K in single-layer FeSe films on doped $SrTiO_3$. *Nat. Mater.* **14**, 285−289 (2015).

[97] J. J. Lee *et al.*, Interfacial mode coupling as the origin of the enhancement of T_c in FeSe films on $SrTiO_3$. *Nature* **515**, 245−248 (2014).

[98] S. He *et al.*, Phase diagram and electronic indication of high-temperature superconductivity at 65 K in single-layer FeSe films. *Nat. Mater.* **12**, 605−610 (2013).

[99] S. Tan *et al.*, Interface-induced superconductivity and strain-dependent spin density waves in FeSe/$SrTiO_3$ thin films. *Nat. Mater.* **12**, 634−640 (2013).

[100] R. Peng *et al.*, Tuning the band structure and superconductivity in single-layer FeSe by interface engineering. *Nat. Commun.* **5**, 5044 (2014).

[101] J. Shiogai, Y. Ito, T. Mitsuhashi, T. Nojima, A. Tsukazaki, Electric-field-induced superconductivity in electrochemically etched ultrathin FeSe films on $SrTiO_3$ and MgO. *Nat. Phys.* **12**, 42−46 (2015).

[102] Y. Miyata, K. Nakayama, K. Sugawara, T. Sato, T. Takahashi, High-temperature superconductivity in potassium-coated multilayer FeSe thin films. *Nat. Mater.* **14**, 775−779 (2015).

[103] K. S. Novoselov *et al.*, Electric field effect in atomically thin carbon films. *Science* **306**, 666−669 (2004).

[104] A. Geim, K. Novoselov, The rise of graphene. *Nat. Mater.* **6**, 183−191 (2007).

[105] K. S. Novoselov *et al.*, Two-dimensional atomic crystals. *Proc. Natl. Acad. Sci. U.S.A.* **102**, 10451−10453 (2005).

[106] K. F. Mak, C. Lee, J. Hone, J. Shan, T. F. Heinz, Atomically thin MoS_2: A new direct-gap semiconductor. *Phys. Rev. Lett.* **105**, 136805 (2010).

[107] B. Radisavljevic, A. Radenovic, J. Brivio, V. Giacometti, A. Kis, Single-layer MoS_2 transistors. *Nat. Nanotechnol.* **6**, 147−150 (2011).

[108] Q. H. Wang, K. Kalantar-Zadeh, A. Kis, J. N. Coleman, M. S. Strano, Electronics and optoelectronics of two-dimensional transition metal dichalcogenides. *Nat. Nanotechnol.* **7**, 699−712 (2012).

[109] M. Chhowalla *et al.*, The chemistry of two-dimensional layered transition metal dichalcogenide nanosheets. *Nat. Chem.* **5**, 263−275 (2013).

[110] M. Xu, T. Liang, M. Shi, H. Chen, Graphene-like two-dimensional materials. *Chem. Rev.* **113**, 3766−3798 (2013).

[111] X. Xu, W. Yao, D. Xiao, T. F. Heinz, Spin and pseudospins in layered transition metal dichalcogenides. *Nat. Phys.* **10**, 343−350 (2014).

[112] G. Fiori *et al.*, Electronics based on two-dimensional materials. *Nat. Nanotechnol.* **9**, 768−779 (2014).

[113] F. Xia, H. Wang, D. Xiao, M. Dubey, A. Ramasubramaniam, Two-dimensional material nanophotonics. *Nat. Photonics.* **8**, 899−907 (2014).

[114] Y. J. Zhang, M. Yoshida, R. Suzuki, Y. Iwasa, 2D crystals of transition metal dichalcogenide and their iontronic functionalities. *2D Mater.* **2**, 44004 (2015).

[115] Z. Sun, A. Martinez, F. Wang, Optical modulators with two-dimensional layered materials. *Nat. Photonics.* **10**, 227−238 (2016).

[116] K. F. Mak, J. Shan, Photonics and optoelectronics of 2D semiconductor transition metal dichalcogenides. *Nat. Photonics.* **10**, 216−226 (2016).

[117] C. R. Dean *et al.*, Boron nitride substrates for high-quality graphene electronics. *Nat. Nanotechnol.* **5**, 722−726 (2010).

[118] C. R. Dean *et al.*, Hofstadter's butterfly and the fractal quantum Hall effect in moir superlattices. *Nature* **497**, 598−602 (2013).

[119] L. A. Ponomarenko *et al.*, Cloning of Dirac fermions in graphene superlattices. *Nature* **497**, 594−597 (2013).

[120] B. Hunt *et al.* Massive Dirac fermions and Hofstadter butterfly in a van der Waals heterostructure. *Science* **340**, 1427−1430 (2013).

[121] L. Wang *et al.*, Fractional fractal quantum Hall effect in graphene superlattices. *Science* **350**, 1231−1234 (2015).

[122] L. Li *et al.* Quantum Hall effect in black phosphorus two-dimensional electron system. *Nat. Nanotechnol.* **11**, 593−597 (2016).

[123] B. Fallahazad *et al.*, Shubnikov-de Haas oscillations of high-mobility holes in monolayer and bilayer WSe_2: Landau level degeneracy, effective mass, and negative compressibility. *Phys. Rev. Lett.* **116**, 086601 (2016).

[124] R. Frindt, Superconductivity in ultrathin $NbSe_2$ layers. *Phys. Rev. Lett.* **28**, 299−301 (1972).

[125] R. E. Glover, M. D. Sherrill, Changes in superconducting critical temperature produced by electrostatic charging. *Phys. Rev. Lett.* **5**, 248−250 (1960).

[126] H. L. Stadler, Changing Properties of Metals by Ferroelectric Polarization Charging. *Phys. Rev. Lett.* **14**, 979−981 (1965).

[127] A. F. Hebard, A. T. Fiory, R. H. Eick, Experimental Considerations in the quest for a thin-film Superconducting field-effect transistor. *IEEE Trans. Magn.* **23**, 1279−1282 (1987).

[128] A. T. Fiory *et al.*, Metallic and superconducting surfaces of $YBa_2Cu_30_7$ probed by electrostatic charge modulation of epitaxial films. *Phys. Rev. Lett.* **65**, 3441−3444 (1990).

[129] J. Mannhart, D. Schlom, J. Bednorz, K. Mller, Influence of electric fields on pinning in $YBa_2Cu_3O_{7-\delta}$ films. *Phys. Rev. Lett.* **67**, 2099−2101 (1991).

[130] A. Walkenhorst *et al.*, Electric field effects on vortex dynamics in ultrathin $YBa_2Cu_3O_{7-\delta}$ films. *Phys. Rev. Lett.* **69**, 2709−2712 (1992).

[131] X. X. Xi *et al.*, Effects of field-induced hole-density modulation on normal-state and superconducting transport in $YBa_2Cu_3O_{7-x}$. *Phys. Rev. Lett.* **68**, 1240−1243 (1992).

[132] J. Mannhart, High-T_c transistors. *Supercond. Sci. Technol.* **9**, 49−67 (1996).

[133] C. H. Ahn *et al.*, Electrostatic modulation of superconductivity in ultrathin $GdBa_2Cu_3O_{7-x}$ films. *Science* **284**, 1152−1155 (1999).

[134] D. Matthey, S. Gariglio, J. M. Triscone, Field-effect experiments in $NdBa_2Cu_3O_{7-\delta}$ ultrathin films using a $SrTiO_3$ single-crystal gate insulator. *Appl. Phys. Lett.* **83**, 3758−3760 (2003).

[135] K. A. Parendo, K. H. S. B. Tan, A. M. Goldman, Electrostatic and parallel-magnetic-field tuned two-dimensional superconductor-insulator transitions. *Phys. Rev. B* **73**, 174527 (2006).

[136] K. A. Parendo *et al.*, Electrostatic tuning of the superconductor-insulator transition in two dimensions. *Phys. Rev. Lett.* **94**, 197004 (2005).

[137] R. Misra, M. McCarthy, A. F. Hebard, Electric field gating with ionic liquids. *Appl. Phys. Lett.* **90**, 2006−2008 (2007).

[138] H. Shimotani, G. Diguet, Y. Iwasa, Direct comparison of field-effect and electrochemical doping in regioregular poly(3-hexylthiophene). *Appl. Phys. Lett.* **86**, 2003−2006 (2005).

[139] M. J. Panzer, C. R. Newman, C. D. Frisbie, Low-voltage operation of a pentacene field-effect transistor with a polymer electrolyte gate dielectric. *Appl. Phys. Lett.* **86**, 103503 (2005).

[140] H. T. Yuan *et al.*, High-density carrier accumulation in ZnO field-effect transistors gated by electric double layers of ionic liquids. *Adv. Funct. Mater.* **19**, 1046−1053 (2009).

[141] H. Shimotani, H. Asanuma, J. Takeya, Y. Iwasa, Electrolyte-gated charge accumulation in organic single crystals. *Appl. Phys. Lett.* **89**, 203501 (2006).

[142] W. H. Brattain, C.G.B. Garrett, Experiments on the interface between germanium and an electrolyte. *Bell Syst. Tech. J.* **34**, 129−176 (1955).

[143] S. G. Haupt, D. R. Riley, C. T. Jones, J. Zhao, J. T. McDevitt, Reversible modulation of T_c in conductive polymer/high temperature superconductor assemblies. *J. Am. Chem. Soc.* **115**, 1196−1198 (1993).

[144] K. Ueno *et al.*, Discovery of superconductivity in $KTaO_3$ by electrostatic carrier doping. *Nat. Nanotechnol.* **6**, 408−412 (2011).

[145] W. Shi *et al.*, Superconductivity series in transition metal dichalcogenides by ionic gating. *Sci. Rep.* **5**, 12534 (2015).

[146] S. Jo, D. Costanzo, H. Berger, A. F. Morpurgo, Electrostatically induced superconductivity at the surface of WS_2. *Nano Lett.* **15**, 1197−1202 (2015).

[147] Y. Saito, T. Nojima, Y. Iwasa, Gate-induced superconductivity in two-dimensional atomic crystals. *Superconductor Science and Technology* **29**, 093001 (2016).

[148] A. T. Bollinger *et al.*, Superconductor-insulator transition in $La_{2-x}Sr_xCuO_4$ at the pair quantum resistance. *Nature* **472**, 458−460 (2011).

[149] X. Leng, J. Garcia-Barriocanal, S. Bose, Y. Lee, A. M. Goldman, Electrostatic control of the evolution from a superconducting phase to an insulating phase in ultrathin $YBa_2Cu_3O_{7-x}$ films. *Phys. Rev. Lett.* **107**, 027001 (2011).

[150] J. Garcia-Barriocanal *et al.*, Electronically driven superconductor-insulator transition in electrostatically doped $La_2CuO_{4+\delta}$ thin films. *Phys. Rev. B* **87**, 024509 (2013).

[151] S. W. Zeng *et al.*, Two-dimensional superconductor-insulator quantum phase transitions in an electron-doped cuprate. *Phys. Rev. B* **92**, 020503 (2015).

[152] Y. Lee *et al.*, Phase diagram of electrostatically doped $SrTiO_3$. *Phys. Rev. Lett.* **106**, 136809 (2011).

[153] P. Gallagher, M. Lee, J. R. Williams, D. Goldhaber-Gordon, Gate-tunable superconducting weak link and quantum point contact spectroscopy on a strontium titanate surface. *Nat. Phys.* **10**, 748−752 (2014).

[154] Y. Yamada, K. Ueno, T. Fukumura, Electrically induced ferromagnetism at room temperature in cobalt-doped titanium dioxide. *Science* **332**, 1065−1067 (2011).

[155] M. Nakano *et al.*, Collective bulk carrier delocalization driven by electrostatic surface charge accumulation. *Nature* **487**, 459−462 (2012).

[156] H. T. Yuan *et al.*, Zeeman-type spin splitting controlled by an electric field. *Nat. Phys.* **9,** 563−569 (2013).

[157] Y. Saito, Y. Iwasa, Ambipolar insulator-to-metal transition in black phosphorus by ionic-liquid gating. *ACS Nano* **9**, 3192−3198 (2015).

[158] M. Yoshida *et al.*, Gate-optimized thermoelectric power factor in ultrathin WSe_2 single crystals. *Nano Lett.* **16**, 2061−2065 (2016).

[159] S. Shamoto *et al.*, Structures of β-ZrNCl and superconducting $Li_{0.16}$ZrNCl: double honeycomb lattice superconductor. *Physica C* **306**, 7−14 (1998).

[160] S. Yamanaka, K. Hotehama, H. Kawaji, Superconductivity at 25.5 K in electron-doped layered hafnium nitride. *Nature* **392**, 580−582 (1998).

[161] T. Ito *et al.*, Two-dimensional nature of superconductivity in the intercalated layered systems Li_xHfNCl and Li_xZrNCl: Muon spin relaxation and magnetization measurements. *Phys. Rev. B* **69**, 134522 (2004).

[162] M. Steiner, N. Breznay, A. Kapitulnik, Approach to a superconductor-to-Bose-insulator transition in disordered films. *Phys. Rev. B.* **77**, 212501 (2008).

[163] A. Glatz, A. A. Varlamov, V. M. Vinokur, Fluctuation spectroscopy of disordered two-dimensional superconductors. *Phys. Rev. B* **84**, 104510 (2011).

[164] Baturina T. I. Baturina *et al.*, Superconducting phase transitions in ultrathin TiN films. *Europhys. Lett.* **97**, 17012 (2012).

[165] L. B. Ioffe, A. I. Larkin, A. A. Varlamov, L. Yu, Effect of superconducting fluctuations on the transverse resistance of high-T_c superconductors. *Phys. Rev. B* **47**, 8936−8941 (1993).

[166] V. V. Dorin, R. A. Klemm, A. A. Varlamov, A. I. Buzdin, D. V. Livanov, Fluctuation conductivity of layered superconductors in a perpendicular magnetic field. *Phys. Rev. B* **48**, 12951−12965 (1993).

[167] T. Schneider, S. Weyeneth, Suppression of the Berezinskii-Kosterlitz-Thouless and quantum phase transitions in two-dimensional superconductors by finite-size effects. *Phys. Rev. B.* **90**, 064501 (2014).

[168] B. I. Halperin, D. R. Nelson, Resistive transition in superconducting films. *J. Low Temp. Phys.* **36**, 599−616 (1979).

[169] K. Ueno, T. Nojima, S. Yonezawa, M. Kawasaki, Effective thickness of two-dimensional superconductivity in a tunable triangular quantum well of $SrTiO_3$. *Phys. Rev. B* **89**, 020508 (2014).

[170] T. Brumme, M. Calandra, F. Mauri, Electrochemical doping of few-layer ZrNCl from first principles: Electronic and structural properties in field-effect configuration. *Phys. Rev. B* **89**, 245406 (2014).

[171] T. Takano, Y. Kasahara, T. Oguchi, Doping variation of optical properties in ZrNCl superconductors. *J. Phys. Soc. Jpn.* **80**, 023702 (2011).

[172] Y. Taguchi, A. Kitora, Y. Iwasa, Increase in T_c upon reduction of doping in LixZrNCl superconductors. *Phys. Rev. Lett.* **97**, 107001 (2006).

[173] M. V. Feigel'man, V. B. Geshkenbein, A. I. Larkin, Pinning and creep in layered superconductors. *Physica C* **167**, 177−187 (1990).

[174] D. Das, S. Doniach, Existence of a Bose Metal at $T = 0$. *Phys. Rev. B* **60**, 1261−1275 (1999).

[175] D. Das, S. Doniach, Bose metal: Gauge-field fluctuations and scaling for field-tuned quantum phase transitions. *Phys. Rev. B* **64**, 134511 (2001)

[176] D. Dalidovich, P. Phillips, Phase glass is a Bose metal: A new conducting state in two dimensions. *Phys. Rev. Lett.* **89**, 027001 (2002).

[177] P. Phillips, D. Dalidovich, The elusive Bose metal. *Science* **302**, 243−247 (2003).

[178] E. Shimshoni, A. Auerbach, A. Kapitulnik, Transport through quantum melts. Phys. Rev. Lett. **80**, 3352−3355 (1998).

[179] Y. H. Lin, J. Nelson, A. M. Goldman, Suppression of the Berezinskii-Kosterlitz-Thouless transition in 2D superconductors by macroscopic quantum tunneling. *Phys. Rev. Lett.* **109**, 017002 (2012).

[180] N. Mason, A. Kapitulnik, Dissipation effects on the superconductor-insulator transition in 2D superconductors. *Phys. Rev. Lett.* **82**, 5341−5344 (1999).

[181] S. Ullah, A. T. Dorsey, Critical fluctuations in high-temperature superconductors and the Ettingshausen effect. *Phys. Rev. Lett.* **65**, 2066−2069 (1990).

[182] S. Ullah, A. T. Dorsey, Effect of Fluctuations on the transport properties of type-II superconductors in a magnetic field Salman. *Phys. Rev. B* **44**, 262−273 (1991).

[183] M. H. Theunissen, P. H. Kes, Resistive transitions of thin film superconductors in a magnetic field. *Phys. Rev. B* **55**, 15183−15190 (1997).

[184] T. Palstra, B. Batlogg, L. Schneemeyer, J. Waszczak, Transport entropy of vortex motion in $YBa_2Cu_3O_7$. *Phys. Rev. Lett.* **64**, 3090−3093 (1990).

[185] N. R. Werthamer, E. Helfand, P. C. Hohenberg, Temperature and purity dependence of the superconducting critical field, H_{c2}. III. Electron spin and spin-orbit effects. *Phys. Rev.* **147**, 295−302 (1966).

[186] T. Vojta, J. Schmalian, Quantum Griffiths effects in itinerant Heisenberg magnets. *Phys. Rev. B* **72**, 045438 (2005).

[187] T. Vojta, R. Sknepnek, Critical points and quenched disorder: From Harris criterion to rare regions and smearing. *Phys. Status Solidi Basic Res.* **241**, 2118−2127 (2004).

[188] T. Vojta, J. A. Hoyos, Criticality and quenched disorder: Harris criterion versus rare regions. *Phys. Rev. Lett.* **112**, 075702 (2014).

[189] A. B. Harris, Effect of random defects on the critical behavior of Ising models. *J. Physica C Solid State Phys.* **7**, 1671−1692 (1974).

[190] D. S. Fisher, Random transverse field Ising spin chains. *Phys. Rev. Lett.* **69**, 534−537 (1992).

[191] D. S. Fisher, Critical behavior of random transverse-field Ising spin chains. *Phys. Rev. B* **53**, 1689−1699 (1995).

[192] O. Motrunich, S.-C. Mau, D. Huse, D. Fisher, Infinite-randomness quantum Ising critical fixed points. *Phys. Rev. B* **61**, 1160−1172 (2000).

[193] L. Demk *et al.*, Disorder promotes ferromagnetism: rounding of the quantum phase transition in $Sr_{1-x}Ca_xRuO_3$. *Phys. Rev. Lett.* **108**, 185701 (2012).

[194] S. Ubaid-Kassis, T. Vojta, A. Schroeder, Quantum Griffiths phase in the weak itinerant ferromagnetic alloy $N_{1-x}V_x$. *Phys. Rev. Lett.* **104**, 066402 (2010).

[195] A. H. C. Neto, G. Castilla, B. A. Jones, Non-Fermi liquid behavior and Griffiths phase in *f*-electron compounds. *Phys. Rev. Lett.* **81**, 3531−3534 (1998).

[196] M. C. de Andrade *et al.*, Evidence for a common physical description of non-Fermi-liquid behavior in *f*-electron systems. *Phys. Rev. Lett.* **81**, 5620−5623 (1998).

[197] A. Del Maestro, B. Rosenow, J. A. Hoyos, T. Vojta, Dynamical conductivity at the dirty superconductor-metal quantum phase transition. *Phys. Rev. Lett.* **105**, 145702 (2010).

[198] Y. Xing *et al.*, Ising superconductivity and quantum phase transition in macro-size monolayer $NbSe_2$. *Nano Lett.* **17**, 6802−6807 (2017).

[199] S. Shen *et al.*, Observation of quantum Griffiths singularity and ferromagnetism at the superconducting $LaAlO_3/SrTiO_3$ interface. *Phys. Rev. B.* **94**, 144517 (2016).

[200] S. Sachdev, P. Werner, M. Troyer, Universal conductance of nanowires near the superconductor-metal quantum transition. *Phys. Rev. Lett.* **92**, 237003 (2004).

[201] J. Hoyos, C. Kotabage, T. Vojta, Effects of dissipation on a quantum critical point with disorder. *Phys. Rev. Lett.* **99**, 230601 (2007).

[202] T. Vojta, C. Kotabage, J. Hoyos, Infinite-randomness quantum critical points induced by dissipation. *Phys. Rev. B* **79**, 024401 (2009).

[203] A. Del Maestro, B. Rosenow, M. Mller, S. Sachdev, Infinite randomness fixed point of the superconductor-metal quantum phase transition. *Phys. Rev. Lett.* **101**, 035701 (2008).

[204] I. Kovcs, F. Igli, Renormalization group study of the two-dimensional random transverse-field Ising model. *Phys. Rev. B* **82**, 054437 (2010).

[205] T. Vojta, A. Farquhar, J. Mast, Infinite-randomness critical point in the two-dimensional disordered contact process. *Phys. Rev. E.* **79**, 011111 (2009).

[206] D. S. Fisher, Flux-lattice melting in thin-film superconductors. *Phys. Rev. B* **22**, 1190−1199 (1980).

[207] D. S. Fisher, M. P. A. Fisher, D. A. Huse, Thermal fluctuations, quenched disorder, phase transitions, and transport in type-II superconductors. *Phys. Rev. B* **43**, 130−159 (1991).

[208] G. Blatter, M. V. Feigel'man, V. B. Geshkenbein, A. I. Larkin, V. M. Vinokur, Vortices in high-temperature superconductors. *Rev. Mod. Phys.* **66**, 1125−1388 (1994).

[209] N. Scopigno *et al.*, Phase separation from electron confinement at oxide interfaces. *Phys. Rev. Lett.* **116**, 026804 (2016).

[210] V. F. Gantmakher, M. V Golubkov, V. T. Dolgopolov, G. E. Tsydynzhapov, A. A. Shashkin, Superconductor-insulator transition in amorphous In-O films. *Physica B* **284**, 649−650 (2000).

[211] P. Spathis, H. Aubin, A. Pourret, K. Behnia, Nernst effect in the phase-fluctuating superconductor InO_x. *Eur. Phys. Lett.* **83**, 57005 (2008).

[212] V. F. Gantmakher, M. V Golubkov, Width of the zero-field superconducting resistive transition in the vicinity of the localization threshold. *JETP Lett.* **73**, 131−134 (2001).

[213] P. A. Frigeri, D. F. Agterberg, M. Sigrist, Spin susceptibility in superconductors without inversion symmetry. *New J. Phys.* **6**, 115 (2004).

[214] P. A. Frigeri, D. F. Agterberg, A. Koga, M. Sigrist, Superconductivity without inversion symmetry: MnSi versus $CePt_3Si$. *Phys. Rev. Lett.* **92**, 097001 (2004).

[215] Y. Matsuda, H. Shimahara, Fulde−Ferrell−Larkin−Ovchinnikov state in heavy fermion superconductors. *J. Phys. Soc. Jpn.* **76**, 051005 (2007).

[216] Z. Y. Zhu, Y. C. Cheng, U. Schwingenschlgl, Giant spin-orbit-induced spin splitting in two-dimensional transition-metal dichalcogenide semiconductors. *Phys. Rev. B* **84**, 153402 (2011).

[217] D. Xiao, G.-B. Liu, W. Feng, X. Xu, W. Yao, Coupled spin and valley physics in monolayers of MoS_2 and other group-VI dichalcogenides. *Phys. Rev. Lett.* **108**, 196802 (2012).

[218] R. Coehoorn, C. Haas, J. Dijkstra, Electronic structure of $MoSe_2$, MoS_2, and WSe_2. I. Band-structure calculations and photoelectron spectroscopy. *Phys. Rev. B* **35**, 6195−6202 (1987).

[219] Y. Saito *et al.*, Superconductivity protected by spin-valley locking in ion-gated MoS_2 *Nat. Phys.* **12**, 144−149 (2016).

[220] J. M. Lu *et al.*, Evidence for two-dimensional Ising superconductivity in gated MoS_2. *Science* **350**, 1353−1357 (2015).

[221] X. Xi *et al.*, Ising pairing in superconducting $NbSe_2$ atomic layers. *Nat. Phys.* **12**, 139−143 (2016).

[222] K. Maki, Effect of Pauli paramagnetism on magnetic properties of high-field superconductors. *Phys. Rev.* **148**, 362−369 (1966).

[223] R. Klemm, A. Luther, M. Beasley, Theory of the upper critical field in layered superconductors. *Phys. Rev. B* **12**, 877−891 (1975).

[224] P. Blaha, G. Madsen, WIEN2K program package. Available at http://www.wien2k.at.

[225] I. Souza, N. Marzari, D. Vanderbilt, Maximally-localized Wannier functions for entangled energy bands. *Phys. Rev. B* **65**, 035109 (2001).

[226] J. Kune *et al.*, Wien2wannier: From linearized augmented plane waves to maximally localized Wannier functions. *Comput. Phys. Commun.* **181**, 1888−1895 (2010).

[227] A. A. Mostofi *et al.*, An updated version of wannier90: A tool for obtaining maximally-localised Wannier functions. *Comput. Phys. Commun.* **185**, 2309−2310 (2014).

[228] T. Brumme, M. Calandra, F. Mauri, First-principles theory of field-effect doping in transition-metal dichalcogenides: Structural properties, electronic structure, Hall coefficient, and electrical conductivity. *Phys. Rev. B* **91**, 155436 (2015)

[229] G. B. Liu, W. Y. Shan, Y. Yao, W. Yao, D. Xiao, Three-band tight-binding model for monolayers of group-VIB transition metal dichalcogenides. *Phys. Rev. B* **88**, 085433 (2013).

[230] A. Kormnyos *et al.*, $\boldsymbol{k} \cdot \boldsymbol{p}$ theory for two-dimensional transition metal dichalcogenide semiconductors. *2D Mater.* **2**, 22001 (2015).

[231] P. A. Frigeri, Superconductivity in crystals without an inversion center. PhD Thesis (2005).

[232] E. Bauer, M. Sigrist, Non-centrosymmetric superconductors: Introduction and overview. (Springer, Berlin/Heidelberg, 2012).

[233] L. P. Gor'kov, E. I. Rashba, Superconducting 2D system with lifted spin degeneracy: mixed singlet-triplet state. *Phys. Rev. Lett.* **87**, 037004 (2001).

[234] Y. Nakamura, Y. Yanase, Multi-orbital superconductivity in $SrTiO_3/LaAlO_3$ interface and $SrTiO_3$ surface. *J. Phys. Soc. Jpn* **82**, 083705 (2013).

[235] S. Ilic, J. S. Meyer, M. Houzet, Enhancement of the upper critical field in disordered transition metal dichalcogenide monolayers. *Phys. Rev. Lett.* **119**, 117001 (2017).

[236] Y. J. Zhang, W. Shi, J. T. Ye, R. Suzuki, Y. Iwasa, Robustly protected carrier spin relaxation in electrostatically doped transition-metal dichalcogenides. *Phys. Rev. B* **95**, 205302 (2017).

[237] R. Wakatsuki, Y. Saito *et al.*, Nonreciprocal charge transport in noncentrosymmetric superconductors. *Sci. Adv.* **3**, e1602390 (2017).

[238] G. L. J. A. Rikken, E. Raupach, Observation of magneto-chiral dichroism. *Nature* **390**, 493−494 (1997).

[239] G. L. J. A. Rikken, P. Wyder, Magnetoelectric anisotropy in diffusive transport. *Phys. Rev. Lett.* **94**, 016601 (2005).

[240] T. Ideue *et al.*, Bulk rectification effect in a polar semiconductor. *Nat. Phys.* **13**, 578−583 (2017).

[241] F. Pop, P. Auban-Senzier, E. Canadell, G. L. J. A. Rikken, N. Avarvari, Electrical magnetochiral anisotropy in a bulk chiral molecular conductor. *Nat. Commun.* **5**, 3757 (2014).

[242] G. L. J. A. Rikken, J. Flling, P. Wyder, Electrical magnetochiral anisotropy. *Phys. Rev. Lett.* **87**, 236602 (2001).

[243] F. Qin *et al.*, Superconductivity in a chiral nanotube. *Nat. Commun.* **8**, 14465 (2017).

[244] E. Navarro-Moratalla *et al.*, Enhanced superconductivity in atomically thin TaS_2. *Nat. Commun.* **7**, 11043 (2016).

[245] N. F. Q. Yuan, K. F. Mak, K. T. Law, Possible topological superconducting phases of MoS_2. *Phys. Rev. Lett.* **113**, 097001 (2014).

[246] Y. Guo *et al.*, Distinctive in-plane cleavage behaviors of two-dimensional layered materials. *ACS Nano* **10**, 8980−8988 (2016).

[247] J. E. Villegas, S. Savel, F. Nori, E. M. Gonzalez, A superconducting reversible rectifier that controls the motion of magnetic flux quanta. *Science* **302**, 1188−1191 (2003).

[248] J. E. Villegas, E. M. Gonzalez, M. P. Gonzalez, J. V. Anguita, J. L. Vicent, Experimental ratchet effect in superconducting films with periodic arrays of asymmetric potentials. *Phys. Rev. B* **71**, 024519 (2005).

[249] C. C. de Souza Silva, J. Van de Vondel, M. Morelle, V. V. Moshchalkov, Controlled multiple reversals of a ratchet effect. *Nature* **440**, 651−654 (2006).

[250] H. Yu, Y. Wu, G.-B. Liu, X. Xu, W. Yao, Nonlinear valley and spin currents from Fermi pocket anisotropy in 2D crystals. *Phys. Rev. Lett.* **113**, 156603 (2014).

[251] A. Kormnyos *et al.*, Monolayer MoS_2: Trigonal warping, the Γ valley, and spin-orbit coupling effects. *Phys. Rev. B* **88**, 045416 (2013).

[252] A. Schmid, Diamagnetic susceptibility at the transition to the superconducting state. *Phys. Rev.* **180**, 527−529 (1969).

[253] N. Schopohl, K. Maki, Quasiparticle spectrum around a vortex line in a *d*-wave superconductor. *Phys. Rev. B* **52**, 490−493 (1995).

[254] M. Ichioka, N. Hayashi, N. Enomoto, K. Machida, Vortex structure in *d*-wave superconductors. *Phys. Rev. B* **53**, 15316−15326 (1996).

[255] H. Ueki, W. Kohno, T. Kita, Vortex-core charging due to the Lorentz force in a *d*-wave superconductor. *J. Phys. Soc. Jpn.* **85**, 064702 (2016).

[256] D. Vasyukov *et al.*, A scanning superconducting quantum interference device with single electron spin sensitivity. *Nat. Nanotechnol.* **8**, 639−644 (2013).

[257] L. Embon *et al.*, Vortex-core charging due to the Lorentz force in a *d*-wave superconductor. *Nat. Commun.* **8**, 85 (2017).

[258] D. Halbertal *et al.*, Nanoscale thermal imaging of dissipation in quantum systems. *Nature* **539**, 407−410 (2016).

List of Publications

1. **Enhanced coupling and reduced dimensions in lightly intercalated superconductors**
   Y. Nakagawa, **Y. Saito**, T. Nojima, K. Inumaru, S. Yamanaka, Y. Kasahara and Y. Iwasa
   submitted.

2. **Magnetochiral Hall effect in a 2D trigonal superconductor**
   Y. M. Itahashi*, **Y. Saito***(co-first), T. Ideue and Y. Iwasa
   (*equal contribution)
   submitted.

3. **Quantum phase transitions in highly crystalline two-dimensional superconductors**
   Y. Saito, T. Nojima and Y. Iwasa
   Nature Communications, in press.

4. **Electric-field-control of electronic states in WS_2 nanodevices by electrolyte gating**
   F. Qin, T. Ideue, W. Shi, Y. Zhang, R. Suzuki, M. Yoshida, **Y. Saito** and Y. Iwasa
   Journal of Visualized Experiments, in press.

5. **Nonreciprocal charge transport in noncentrosymmetric superconductors**
   R. Wakatsuki*, **Y. Saito***(co-first), S. Hoshino, Y. M. Itahashi, T. Ideue, M. Ezawa, Y. Iwasa and N. Nagaosa
   (*equal contribution)
   Science Advances **3**, e1602390 (2017).

6. **Highly crystalline 2D superconductors**
   Y. Saito, T. Nojima and Y. Iwasa
   Nature Reviews Materials **2**, 16094 (2016).

7. **電気二重層トランジスタと2次元超伝導**
   斎藤 優、野島 勉、岩佐 義宏
   固体物理 **51**, 775−778 (2016).

8. **Gate-tuned thermoelectric power in black phosphorus**
   Y. Saito*, T. Iizuka*, T. Koretsune, R. Arita, S. Shimizu and Y. Iwasa
   (*equal contribution)
   Nano Letters **16**, 4819−4824 (2016).

9. **Gate-induced superconductivity in two-dimensional atomic crystals**
   Y. Saito, T. Nojima and Y. Iwasa
   Superconductor Science and Technology **29**, 093001 (2016).

10. **Gate-optimized thermoelectric power factor in ultrathin WSe_2 single crystals**
    M. Yoshida, T. Iizuka, **Y. Saito**, M. Onga, R. Suzuki, Y. J. Zhang, Y. Iwasa and S. Shimizu
    Nano Letters **16**, 2061−2065 (2016).

11. **Superconductivity protected by spin-valley locking in ion-gated MoS_2**
    Y. Saito, Y. Nakamura, M. S. Bahramy, Y. Kohama, J. T. Ye, Y. Kasahara, Y. Nakagawa, M. Onga, M. Tokunaga, T. Nojima, Y. Yanase and Y. Iwasa
    Nature Physics **12**, 144−149 (2016).

12. **Metallic ground state in an ion-gated two-dimensional superconductor**
    Y. Saito, Y. Kasahara, J. T. Ye, Y. Iwasa and T. Nojima
    Science **350**, 409−413 (2015).

13. **Superconductivity series in transition metal dichalcogenides by ionic gating**
    W. Shi, J. T. Ye, Y. J. Zhang, R. Suzuki, M. Yoshida, J. Miyazaki, N. Inoue, **Y. Saito** and Y. Iwasa
    Scientific Reports **5**, 12534 (2015).

14. **Ambipolar insulator-to-metal transition in black phosphorus by ionic-liquid gating**
    Y. Saito and Y. Iwasa
    ACS Nano **9**, 3192−3198 (2015).